

TUNABLE PHOTONIC CRYSTAL BIOSENSORS FOR PORTABLE LABEL-FREE DIAGNOSTICS

A DISSERTATION
SUBMITTED TO THE DEPARTMENT OF ELECTRICAL ENGINEERING
AND THE COMMITTEE ON GRADUATE STUDIES
OF STANFORD UNIVERSITY
IN PARTIAL FULFILLMENT OF THE REQUIREMENTS
FOR THE DEGREE OF
DOCTOR OF PHILOSOPHY

Meredith Marie Lee

June 2012

Abstract

Although there is a pressing global need for widely-deployable disease detection and monitoring systems, today's options for biochemical analysis are often bulky, slow, expensive, and reliant on trained medical personnel. In contrast, the miniaturization and integration of devices based on arrays of sources, detectors, and active or passive biosensing surfaces provides a means to achieve handheld diagnostic capabilities with a "lab-on-a-chip" that would be vastly less expensive and fully automated.

Reducing the size of each piece of conventional analysis systems in hopes of yielding a portable, point-of-care biosensor is problematic because of challenges that arise in maintaining detection capabilities, as well as difficulties in assembling miniature components. Consequently, there is great interest in designing biochemical analysis systems that can not only capitalize on established manufacturing technology, but also leverage novel nanoscale phenomena to maximize detection performance. Employing cost-effective integrated semiconductor microfabrication techniques and concepts from the growing field of nanophotonics, we aim to design devices that reduce overall sensor sizes and costs substantially, while maintaining adequate sensitivity and specificity compared with existing systems.

In particular, the development of label-free affinity-based optical sensors offers an opportunity for multi-modality measurements, where different sensing mechanisms can be integrated on one platform to provide correlated results for increased diagnostic accuracy. In addition to being sensitive, specific, cost-effective, and well-suited for multi-modality detection, biosensors for a lab-on-a-chip must tolerate a wide range of operating conditions to be field-deployable. Especially for handheld, point-of-care diagnostics, where the testing environment can be highly variable, it is advantageous to have a sensor with a tunable operating range. Creating a suite of tailored sensors would allow the user

to collect a broad dataset for greater detection confidence and reliability, despite any non-ideal environmental conditions.

To address these requirements, in this thesis, we design, fabricate, and characterize tunable biosensors with compact and low-cost Vertical Cavity Surface Emitting Lasers (VCSELs), integrated detectors, Peltier coolers, photonic crystal slab resonators, and polymer microfluidics. All of the components utilize scalable semiconductor and soft-lithography techniques to significantly reduce the required device footprint, simplify system assembly, and enable large-scale, economical manufacturing. The sensors operate in the visible to near-infrared 650-900 nm wavelength range for low absorption of water, hemoglobin, and other background elements found in tissue or aqueous samples. Moreover, the 670 nm sensors we demonstrate are designed for compatibility with previously characterized monolithically integrated fluorimeters that capitalize on emerging deep-red fluorescent proteins and molecular probes approved for pre-clinical use by the Food and Drug Administration.

In addition to demonstrating single-slab label-free sensing with tunable GaAs-based 670 nm VCSELs, we present the design, fabrication, and characterization of tunable-gap coupled photonic crystal slabs for increased flexibility and sensitivity. Compared with single-slab devices, double-slab designs offer increased intensity enhancement and an opportunity to differentiate captured molecules with an additional dimension of data from a 2D “fingerprint” of intensity spectra for various gap sizes. Moreover, the ability to control and monitor the effect of mechanical forces exerted on cells and tissues in such a diagnostic platform opens the door to real-time, continuous sample analysis for fundamental research in mechanobiology and numerous clinical applications. Both the single-slab and double-slab sensor architectures enable multiplexed, cost-efficient on-chip biosensing, with packaged systems occupying less than one cubic centimeter.

Acknowledgements

The past n years at Stanford have been an amazing journey, made all the more meaningful because of the incredible individuals I have met along the way. First and foremost, I would like to thank my primary advisor, Professor James “The Coach” Harris for his central role in my education and growth. I first met Coach when I was a freshman, and his contagious enthusiasm for a dazzling array of topics drew me to the group. We’ve since then traversed more than a decade, three graduations, and countless hours of interactions – including Saturday evening conference calls, two optics lab floods, and Harris Group themed charades! After mentoring hundreds of Ph.D. students, he still inspires us to seek out meaningful challenges, with seemingly unbounded energy. I am truly grateful for the opportunity to pursue this research and to be a part of the Harris Group family.

I would like to thank my co-advisor Professor Shanhui Fan for his technical guidance and great enthusiasm for this work; I will miss our productive discussions, particularly the joy of hearing “*that’s amaaazing!*” and “*it turns out ... (insert interesting insight here)*.” I am thankful to have had the chance to work closely with the Fan Group students and post-doctoral researchers over the years, and know that I will be keeping an intrigued eye towards what the group investigates moving forward.

I am grateful to have had the chance to interact with Professor Bert Hesselink, both through his courses and in preparing this thesis. His ability to decompose any problem or idea into its key principles – and his passion for guiding his students to do so – is quite simply, inspiring. I also owe Bert many thanks for pointing out early in my graduate career that “the Ph.D. is one of the best times of your life,” as it has made me appreciate the intellectual freedom and aim to make the most of the experience.

I would like to thank Prof. Mark Brongersma, the chair of my Ph.D. defense committee, for his enthusiasm, collaborative spirit, and dedication to teaching. I also owe many thanks to the other professors, visiting scholars, and staff whom I have interacted with here and abroad, for making this field exciting and collaborative.

I especially want to thank Dr. Jingyu Zhang, Dr. Wonjoo Suh, Victor Liu, Prof. Yuzuru Takashima, Prof. Steve Brueck, and our collaborators at the Stanford School of Medicine and Bio-X – it has been an honor to work closely with such talented scientists and engineers. Thanks to Prof. Jan Liphardt at UC Berkeley and Prof. Valerie Weaver at UCSF for interesting discussions about mechanobiology and biomedical applications of this work. My graduate years have also been greatly influenced by a near-constant stream of research mentees who have introduced me to the joys and challenges of teaching. Special thanks to Antonio Cerruto, Min-Chieh Ho, Phil Ponce de Leon, Karine Hsu, Rolf Timp, and Alfred Weschelberger for their curiosity, drive, and open ears.

I am indebted to my industry mentors for broadening my technical background, encouraging my professional development, and for giving me the chance to work on so many exciting projects: Dr. Dave Bour and Dr. Waguih Ishak from Agilent Laboratories, Dr. Chris D'Emic, Dr. John Heidenreich, and Dr. Kathryn Guarini from IBM T.J. Watson Research Center Yorktown Heights, Dr. David Hayden and Dr. Stanford Miller from Intel Hillsboro, and Dr. Todd Ulmer, Dr. Jeffrey Roth, and Dr. Robin Huang from MIT Lincoln Laboratory. I am eternally grateful for the industrial collaborators and colleagues that have helped propel this work when our own resources fell short; special thanks to Dr. Shuwei Chiu of M-Com, Dr. Mary Hibbs-Brenner and the team at Vixar, and Tim Huebner and Nate Geniella of Newport for their support and interest in our research. I would also like to give my sincere thanks to Tim Brand, Pauline Prather, and the Physics Machine Shop team (especially Karlheinz, Matt, and Mehmet) for their amazing help at all hours. This work was supported by DARPA, a Beckman Center grant, Stanford Bio-X,

and fellowships from the National Science Foundation and National Defense Science and Engineering Graduate program.

With so many years in the Harris Group, I have collected a long list of collaborators and friends to acknowledge. I especially want to thank Dr. Evan Thrush, Professor Ofer Levi, Professor Heon Lee, and Dr. Luigi Scaccabarozzi for mentoring me and for their technical interactions, support, and impact on my time at Stanford. I owe great thanks to the Harris Group alumni from my undergraduate days, particularly Professor Lynford Goddard, Professor Seth Bank, Dr. Homan Yuen, Dr. Tom Lee, and Dr. Ke Wang for their advice, encouragement, and friendship. Recent and current Harris Group members have made the final stretch exciting and memorable; thanks to the soon-to-be Dr. Angie Lin, Tomas Sarmiento, Dr. Paul Lim, Robert Chen, Sara Harrison, Dr. Altamash Janjua, Shuang Li, Dong Liang, Sonny Vo, Dr. Yijie Huo, Dr. Ted Kamins and everyone for their camaraderie and support over the years. Tomas and Angie, I'm so glad we started the clan that is "like Quals prep – but instead of trying to get into the Ph.D., we're trying to get out." Grad Prep Group is going to be a worldwide phenomenon. Many thanks also go to our wonderful Gail Chun-Creech, for resolving numerous day-to-day issues and making CIS feel a bit more like home.

My experience at Stanford beyond our research group has been equally amazing. I am thrilled to have met so many fantastic colleagues and friends committed to pursuing interesting research and creating value for our communities. Thanks to the extended d.school family, CHIPSters, NNIN-Brazil nanoscientists, CIS Japan trip teammates, and the enormously talented and diverse photonics student community here for filling the hours outside of lab with exciting activities and great memories. I owe many thanks to Dr. Tom Baer and the SPRC team for helping our student chapter grow by leaps and bounds and broadening my technical and leadership foundations. We have built so many useful programs for the scientific community, and managed to do so with volunteers who have

so many other commitments. We must be doing something right! Special thanks to Dr. Tom O’Sullivan for being an enthusiastic collaborator, fantastic Stanford Optical Society partner-in-crime, and caring cubicle-mate throughout this journey.

I also extend my sincere thanks to my pre-Stanford mentors whose dedication and enthusiasm helped shape who I am today – especially Mr. Steve Schlink, Mme. Mireille McNabb, Mrs. Heidi Strahm Black, Mr. Lambert Woo, Mrs. Jane Owczarzak, Mr. Greg Asplund, Mr. Stafford Baham, Mrs. Freida Murphy, and Dr. Mike Stallard.

My warmest thanks go to my friends, many of them who have passed through the halls of Packard or CIS at some point. If you’re out in the real world, I’m excited that I can finally see you again. If you’re still tied to your optical bench or MATLAB code, I wish you rapid success!

Words cannot express how grateful I am to my boyfriend Elad for his unwavering love, support, and inspiration for the last 11 years. Elad, I’m glad you don’t mind turning restaurant napkins into MEMS prototypes, understand the urgency of an intermittent short circuit, and sometimes laugh at my photonics puns. The journey and the destination would not mean the same without you and your supportive family.

Finally, to my mom and dad, grandparents, brother Jeff, and the rest of my family: thank you for always being there for me, and for trying to refrain from asking me when I would graduate and leave The Farm. Your unconditional support and encouragement has allowed me to grow long before I knew what a photon was, and for that, I dedicate this thesis to you.

Table of Contents

Abstract	v
Acknowledgements.....	vii
Table of Contents	xi
List of Tables.....	xiv
List of Figures.....	xv
Chapter 1 Introduction.....	1
1.1 Organization	5
Chapter 2 Lab-on-a-Chip Systems	10
2.1 Biosensor Fundamentals	12
2.2 Transduction Mechanisms	14
2.2.1 A Closer Look at Fluorescence	17
2.3 VCSELs for Portable Sensing	20
2.4 Label-Free Optical Sensing.....	27
2.5 Introduction to Sensor Figures of Merit.....	30
2.6 Summary	34
Chapter 3 Photonic Crystal Slabs for Label-Free Sensing	36
3.1 Introduction to Guided Resonances.....	38
3.2 Properties of Guided Resonances	40
3.3 Design and Simulation for VIS-NIR.....	41
3.4 Summary	49
Chapter 4 Sensor Fabrication and Characterization	51
4.1 Integrated TEC, VCSEL, and Detector Module	52
4.1.1 Design and Fabrication.....	52
4.1.2 Packaging and Measurement Setup	61
4.1.3 TEC Performance.....	66
4.1.4 VCSEL Performance	68
4.2 Photonic Crystal Slabs and Fluidic Delivery.....	79
4.2.1 Thin Film Deposition	79
4.2.2 Interference Lithography.....	80

4.2.3 Etching	83
4.2.4 Nanoimprint Lithography Alternatives	85
4.2.5 Surface Treatment Studies	86
4.2.6 Fluidic Chamber Construction	88
4.3 Photonic Crystal Resonance Characterization.....	90
4.4 Summary.....	95
 Chapter 5 Refractive Index Sensing with Tunable VCSELs	97
5.1 Testing Setup	98
5.2 Bulk Sensing Results	102
5.3 Off-Normal Incidence and Drift in Realistic Systems	108
5.4 Label-Free Optical Biosensor Comparison	111
5.4.1 Temperature Sensitivity and Drift.....	115
5.5 Microfluidics Integration	118
5.6 Summary.....	123
 Chapter 6 Coupled Photonic Crystal Slabs for Sensing.....	125
6.1 Background	126
6.2 Double-Slab Design	130
6.2.1 Simulations	130
6.3 Wedge Approximation Experiment and Results.....	132
6.4 Actuation Design.....	139
6.5 Process Development.....	142
6.6 Summary.....	143
 Chapter 7 Conclusions	145
7.1 Summary.....	146
7.1.1 Label-Free Sensor Design/Fabrication/Characterization	146
7.1.2 Demonstration of Index Sensing with 670 nm VCSELs	148
7.1.3 Examination of Photonic Crystal Angular Dependence	149
7.1.4 Design of Coupled Slabs for Tunable-Gap Devices.....	150
7.2 Future Work.....	151
7.2.1 Increased Simulation and Design Capabilities.....	151
7.2.2 Sensor Component and Array Optimization	153
7.2.3 Interface with Biology and Users	153
7.2.4 Multi-Modality Sensing	154
 Appendix A: Fabrication Techniques.....	156
A.1 Photonic Crystal Slab Process Flow	156

A.1.1 Nanoimprint Lithography	158
A.2 Fluidic Delivery Systems.....	158
A.2.1 Macrofluidics.....	158
A.2.2 Microfluidics	159
A.3 Double Photonic Crystal Slab Process Flow.....	159
 Appendix B: Characterization Setups.....	163
B.1 Photonic Crystal Characterization Equipment	163
B.2 TEC/VCSEL/Detector/Other Characterization Equipment	163

List of Tables

Table 3-1: Typical geometric and materials parameters used to generate guided resonance modes in the VIS-NIR.....42

Table 5-1: Comparison of optical label-free sensor performance.....112

List of Figures

Figure 1-1: Illustration of a typical diagnostic pipeline for a patient, where samples may need to be sent to specialized facilities, resulting in prolonged wait times while tests are completed serially	2
Figure 1-2: Image of a bulky and expensive piece of biomedical diagnostics equipment (left) often used today in research centers, compared to desired portable devices (right) that aim to reduce the size and cost of sensing systems.....	3
Figure 2-1: (a) Schematic of an antibody-antigen lock-and-key pairing. Recognition elements can be engineered for a wide variety of analytes to provide specificity for an assay. (b) Illustration of a chain of affinity-based binding events. These sand-wich assays can employ contrast agents such as a fluorescent tag to improve the limit of detection for small molecules.....	13
Figure 2-2: Schematic of a 3D lab-on-a-chip platform, with arrays of low-cost VCSELs, integrated detectors, and shared fluidic delivery in a compact footprint	17
Figure 2-3: Absorption and emission spectra of the fluorescent dye Cy5.5. Light sources at 670 nm are appropriate for fluorophore excitation	18
Figure 2-4: (a) Epitaxial structure of a monolithically integrated VCSEL and detector. (b) Scanning Electron Microscopy (SEM) image showing blocking layers	22
Figure 2-5: Absorption of the primary elements of tissue, including water, lipids, hemoglobin, and oxyhemoglobin. For both the hemoglobin and oxyhemoglobin curves shown, 10 μM concentrations were assumed for the spectrum calculation to approximate mammalian tissue. Operating in the 650-900 nm region enables sensing with minimal loss.....	23
Figure 2-6: VCSEL mirror reflectivity vs. number of DBR pairs. To reach 99.9% reflectivity, nearly double the number of pairs is needed for VCSELs at 670 nm	

compared to other wavelengths. The DBR materials assumed are AlAs-GaAs for the 980 nm and 1550 nm VCSELs, AlAs-Al _{0.2} Ga _{0.8} As for 850 nm, and AlAs-Al _{0.5} Ga _{0.5} As for 670 nm. Plot courtesy of Tomas Sarmiento, Stanford University	24
Figure 2-7: Scanning Electron Micrograph of a 670 nm monolithically integrated VCSEL/detector unit. A large area detector is chosen to collect ample signal	25
Figure 2-8: Photocurrent measured at the detector for various concentrations of Cy5.5 dye in PBS solution. As described by O’Sullivan et al. [37], the integrated VCSEL and detector was fixed below a transparent plastic well, with solutions introduced from low to high concentration and a buffer rinse in between consecutive concentrations to verify a return to the initial signal	26
Figure 2-9: (a) Schematic of a photonic crystal guided resonance-based label-free sensor and (b) the simulated spectral shift for two different refractive index fluids. The displacement of background fluid upon the binding of an analyte to surface biorecognition elements alters the optical transmission spectrum of the device. Here, the simulated difference between bulk solutions of deionized (DI) water and isopropyl alcohol (IPA) illustrates the shift in the optical spectrum	27
Figure 3-1: A 2D photonic crystal slab, with a square lattice of air holes	38
Figure 3-2: (a) A uniform slab (side view) and its frequency vs. wavevector diagram showing separate radiation and guided modes. (b) The addition of scattering elements, with periodicity a , in a photonic crystal slab causes the guided mode to fold, creating guided resonances that can couple to external radiation. Figure adapted from [90]	39
Figure 3-3: Energy profile (3x3 unit cells shown) on the photonic crystal surface. Intensity hot spots (red) are located outside of the holes (white outline), providing increased field intensity where biorecognition elements would capture analytes and also making the structure robust to sidewall and etching non-uniformities	41

Figure 3-4: Effect of hole diameter on the photonic crystal guided resonance peak location and shape. Simulation results for SiNx on fused silica in air, with hole diameters of 250 nm (orange), 200 nm (blue), and 150 nm (grey) are shown.....	43
Figure 3-5: (a) FDTD simulation of reflection spectra for mixtures of IPA and water. (b) Simulated sensitivity of 130 nm/ RIU	44
Figure 3-6: (a) Simulated reflection spectra for water and IPA above a photonic crystal slab designed for operation at ~675 nm and (b) Simulated peak shift for solutions of different refractive indices (1.333, 1.334, and 1.336).	45
Figure 3-7: Photonic crystal spectra observed when a polarizer is rotated (a) 0° and 90° or (b) 45° show the quality of each resonance.....	47
Figure 3-8: Simulation results for TE and TM off-normal incidence show a substantial change in peak to valley height, but a preserved slope when averaging behavior from a cone of up to 2°.....	48
Figure 4-1: Schematic of a TEC, with the top ceramic plate removed to more easily observe the four P and N (denoted in green and blue) pellet pairs linked in series electrically and in parallel thermally	53
Figure 4-2: Photographs of two types of TECs used to control the VCSEL temperature. (a) A 4-pellet pair unit that needed to be trimmed to fit standard transistor packaging, with the monolithically integrated VCSEL/detector as well as three extra lasers at a different wavelength. (b) An 8-pellet pair TEC device with a slimmer profile. Three lasers are bonded, and a precision thermocouple is attached with conductive epoxy. The next step is the bonding of the monolithically integrated VCSEL/detector in the remaining space on the top metallized plate	55
Figure 4-3: A typical VCSEL structure, with bottom n-contact, GaAs substrate, top and bottom DBRs defining a cavity, quantum wells inside the cavity, and a top ring	

contact. An oxide aperture confines the current and emission occurs normal to the substrate	56
Figure 4-4: Responsivity vs. wavelength for a GaAs photodiode. The roll-off at ~870 nm corresponds to the band gap of GaAs at 1.42 eV	59
Figure 4-5: Layout design of the TO-5 header. A monolithically integrated pair of VCSELs and detector, with two VCSEL p-contacts and the detector readout signal occupying 4 pins, is bonded on an 8-pellet pair TEC. Thicker gold ribbons are used to provide larger ampacity for the TEC biasing. For TECs that are not metallized, a 0.5 mm thick quartz spacer coated with gold is bonded in between the TEC top ceramic plate and the laser dies to provide a ground plane	60
Figure 4-6: Photograph of a trimmed and bonded 4-pellet pair TEC, with an integrated VCSEL/detector, additional VCSELs, and the thermocouple, utilizing a TO-5 transistor header package. After the VCSEL/detector, extra VCSELs, and thermocouple are bonded to the TEC and wired to the header pins, a TO-can enclosure and collimating lens can be added	61
Figure 4-7: Diagram of laboratory testing equipment connections enabling characterization of the TEC/VCSEL/detector and photonic crystal in reflection and transmission, with GPIB protocols and a MATLAB interface	63
Figure 4-8: Measured photocurrent from the integrated detector in (a) reflection and (b) transmission configurations	65
Figure 4-9: (a) TEC/VCSEL/detector packaging enclosure. An aperture is created on a standard TO-cap before it is spray painted matte black to prevent stray reflections, and an aspheric collimating lens is added. (b) The cap fits snugly over the TO-5 headers (shown here in a side view) that hold the TEC/VCSEL/detector	66
Figure 4-10: Time transients were observed, as expected, during thermal tuning. In this example, we cool and heat the VCSEL biased above threshold, by stepping the	

current driving the TEC every 100 seconds. Typical transients last 40 seconds as we ramp the TEC current 50-75 mA every 100 seconds	68
Figure 4-11: LI curve for a 670 nm VCSEL at seven different temperatures set by the TEC.	
The VCSEL current biases shown here represent the full range (5 mA maximum operating current), hence we observe rollover.....	69
Figure 4-12: LI curve at eight different TEC settings (-100 mA, -75 mA, -50 mA, 0 mA, 50 mA, 75 mA, 100 mA, and 125 mA) and their corresponding temperature ranges (~10-15 °C, 15-17 °C, 17-20 °C, 24-27 °C, 32-35 °C, 36-40 °C, 41-45 °C, and 48-51 °C), for a 822 nm VCSEL. Compared to the operating conditions used in Figure 4-11, this VCSEL is being operated at current biases closer to threshold (not reaching the 12 mA maximum operating current)	70
Figure 4-13: Power spectra for a 670 nm VCSEL. Each curve represents an increment of 0.25 mA. A ~0.2 nm FWHM is seen through moderate biases, with approximately more than 3 orders of side mode suppression near threshold.....	72
Figure 4-14: Power spectra for the same 670 nm VCSEL shown in Figure 4-13, now biased from 4 to 5 mA, again in increments of 0.25 mA. The effective FWHM has broadened significantly in this multi-mode regime	73
Figure 4-15: Measured 822 nm VCSEL 3D and top-view beam profile showing single mode, circular beams. Beam profile cameras were used in conjunction with an optical spectrum analyzer to investigate the presence of transverse modes.....	74
Figure 4-16: With the 670 nm VCSEL held above threshold at a low bias of 1.6 mA, temperature tuning provides a precise shift, while preserving the laser's narrow linewidth	75
Figure 4-17: Power of a 670 nm VCSEL biased at 3 mA, where the laser threshold was 1.5 mA, measured for over two hours. The peak-to-peak variation was ~0.7%.	77

Figure 4-18: Stable transmitted power for a 822 nm VCSEL with 50 mA driving the TEC and different VCSEL bias points (3.5 mA, 4 mA, 4.5 mA, 6 mA, and 12 mA shown here), each held for 1000 seconds	78
Figure 4-19: Schematic of the interference lithography setup. A 355 nm Nd:YAG laser is incident on the wafer from two directions, creating an interference pattern at the wafer	82
Figure 4-20: Deposition, lithography, and etch process for 2D photonic crystals.....	83
Figure 4-21: Scanning Electron Microscopy (SEM) images after lithography and etching show the SiNx photonic crystals with pitch 500 nm and hole diameters of ~200 nm, designed for resonances in the VIS-NIR.....	84
Figure 4-22: SEM images taken immediately after using an integrated Focused Ion Beam (FIB) fill the photonic crystal holes with Pt and mill trenches. This allowed for high-contrast imaging of the sidewall shapes to improve processing parameters	84
Figure 4-23: Contact angle images for DI water droplets on SiNx surfaces demonstrate the effect of surface treatments on hydrophobicity. Angles of 45° and 104° were measured for the (a) HMDS and (b) CF ₃ treated samples, respectively	88
Figure 4-24: Illustration and photograph depicting the design and assembly of a macrofluidic chamber for initial tests with a large 12 mm x 12 mm photonic crystal slab. Interferometry flats, index-matching fluid, Kapton tape, a Teflon disc, syringe tips, polyethylene tubing and plastic paraffin sealing film are compatible with standard cage optomechanic mounts	89
Figure 4-25: (a) Cary 500 spectrophotometer and (b) a top view inside the testing chamber, with photonic crystal and macrofluidic cell.....	90
Figure 4-26: Measured reflection spectra from two different photonic crystal samples designed for use with 670 nm VCSELs (left) and 795 or 822 nm VCSELs (right). The sample yielding the 624 nm and 646 nm peaks in air was fabricated with	

nanoimprint lithography and the lower-wavelength resonance (labeled in red) was later used for aqueous sensing (discussed in Chapter 5)	91
Figure 4-27: Measured normalized reflection for a photonic crystal sample in air matches the peak locations predicted by FDTD simulation. Some broadening is hypothesized to occur from off-normal incidence light, as will be discussed in Chapter 5	92
Figure 4-28: Measured normalized reflection for the same photonic crystal sample as shown in Figure 4-27, with DI water compared to FDTD simulations. The photonic crystal probing location was not moved or optimized compared to that used in Figure 4-27 in air, and the non-uniformity likely caused both the blending and 8 nm shift from expected peak values	93
Figure 4-29: Measured normalized reflection for the same photonic crystal sample as shown in Figure 4-27, with DI water. Moderate Qs of 83 and 181 are robust to fabrication defects while providing enhancement for observation of peak-shifting..	94
Figure 4-30: Measured normalized reflection for different water and IPA solutions. With peak fitting, one can differentiate water and 5% IPA solutions clearly, corresponding to a resolved index change of $\sim 1.5 \times 10^{-3}$ RIU	95
Figure 5-1: SEM image and photographs of photonic crystal samples made via nanoimprint lithography. For the photographs on the right, black fabric is placed behind the clear plastic sample container to provide contrast. While local patterning is transferred with high fidelity, the original master quality and adhesion issues can limit the patterned area of samples. Our sample with 144 nm holes on a 400 nm lattice (far right) was utilized for sensing even though it had large unpatterned voids, as it was resonant at wavelengths that corresponded to 670 nm VCSELs	99
Figure 5-2: Non-uniformity of a photonic crystal made with nanoimprint lithography results in different reflection spectra. These curves were taken at locations ~ 1 mm apart.....	100

Figure 5-3: Schematic of the measurement system used to co-align the broadband light source with the VCSEL to probe the same location on the photonic crystal101

Figure 5-4: *In situ* characterization of the photonic crystal slab in air (black) and DI water (blue) shows a shift of 132 nm/RIU. The photonic crystal resonance in aqueous solutions appears to align with the VCSEL wavelength (pink)103

Figure 5-5: Simulated reflection for the photonic crystal with four solutions of DI water/IPA (left), compared with experimental results for normalized reflection utilizing a VCSEL source. We see 25% change in transmission between DI water and 50% IPA, corresponding to $\sim 10^{-4}$ RIU detection104

Figure 5-6: Extended tuning range of the 670 nm VCSEL, compiled from Lorentzian fits of OSA spectra for different temperature (TEC bias) and current biasing conditions. Single-mode operation provides less than 0.08nm FWHM linewidth for precise control of wavelength, and transverse multi-mode operation yields ~ 0.5 nm FWHM linewidth. The total tuning range with a combination of temperature and current tuning is 3 nm. To generate the graph in the center, temperatures ranged from ~ 8 °C to ~ 50 °C, corresponding to four TEC bias points of -350 mA (black), 0 mA (grey), 150 mA, and 275 mA (both orange).106

Figure 5-7: Reflection spectra for a photonic crystal design with two guided resonant modes at ~ 800 nm shown for (a) normal incidence, 1°, 2°, and 4°, and (b) normal incidence, 4°, 7.5°, and 9°109

Figure 5-8: Simulated photonic crystal spectral response for an incoming source beam with a finite divergence angle of 7.5° $1/e^2$ half width. The VCSEL incident beam is approximated by a superposition of plane waves at different incidence angles, with a Gaussian amplitude distribution with respect to the angle from normal incidence. The reflection spectra were numerically integrated up to a maximum full angular

width of 15° at each wavelength and summed over equal amplitudes of both polarizations	110
Figure 5-9: Schematic for two microfluidic chips, featuring a valved control line and a flow line for the aqueous solution delivered to the photonic crystal.....	119
Figure 5-10: Photographs of two-layer microfluidic chip with a 3.2 mm x 3.2 mm reservoir mounted on photonic crystal slab. Stainless steel 23 gauge tubing is used for inlets and outlets	120
Figure 5-11: CAD schematic of three-layer microfluidic chip to enable more complexity without requiring a larger photonic crystal substrate to seal the entire area. The control layer (red) regulates flow of the middle fluidic layer (blue) with pneumatic valves. Dead end channels (blue) overlap a reservoir (purple) in the third layer	121
Figure 5-12: CAD schematic of fluid layers, showing dead end channels (red), punch through connections (navy) and the reservoir (cyan). The z axis is scaled 100x to show the connections	121
Figure 5-13: Photograph of a three-layer microfluidic chip with a photonic crystal sealing the chamber. For size reference, the smaller microfluidic chip and a United States penny are shown to the left.....	122
Figure 5-14: A pneumatic manifold and the corresponding valves designed for use with the control layer of the microfluidic chips shown in Figures 5-10 and 5-13. The valves are operated with a MATLAB user interface for rapid pumping, mixing, and flushing.....	122
Figure 6-1: (a) Illustration of a double photonic crystal slab system. (b) Example of a 2D spectrum from [131], simulated for a pair of photonic crystal slabs, with intensity spectra for various gap distances.....	127
Figure 6-2: Schematic of a double slab system to simultaneously monitor a tissue sample's optical and mechanical response to compression and extension forces. In a cost-	

effective cartridge-style system, piezoelectric transducers can bring the two slabs together, compressing elastic spacers129

Figure 6-3: Simulated field profile for a double slab structure (each slab is shown in purple). The square of the electric field for a double slab configuration is shown in red; the value is $\sim 20x$ greater than the case for a single slab (shown in blue). The field values were In addition to the 20x peak field enhancement, the coupled slab system enables more efficient overlap of the field profile with the analytes, in an accessible volume between the slabs.....131

Figure 6-4: Schematic of the wedge approximation characterization setup. A fiber-coupled white light source can probe different effective gaps between the two photonic crystals in a static structure. For the $5\text{ }\mu\text{m}$ shim, an angle of 0.03 degrees is formed between the slabs. The beam spot size ($\sim 500\text{ }\mu\text{m}$) covers ~ 1000 periods and a difference in gaps of $\sim 260\text{ nm}$ 132

Figure 6-5: Photograph of the two photonic crystal slabs, with a $5\text{ }\mu\text{m}$ shim inserted between them on one side, and the rounded edge on the opposite side. Three clamps are shown; the sample holder allowed for additional clamps if needed to adjust the flatness of the samples134

Figure 6-6: The sample mount (depicted as a transparent square in the illustration to allow visualization of the layers below) is attached to a pair of stacked crossed-roller bearing linear stages with apertures. Clamps (not shown) secure the photonic crystal slabs and the shim in between the slabs.135

Figure 6-7: Photograph of the double-slab wedge experimental setup, with a QTH fiber-coupled light source, motion controlled sample stage, and fiber spectrometer, with a camera used for alignment136

Figure 6-8: Experimental spectra as a function of gap for coupled photonic crystal slabs in a wedge configuration (top) correlate with simulation data (bottom). The color bar indicates normalized transmission intensity.....	137
Figure 6-9: (a) A double photonic crystal slab on thick fused silica with trenched polymer spacers (in yellow) enables a large percentage of compression relative to the exposed spacer volume. (b) A top view showing actuation contact points (blue) and capacitance pads (red) for measuring the gap.....	139
Figure 6-10: COMSOL simulations show that increasing the top substrate thickness by a couple of millimeters improves the flatness (and hence gap uniformity) during actuation.....	141
Figure 6-11: Photographs taken during the thick-substrate photonic crystal fabrication process. (a) Interferometry was used to estimate flatness and parallelism. (b) Thinned rims were compatible with existing wafer holders and equipment. (c) Increased vacuum suction was needed during wafer spinning. (d) SiNx was deposited via PECVD, using a process similar to that described in Chapter 4 for standard thickness wafers. (e) 4-inch wafers fit into existing etchers. (f) Interference lithography was used to pattern the thick wafer with nine large area photonic crystals	142

Chapter 1

Introduction

“They died by the hundreds, both day and night, and all were thrown in ditches and covered with earth. And as soon as those ditches were filled, more were dug. And so many died that all believed it was the end of the world.”

- *The Plague in Siena: An Italian Chronicle*

The Black Plague, one of the most devastating pandemics in human history, is estimated to have killed 45 to 50 percent of the European population during a five-year period, reducing the world's population from nearly 450 million to 350 million at the end of the 14th century [1]. Medical knowledge had stagnated, and by many accounts had even declined during the Middle Ages, leaving communities without reasonable public health guidelines or measures to prevent the spread of disease.

Although much progress has been made since the days of the Black Plague, particularly with the advent of vaccinations in the 18th century [2], the prevalence and spread of infectious diseases is still of utmost concern. In particular, current trends in both disease etiology and transmission methods pose an acute threat. Approximately 75 percent of new diseases affecting humans in the past decade are zoonotic, often traceable to an unexpected breach in the species barrier between humans and animals [3]. Such diseases can rapidly adapt to attack new hosts, and consequently are at higher risk to

escalate into a worldwide outbreak. In recent years, new diseases have been emerging at a historically unprecedented rate; from 2002-2007 alone, the World Health Organization verified more than 1,100 epidemic events worldwide [4]. With increasing international travel and commerce, if we do not create global technological infrastructure to monitor and quickly respond to such events, all countries are vulnerable to these emerging biomedical threats.

The development of new monitoring technologies promises to alter the treatment of not only rapid-onset epidemics, but also longer-term and more common diseases. In industrialized countries, the leading causes of death and disability are chronic diseases such as diabetes, cardiovascular conditions, and many forms of cancer. A patient's prognosis and quality of life is often largely impacted by the timeliness of detection and the ability to determine the efficacy of treatments; consequently, there is a large unmet demand for ubiquitous diagnostic and continuous monitoring tools. Instead of waiting

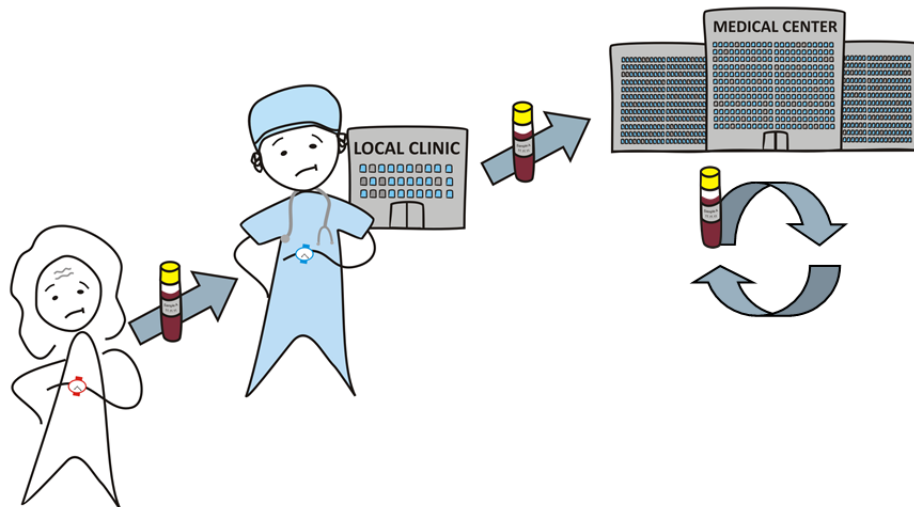


Figure 1-1: Illustration of a typical diagnostic pipeline for a patient, where samples may need to be sent to specialized facilities, resulting in prolonged wait times while tests are completed serially.

days or weeks for medical test results, as illustrated in Figure 1-1, one could imagine cost-effective, portable systems that allow for frequent monitoring at the point-of-care. Moreover, the creation of more readily accessible biomedical sensors would open the door to large-scale distribution, particularly in resource-limited areas of the world where diseases that can be controlled and treated in the developed world are often life-threatening. Whether we aim to continuously monitor the effectiveness of new drug therapies in state-of-the-art research laboratories, or aspire to deploy basic disease screening tools in developing countries, it is clear that our worldwide health diagnostic demands continue to rapidly outgrow our capabilities.

The central roadblocks to pervasive medical diagnostics are the size and cost of reliable biochemical analysis systems. Many of the options available today are bulky, expensive, slow, and often require specialized personnel to run one test at a time. For example, a fluorescence system like the one shown in Figure 1-2 can easily cost \$500 000 or more, weigh hundreds of kilograms, and occupy a few cubic meters.

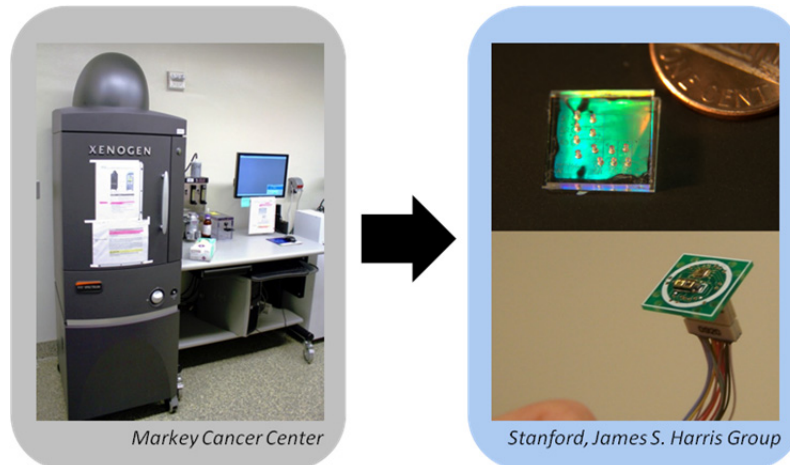


Figure 1-2: Image of a bulky and expensive piece of biomedical diagnostics equipment (left) often used today in research centers, compared to desired portable devices (right) that aim to reduce the size and cost of sensing systems.

Scaling down the size of each piece of these analysis systems in hopes of generating a handheld point-of-care biosensor is problematic because of challenges that arise in maintaining detection capabilities, as well as difficulties in the production and assembly of miniature components. As a result, there is great interest in designing biochemical analysis systems that can not only capitalize on established manufacturing technology, but also leverage novel nanoscale phenomena to maximize detection performance. Employing cost-effective integrated semiconductor microfabrication technology and concepts from the growing field of nanophotonics, we aim to design new devices that reduce overall device sizes and costs substantially, while maintaining adequate sensitivity and specificity compared with existing systems.

There are a number of additional benefits from shrinking the size and cost of a biochemical analysis system. One significant advantage is that smaller, economical sensors make it possible to produce arrays of devices for multiplexed experiments and personalized assay sequences on a single lab-on-a-chip. One can imagine, for instance, sending a biological sample through a series of parallel tests, with the real-time results of the first tests determining where the sample should be routed for subsequent on-chip assays. The criteria for routing the sample through the relevant tests could be programmed ahead of time and monitored remotely if needed, so that the device could be utilized in the field, with only the patient and any modestly-trained medical personnel present. Utilizing semiconductor processing, where the placement of devices is easily defined lithographically, will enable rapid, parallel measurements and personalized test sequences that are cost-effective enough to be part of a disposable or recyclable lab-on-a-chip system.

Besides being compact, sensitive, specific, and cost-effective, biosensors for a lab-on-a-chip must tolerate a wide range of operating conditions to be field-deployable. Especially for point-of-care diagnostics, where the testing environment can be highly variable, it would be advantageous to have sensors with tunable operating ranges. Creating a suite of sensors (for example, with different operating wavelengths, temperature ranges, and biochemical surface configurations) would allow the user to collect an extensive dataset for greater detection certainty, despite any non-ideal environmental conditions.

To address these requirements, in this thesis, we design and demonstrate tunable biosensors with compact and cost-effective light sources, detectors, photonic crystal sensing surfaces, and microfluidics. All of the components are fabricated with scalable semiconductor and soft-lithography techniques to significantly reduce the required device footprint, simplify system assembly, and enable large-scale, low-cost manufacturing. With the goal of prototyping a fully integrated portable analysis platform with multiple sensing mechanisms for correlated measurements, we focus on label-free detection that can be deployed side-by-side with established fluorescence techniques.

1.1 Organization

The first introductory chapter, “Lab-on-a-Chip Systems,” highlights progress in the rapidly growing field of portable biosensing. A review of various detection mechanisms is presented, with an emphasis on optical, label-free techniques, as they require minimal sample preparation and are well-suited for multi-modality¹ systems. In

¹ I.e., allowing for parallel, simultaneous measurements from different sensing mechanisms, such as absorption and scattering or fluorescence and absorption.

particular, we note the importance of compatibility with widely-used fluorescence techniques in the visible to near-infrared (VIS-NIR) wavelength range, and the opportunity to design parallel multi-modality sensors with arrayable sources and detectors. The chapter includes an introduction to a biosensor’s performance metrics and describes some of the primary points of comparison between sensor designs, such as a system’s sensitivity, signal-to-noise ratio, and operating range. In order to address the global need for widely-deployable disease detection and monitoring systems, this thesis concentrates on designs that can take advantage of monolithically integrated Vertical Cavity Surface Emitting Lasers (VCSELs) and detectors to dramatically reduce device size and cost, while maintaining adequate sensitivity, signal-to-noise ratio, and ease of use.

Designs featuring nanofabricated resonant optical structures can address the challenge of maintaining performance within a small footprint. In particular, one efficient and compact way to achieve enhanced interaction between a probing light source (whether the source is a VCSEL or an alternative) and any biomolecules of interest is to employ photonic crystals to trap the light at a surface where biological samples will adhere. Chapter 3, “Photonic Crystal Slabs for Label-Free Sensing,” introduces the physics of the guided resonances in the photonic crystals utilized in our sensor designs. We examine design parameters and present simulation results for operation in the desirable VIS-NIR “tissue transparency window,” where one can benefit from low absorption of water, lipids, hemoglobin, and oxyhemoglobin that would normally reduce the signal contrast of target biological samples.

With these motivations in mind, Chapter 4, “Sensor Fabrication and Characterization,” describes the challenges and rationale behind the fabrication and packaging techniques used for each sensor element, and presents characterization results.

Since the label-free sensor aims to evade bulky and expensive equipment in favor of tunable VCSELs and detectors, the TEC/VCSEL tuning range, intensity stability, and behavior as a function of biasing conditions are of utmost importance. Thus, several performance metrics including noise, transients, and the mode profile were measured. The TEC/VCSEL/detector module is designed to be paired with a photonic crystal that has resonance in the VCSEL tuning range. Hence, we utilize a combination of semiconductor processing, optical interference lithography, and soft-lithography techniques to create low-loss, all-dielectric photonic crystals in the 650-900 nm regime. The photonic crystal slab resonances are characterized to yield a measured sensitivity of 130 nm per refractive index unit (RIU), first as part of a system with broadband sources, spectrometers, and a large fluidic reservoir.

Chapter 5, “Refractive Index Sensing with Tunable VCSELs,” demonstrates the label-free sensor sensitivity using solvent dilutions with the photonic crystal slab and temperature and current tuned VCSELs. This represents a significant reduction in the system footprint; the fiber-coupled white light source and optical spectrum analyzers or spectrometers used in Chapter 4 are now replaced by integrated lasers and detectors packaged to be less than 1 cm³. In order to enable multi-modality sensing - in particular, parallel fluorescence and label-free sensing - for increased diagnostic confidence, we demonstrate a sensor system of VCSELs, detectors, and photonic crystals operating at 670 nm. This wavelength choice is crucial to enable compatibility with fluorescence sensors that take advantage of emerging deep-red fluorescent proteins [5, 6] or early cancer marker molecular probes approved for pre-clinical use by the Food and Drug Administration (FDA) [7-9]. Refractive index sensing shows differentiation of bulk solutions with a 25% change in transmission for 50% (v/v) isopropyl alcohol (IPA) and deionized (DI) water using the tuned 670 nm VCSEL, corresponding to an estimated

limit-of-detection of 10^{-4} RIU. While the initial measured sensitivity is less than the best reported performance of other label-free sensors, the utilization of VCSELs and integrated detectors for this platform has several advantages due to its compact size, scalability, and cost-effectiveness. To elaborate upon these tradeoffs, we include a critical comparison of this work with other optical label-free sensor results published in literature. Furthermore, we discuss key insights about photonic crystal angular dependence and realistic beams that can aid the development of future tunable designs.

In addition to the optical component integration and characterization, the miniaturization of the fluidic delivery system is an essential step in the development of a complete portable diagnostic device. Polydimethylsiloxane (PDMS) microfluidic chips are thus designed and fabricated, providing rapid fluidic delivery, mixing, and flushing for the next generation of experiments.

To increase the detection sensitivity and gain operating flexibility, Chapter 6, “Coupled Photonic Crystal Slabs for Sensing,” introduces a design for a tunable-gap double photonic crystal slab sensor. Simulations that indicate a 20x enhancement in field intensity at the photonic crystal slab surface compared to single-slab designs are presented. In addition to this intensity enhancement for a given gap size, the tunable-gap design yields a 2D spectrum “fingerprint” over different gap distances instead of a typical single-slab intensity spectrum, providing another dimension of data useful for optimizing the sensor architecture for specific analytes and for more precisely differentiating captured molecules.

To experimentally verify the coupled photonic crystal slab resonances over a continuous range of gap distances, we construct a wedge-based setup, collecting

measurement data that agrees with results expected from simulations. Furthermore, we present a piezoelectric and polymer-based tunable coupled photonic crystal slab device design and fabrication process that can provide stable mechanical forces on analytes such as cells or tissues. This functionality can be utilized for a number of mechanobiology applications, such as correlating a tissue sample's mechanical and optical properties with tumor progression. The double-slab architecture offers real-time analysis for rapid feedback in a customizable yet cost-effective measurement platform that is well-suited for parallel testing. Finally, in Chapter 7, we conclude with a summary and a discussion of possible future research directions that span a wide range of biomedical applications.

Chapter 2

Lab-on-a-Chip Systems

"First to fall over when the atmosphere is less than perfect/ your sensibilities are shaken by the slightest defect/ you live your life like a canary in a coalmine."

- *The Police, Zenyatta Mondatta*

Throughout most of the 20th century, canary birds and mice were routinely used as an early warning system for toxic gases in coalmines [10]. The small animals, particularly the vocal canary, were sensitive to the presence of carbon monoxide, and provided a quick method of detection to warn miners. By 1986, however, the British government began to phase out the use of canaries in favor of more cost-effective and efficient handheld electronic gas detectors.

In a similar manner, over the last few decades, research efforts have begun to focus on the development of portable detection systems for a wide spectrum of applications, from environmental monitoring to biomedical sensing. The combination of multiple laboratory functions – such as purification, mixing, and measurement – onto a single lab-on-a-chip promises to provide efficient sample handling and rapid analysis in a compact device. Moreover, the development of integrated lab-on-a-chip systems that can

incorporate multi-modality sensing would enable correlated measurements for new analysis capabilities and more thorough diagnostics.

Combined with the growing prevalence and improved accessibility of biomedical databases, more quantitative diagnostic tools will allow us to effectively study diseases and their spread in our communities. Various organizations are beginning to offer data aggregation services, collecting media reports and user-submitted entries in hopes of being able to track and mitigate the spread of disease. Indeed, in a radical departure from previous international conventions, the International Health Regulations (IHR) in 2005 explicitly acknowledged that non-state sources of information about outbreaks will often pre-empt official notifications, and the World Health Organization (WHO) is now authorized to take information sources other than official notifications into account [4]. However, for emerging data visualization tools to accurately reflect the rapidly-changing nature of public health, one must move beyond reports and user entries that are difficult to validate. A common platform of quantitative and calibrated diagnostic devices in lab-on-a-chip systems could serve as the much-needed hardware infrastructure for global health monitoring.

Rapid and portable diagnostics are particularly important in areas of the world that are resource-limited; in rural communities, a patient could journey to a clinic outpost, but not be able to stay more than a few hours before returning home. If test results are not ready in this timeframe, the patient may never revisit and opportunities for treatment, monitoring, or containment of problematic strains of diseases could be lost. In a similar vein, real-time portable diagnostic tools have the potential to greatly change the landscape of modern healthcare in developed communities. Cost-effective implementation of such technologies would provide an opportunity to continuously

monitor a patient during open surgery, or even constantly during daily activities, to study and treat the development of medical conditions with unprecedented time-resolution. In particular, for diseases where the effectiveness of specific therapies is unknown, one can collect valuable information for critical feedback during treatment.

With these motivations in mind, this chapter reviews lab-on-a-chip sensing principles and mechanisms, noting an opportunity to utilize semiconductor optoelectronics, particularly VCSELs, as cost-effective components that allow for wafer-scale manufacturing and integration. We discuss the benefits and tradeoffs of various sensing methods, with a focus on optical label-free techniques that enable multi-modality tests at clinically relevant operating wavelengths.

2.1 Biosensor Fundamentals

A biosensor is a device that detects an analyte, which is defined as a chemical component of interest, such as a virus or an antibody. Today's biosensing systems are often classified by the type of biological element employed to capture the analyte, and the mode of detection or transduction. The biorecognition elements, or bioreceptors, used to capture analytes can include enzymes, proteins, nucleic acids, or whole living systems such as cells or tissues. A “lock-and-key” pairing of a biorecognition element with its corresponding analyte, as illustrated in Figure 2-1a, provides specificity. With the diverse choice of antibodies possible (humans alone have $\sim 10^8$), there are many biomolecules than can be detected directly. In addition, one can use sandwich assays where a secondary molecule facilitates detection of entities that may be otherwise too small to be detectable. Moreover, in a chain of affinity-based detections, contrast agents can provide additional signal amplification, as shown in Figure 2-1b.

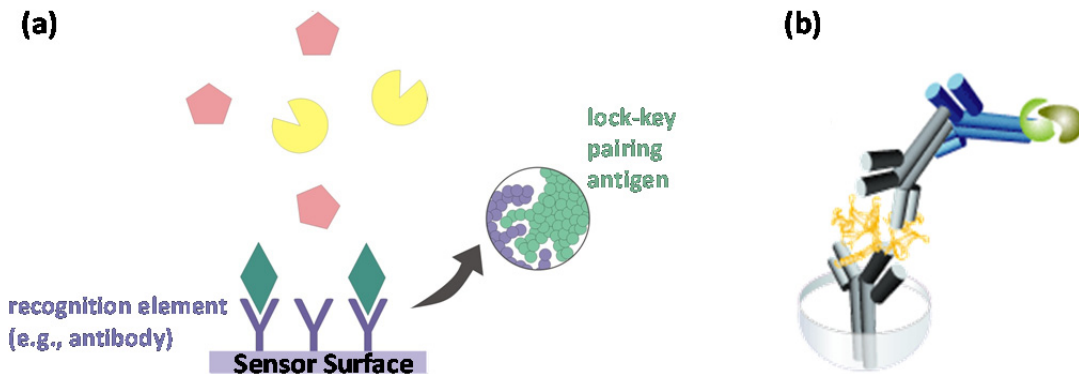


Figure 2-1: (a) Schematic of an antibody-antigen lock-and-key pairing. Recognition elements can be engineered for a wide variety of analytes to provide specificity for an assay. (b) Illustration of a chain of affinity-based binding events. These sandwich assays can employ contrast agents such as a fluorescent tag to improve the limit-of-detection for small molecules.

Although the pairing of a bioreceptor to an analyte is designed to be specific, the quality of surface functionalization methods used can vary. Any non-specific or unintended binding will lower the signal-to-noise ratio and limit the accuracy of the biosensor. A combination of bioreceptor engineering, surface treatments, and flushing procedures can help minimize non-specific binding. As reviewed by Hunt and Armani [11], a diverse set of biological recognition elements can be engineered with the specificities and affinities required for a wide range of analytes. For example, optical sensors have been paired with enzymes, peptides, antibodies, and aptamers. If a recognition element cannot be found or engineered with the correct properties to provide adequate sensor performance, an alternative is the use of molecular imprinting² to form “pockets” of particular sizes and shapes, with specificities (towards a molecule, functional group, or structure) similar to that of antibody-antigen reactions [12-14].

² I.e., a process where transducer surfaces are coated with a solution of plastic monomers and biorecognition molecules. After polymerization, entrapped molecules are removed, yielding rigid template “pockets.”

2.2 Transduction Mechanisms

One can detect that an affinity binding event has occurred through a variety of transduction mechanisms, including magnetic, electrochemical, mechanical, and optical techniques. Magnetics-based lab-on-a-chip approaches include the use of giant magnetoresistance (GMR) [15, 16], as well as optomagnetic and resonance frequency shift techniques where magnetic nanoparticles act as contrast agents. GMR sensors employ materials that exhibit a change in resistance in response to an applied magnetic field.

For example, a typical GMR material can consist of several magnetic layers grown by Molecular Beam Epitaxy (MBE) or deposited from a sputtering tool, with alternating layers of different magnetizations separated by a non-magnetic material such as chromium (Cr). Each of the magnetic layers is designed to be ferromagnetic, and therefore contains ordered magnetic dipoles that align in the same direction if a sufficient magnetic field is applied. The dipoles can be aligned in parallel or anti-parallel directions, resulting in two different resistances. These resistances can be measured by applying an electrical current and measuring a voltage, or by applying a voltage and measuring an electrical current.

This approach has been used to show femtomolar (fM) sensitivity with assay times less than one hour and a dynamic range of 6 orders of magnitude [17]. However, the fabrication and handling of the magnetic labels and magnets that must be used add complexity and cost to the testing procedure, often requiring specialized personnel on-site. Furthermore, one must account for and often engineer against undesired localized magnetic forces that can occur, complicating the interpretation of measured data.

Electrochemical sensors offer quick and sensitive detection, and are particularly attractive for *in vivo* studies, where many chemical compounds of interest have short half-lives. However, bio-fouling³ of critical electrochemical surfaces (i.e., the electrical contact pads) due to molecular adsorption can be a large concern. Recent studies exploring nanoporous gold as a possible electrode material [18] for electrochemical sensors are promising for delaying adsorption to some extent, but further investigation on the time-dependent effects of bio-fouling is needed. Even though many other types of sensors are also susceptible to surface adsorption, we will see in Section 2.3 how optical sensing can take advantage of absorption transparency windows to circumvent this issue.

Another type of transduction is based on mechanical forces and consists of the measurement of small changes in mass, often employing piezoelectric crystals or microfabricated mechanical resonators. The crystals or resonators can be engineered to vibrate at specific frequencies when exposed to an electrical signal, where the oscillation frequency is dependent on the applied electrical signal as well as the crystal or resonator mass. If a binding event occurs, the mass increases and the oscillation frequency changes; this can be measured electrically and is reviewed by O’Sullivan and Guilbault [19]. While the sensitivity of such structures is promising, their fabrication and packaging processes have not yet reached the cost-effectiveness needed for many disposable biosensing applications. Moreover, many of the designs that involve suspended beams and other movable structures exposed to analytes may be difficult to coat with surface treatments, limiting devices to one-time use to avoid residue.

³ I.e., the undesirable accumulation of biological material, often due to protein adsorption, which can cause sensor failure.

Compared with other transduction methods, optical sensing encompasses the largest number of sub-categories, as there are many different types of spectroscopic methods (e.g., absorption, scattering, fluorescence, bioluminescence, Raman) where different optical properties (e.g., amplitude, polarization, decay time, or phase) can be recorded. Optical sensors based upon modern integrated photonics and microfluidics are particularly attractive because they can be compact, lightweight, and low-cost. Light beams are also inherently sterile; the optical sources and detectors can be decoupled from affinity-coated surfaces in contact with the biomolecules, in a disposable cartridge-based configuration. This reduces contamination concerns and allows for continued use of the same light sources and detectors for different samples, keeping per-test costs minimal. Alternatively, if manufactured in large quantities, the scalable optical source/detector modules enable the entire lab-on-a-chip to be disposable or recyclable.

Especially useful for multi-modality sensing, optical approaches provide a way to probe a sample non-destructively, with multiple wavelengths, intensities, or timescales providing a powerful set of data for analysis. This allows us to envision parallel sensors, where the results from different detection modalities, such as fluorescence and label-free sensing, can be compared for greater diagnostic confidence. Ideally, our platform would utilize compact, arrayable sources with different tests sharing not only a layer of sources and detectors, but also microfluidics, sensing surface layers, and electronic readout systems, as depicted in Figure 2-2.

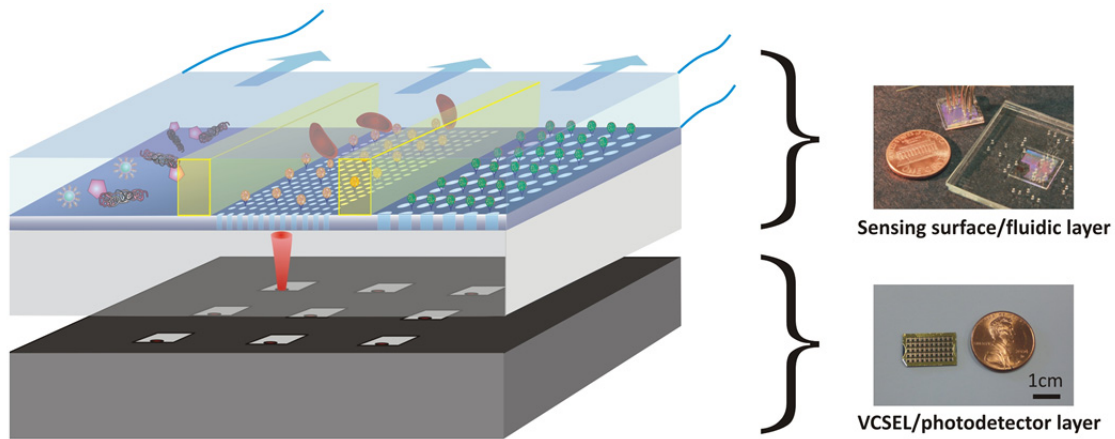


Figure 2-2: Schematic of a 3D lab-on-a-chip platform, with arrays of low-cost VCSELs, integrated detectors, and shared fluidic delivery in a compact footprint.

2.2.1 A Closer Look at Fluorescence

Optical biosensing techniques, albeit often in bulky form factors, are increasingly used in clinical settings and research laboratories. In particular, fluorescence sensing has been an extremely valuable research tool for biochemists and biophysicists for many decades, and is now being utilized for a number of different applications in DNA sequencing, medical diagnostics, forensics, and other fields [20].

Fluorescence sensing is based on the introduction of a fluorescent agent or label into molecules or cells of interest in order to study the molecule's location. As reviewed by Lakowicz and Masters [20], the fluorescent labels, or fluorophores, can absorb optical radiation to enter a higher energy state, and subsequently release the energy in the form of lower energy photons. Typical fluorescent labels excite and emit in the VIS-NIR regions of the electromagnetic spectrum. The absorption and emission spectra of Cyanine 5.5 (Cy5.5) – which is the fluorophore utilized in fluorimeters that can be packaged with the label-free sensors of interest in this dissertation – is shown in Figure 2-3.

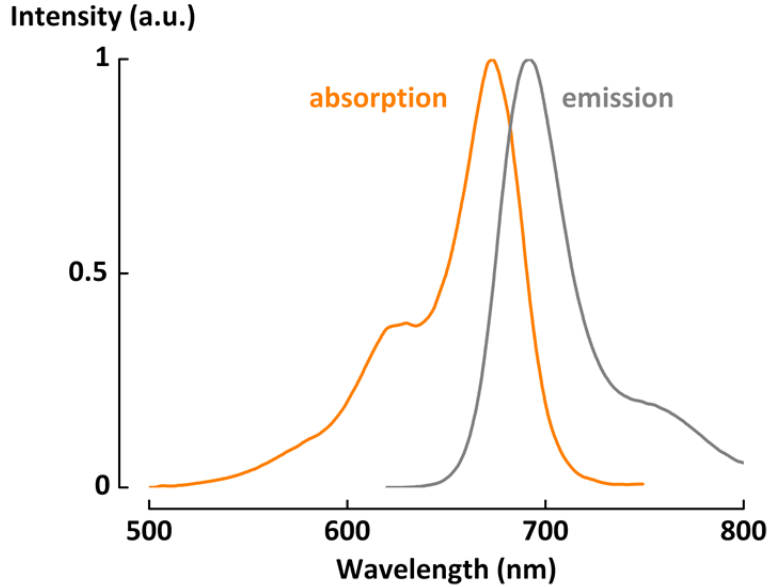


Figure 2-3: Absorption and emission spectra of the fluorescent dye Cy5.5. Light sources at 670 nm are appropriate for fluorophore excitation.

Since there are actually several upper energy states, much like the quasi-continuous electronic bands in semiconductor devices, the allowed energy transitions manifest not as single absorption or emission lines, but as broad spectra. These spectra, combined with the fluorophore's ability to absorb radiation (defined as molar absorptivity, ε) are important metrics to include in the optical sensor design process.

One can derive a simple expression for the amount of fluorescence-induced current expected at a sensor's photodetector [21], given the dye quantum efficiency⁴ QE_{dye} , the detector collection efficiency C_{sensor} , and the fraction of emitted light that is transmitted through an emission filter, T_{filter} . The power incident on the detector is

$$P_D = P_{absorbed} QE_{dye} T_{filter} C_{sensor} \quad (2-1)$$

⁴ I.e., an expression (unitless) of the fraction of photons emitted to the photons absorbed

where the power absorbed by the fluorophores with concentration M and sample thickness d for an excitation power P_{laser} is

$$P_{absorbed} = P_{laser} (1 - 10^{-\varepsilon M d}) \quad (2-2)$$

from the Beer-Lambert Law. Multiplying by the quantum efficiency of the detector, QE_{det} , and dividing by the photon energy hc/λ to convert the optical power in Equation 2-1 to the number of photons, the photocurrent in Amperes can be expressed as

$$I_D = q \frac{\lambda}{hc} P_{laser} QE_{dye} T_{filter} C_{sensor} (1 - 10^{-\varepsilon M d}) \quad (2-3)$$

at the detector. For our fluorescence sensors, which can be monolithically integrated on the same substrate as the label-free sensors developed in this dissertation, the photocurrent expected when operating in a reflection scheme is on the order of picoAmperes (pA) to nanoAmperes (nA).

It is important to note that the excitation background may be orders of magnitude higher than the signal, requiring a high dynamic range detector. With the excitation and sensing originating from the same direction, and the emission intensity typically being 4-5 orders of magnitude less than the excitation intensity, high quality emission filters are also required for fluorescence sensing. For *in vivo* applications, both backscattered light as well as an animal's autofluorescence contribute to the background, meaning the detector must be sensitive to low photon fluxes, on the order of $\sim 10^8$ photons/sec/cm²/str (the autofluorescence for a mouse at 675 nm). These design concerns and other figures of merit for optical biosensor systems are discussed further throughout the thesis, and reviewed at the end of Chapter 5.

With few exceptions, conventional *in vivo* fluorescence systems require the animal subject to be anesthetized or immobilized to avoid any movement during testing. Those approaches that do accommodate animal subject movement, such as the Invitrogen/Xenogen IVIS Kinetic pictured in Figure 1-2, confine the animal in a dark chamber during imaging, and employ large format excitation light sources as well as cooled or intensified charge coupled devices (CCDs) in a bulky platform. A number of groups have attempted to miniaturize fluorescence instruments, as reviewed by Dandin *et al.* [22], for improved cost, speed, and portability.

Recent work with optical fiber-based components demonstrated fluorescence-based neural imaging in freely-moving small animals [23-25], but required a tether to bulky external light sources. As we will see in the following section, the use of VCSEL technologies can enable a dramatic reduction in device size, making the entire system implantable to permit a full range of un-tethered subject motion.

2.3 VCSELs for Portable Sensing

From fluorescence and refractive index sensing to Raman and bioluminescence techniques, optical biosensing systems today often rely on bulky external light sources and delicate alignment procedures that are not realistic for handheld or implantable sensors. Light emitting diodes (LEDs) and VCSELs represent more portable, robust, and compact alternatives. LEDs can be useful in benchtop and point-of-care systems that do not require a narrow linewidth, directionality, or high power per footprint.

In contrast to LEDs, VCSELs offer a much more narrow linewidth, concentrating the optical power to a full-width-half-maximum (FWHM) wavelength span of less than

0.5 nm even in transverse multi-mode operation (compared to greater than 30 nm in many LEDs). This is important for fluorescence sensors, where the emission peaks of fluorophores may be less than 20 nm away from their excitation peaks. Likewise, we will see in Chapter 5 that for label-free sensors, this narrow linewidth is crucial for obtaining high resolution transmission spectra without bulky wavelength meters and optical spectrum analyzers. With low divergence and a circular output beam that emits upwards, perpendicular from the wafer surface, VCSELs are easily coupled to a variety of other structures. Moreover, VCSELs are arrayable and are easily manufactured and tested on the wafer-scale, providing extremely cost-effective solutions. In fact, 850 nm VCSELs represent the largest volume of any laser produced today, with tens of millions of units fabricated per month.

VCSELs have been explored for affinity-based biosensing in the 790-850 nm wavelength range, with external PIN detectors, beam splitters, and large spectrometers or wavelength meters [26-29]. In contrast to these benchtop systems, monolithic integration provides several advantages. Indeed, as early as 1991, Hasnain *et al.* grew a detector on top of a VCSEL for laser stabilization and control applications at 850 nm [30]. Our group has demonstrated [31-38] that high quality VCSELs and detectors can be integrated monolithically for sensing applications, as shown in Figure 2-4, with emission filters and metal blocking layers to enhance sensitivity performance. The topology of the VCSEL lends itself to elegant process assimilation, with detectors that can be grown directly above [37] or below [33] the laser structure. This approach represents the most compact integration possible, offering dense arrays of sources and detectors defined lithographically with spacing on the order of microns. Such integration also enables reduced fabrication, testing, and packaging costs.

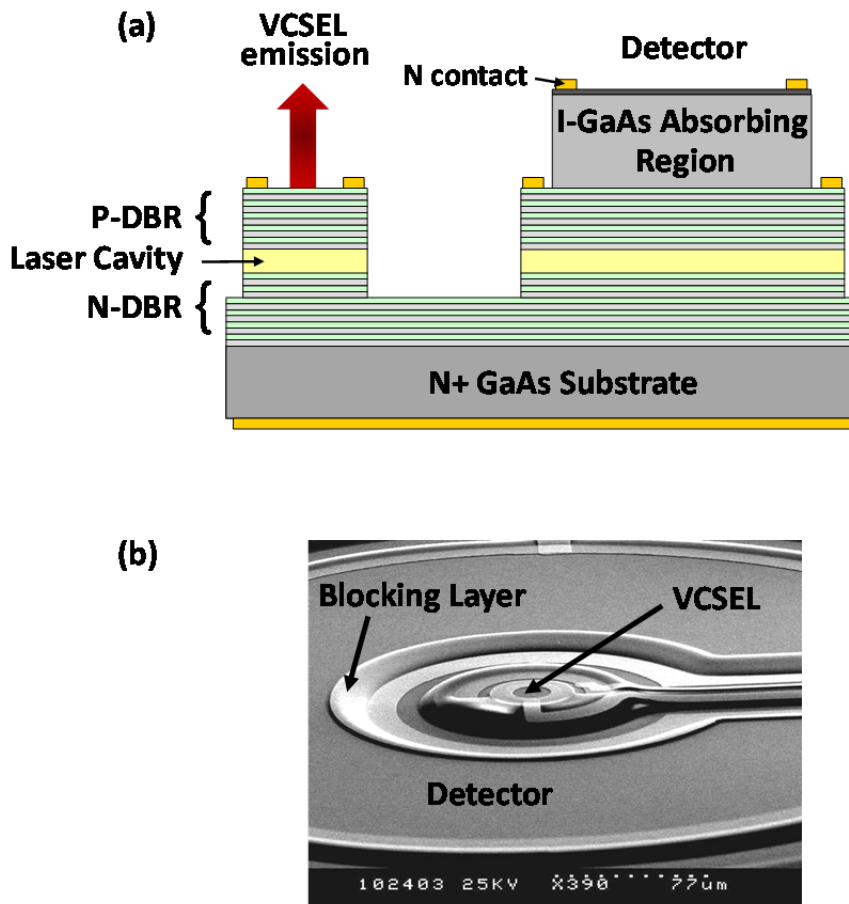


Figure 2-4: (a) Epitaxial structure of a monolithically integrated VCSEL and detector. (b) Scanning Electron Microscopy (SEM) image showing blocking layers.

Our group's initial designs for the integrated VCSEL/detector targeted the 800 nm operating regime, for use with IR-800 fluorescent dye. In choosing the operating wavelength, both the ease of fabrication as well as the potential biological application spaces (at the time) were considered. Creating VCSEL/detector modules at 800 nm allowed for fairly straightforward growth with the AlGaAs/GaAs material system, and resulted in devices well within the desirable 650-900 nm transparency window depicted in Figure 2-5. Operating in this low-absorption region can help circumvent problems with bio-fouling, since the primary elements of tissue do not significantly disrupt the optical signal in the VIS-NIR span.

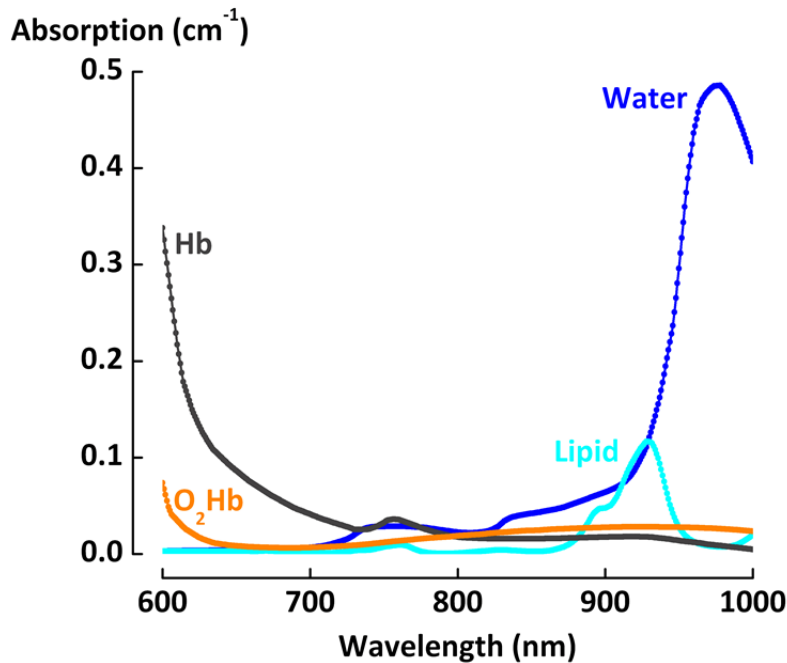


Figure 2-5: Absorption of the primary elements of tissue, including water, lipids, hemoglobin, and oxyhemoglobin. For both the hemoglobin and oxyhemoglobin curves shown, $10 \mu\text{M}$ concentrations were assumed for the spectrum calculation to approximate mammalian tissue. Operating in the 650-900 nm region enables sensing with minimal loss.

As one moves away from the 800-850 nm wavelength regime, either to longer or shorter wavelengths, the epitaxial growth and fabrication challenges quickly increase. For shorter wavelengths, the higher aluminum content needed in the AlGaAs layers in order to not be absorbing results in less index contrast between the distributed Bragg reflectors (DBRs). Consequently, a VCSEL lasing at 670 nm requires nearly double the number of quarter wavelength mirror layers compared to a VCSEL at 980 nm. Figure 2-6 shows the calculated reflectivity of AlAs/Al(Ga)As DBRs versus the number of DBR pairs at different wavelengths. The thicker mirrors required to reach adequate reflectivity translate into a lower thermal conductivity, creating significant design challenges in thermal management.

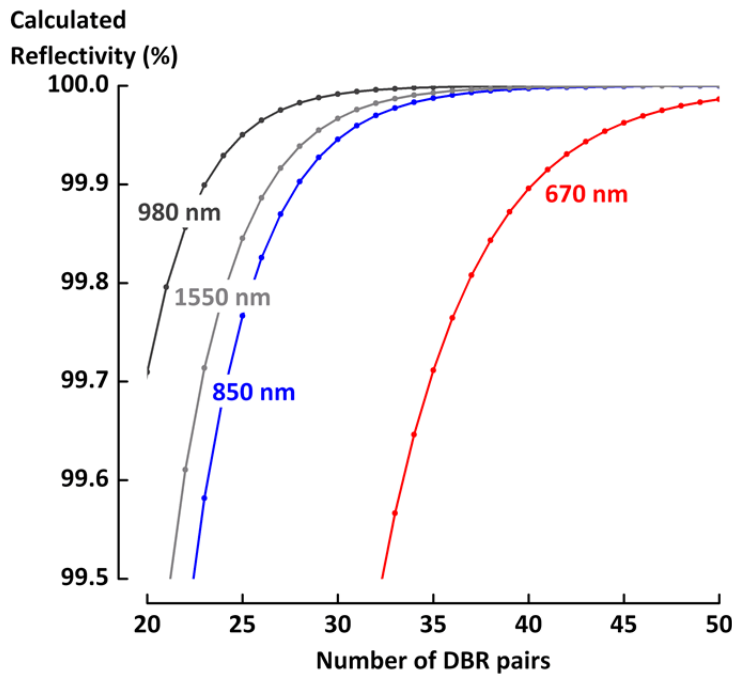


Figure 2-6: VCSEL mirror reflectivity vs. number of DBR pairs. To reach 99.9% reflectivity, nearly double the number of pairs is needed for VCSELs at 670 nm compared to other wavelengths. The DBR materials assumed are AlAs-GaAs for the 980 nm and 1550 nm VCSELs, AlAs-Al_{0.2}Ga_{0.8}As for 850 nm, and AlAs-Al_{0.5}Ga_{0.5}As for 670 nm. Plot courtesy of Tomas Sarmiento, Stanford University.

Despite the multitude of device design and fabrication challenges, substantial effort has been made by several groups in attempts to realize high power short-wavelength VCSELs [39-41]. Recently, with the development of improved surface passivation techniques, metal blocking layers, spectral filtering, and processing optimization, our GaAs-based monolithically integrated VCSEL and detector has been extended to 670 nm (Figure 2-7) [37, 42]. This is significant for biosensing applications, as it allows us to take advantage of newly emerging deep-red and NIR fluorescent proteins as well as fluorescent dyes which are FDA-approved and already in pre-clinical use. With the FDA approval process taking many years, the incorporation of pre-approved markers shortens assay development and can increase the likelihood of device commercialization.

For many fluorescence sensing applications requiring high sensitivity and rejection of backscattered excitation light, sensors are packaged with an external optical emission filter, including both absorption and interference components bonded directly to the photodetector. Combined with a monolithically integrated dielectric-based notch filter, the multilayer stack filter was found to reject over five orders of magnitude of 675 nm excitation light up to an acceptance angle of 30° from normal. This has been sufficient to sense concentrations of Cy5.5 down to 5 nM *in vitro* with dilutions in phosphate buffered saline (PBS) (Figure 2-8), and 50 nM *in vivo*, which is limited by the autofluorescence of the animal subject, and not the device itself [21].

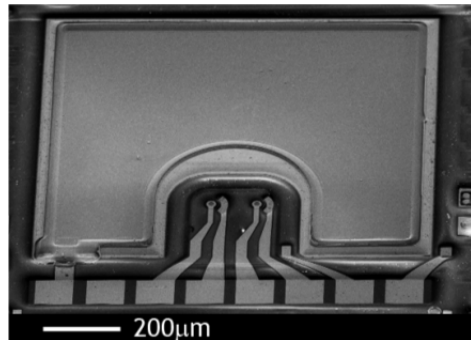


Figure 2-7: Scanning Electron Micrograph of a 670 nm monolithically integrated VCSEL/detector unit. A large area detector is chosen to collect ample signal.

While such results are extremely promising for several biomedical applications, and fluorescence is one of the most prevalent sensing mechanisms in use today, there are a number of issues that lead one to ask what we can detect without labels, or what other type of sensor modality could complement the fluorescence results. In particular, there are a limited number of engineered fluorescent probes in existence, and the engineering needed to create additional adequately specific probes is non-trivial. If one is able to obtain a sufficient fluorescent probe for a given desired analyte, the tagging and sample delivery process is the next step. Unfortunately, as currently performed, this process is

lengthy (often requiring hours), does not lend itself to widespread point-of-care use (as it requires trained personnel), and can easily account for a large majority of the cost of a test. Finally, provided an appropriate probe exists, after one spends the effort to deliver it, there remains a concern that the probe's presence itself alters the molecular interactions that one is in fact trying to measure. In contrast, optical label-free⁵ sensors, as described in the next section, offer a simplified sample preparation routine that can complement or replace lengthy and cost-prohibitive fluorescence techniques for various applications.

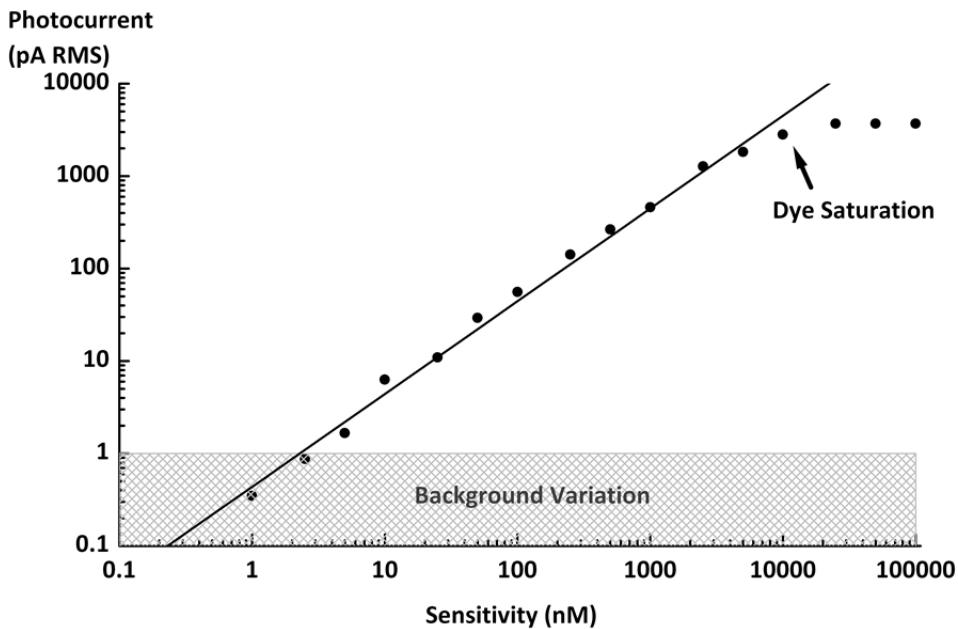


Figure 2-8: Photocurrent measured at the detector for various concentrations of Cy5.5 dye in PBS solution. As described by O'Sullivan et al. [37], the integrated VCSEL and detector was fixed below a transparent plastic well, with solutions introduced from low to high concentration and a buffer rinse in between consecutive concentrations to verify a return to the initial signal.

⁵ Label-free sensors employ any detection mechanism (which could be optical, electrical, or mechanical) that does not require labels or tags. Section 2.4 focuses on the growing field of optical label-free sensing that relies on the detection of a change in the index-of-refraction.

2.4 Label-Free Optical Sensing

To understand the principles of optical label-free or index-of-refraction sensing, one can imagine the displacement of a background fluid or gas with biological matter (for example, a red blood cell displaces buffer fluid when it binds to a recognition element, as shown in Figure 2-9). This displacement results in a change in the optical properties of the system, and can be detected by monitoring output signals such as a transmission spectrum. Utilizing a resonant structure like the photonic crystal slabs described in Chapter 3, one can generally achieve more sensitive detection of binding events - that is, one can more easily detect the shift of a sharp peak instead of the shift of a line or broader peak that would occur without the resonance enhancement.

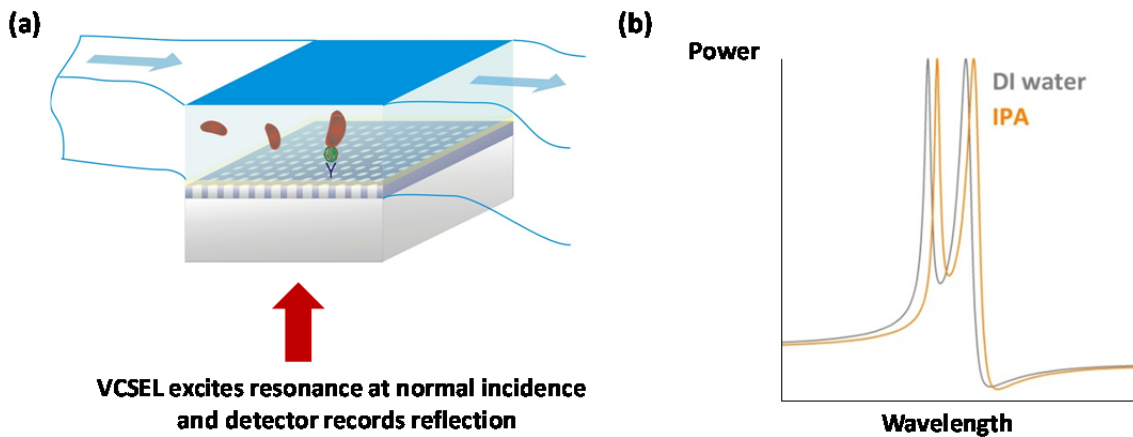


Figure 2-9: (a) Schematic of a photonic crystal guided resonance-based label-free sensor and (b) the simulated spectral shift for two different refractive index fluids. The displacement of background fluid upon the binding of an analyte to surface biorecognition elements alters the optical transmission spectrum of the device. Here, the simulated difference between bulk solutions of deionized (DI) water and isopropyl alcohol (IPA) illustrates the shift in the optical spectrum.

A number of different label-free optical sensors have been proposed and developed, with approaches ranging from ring resonators [43, 44], slot waveguides [45, 46], and interferometers [47, 48], to porous silicon [49, 50], ultra-high-Q whispering-gallery-mode resonators [51, 52], and photonic crystal cavities or fibers [49, 53-57]. Some of the key performance metrics and best achieved values in literature for these approaches are tabulated in Section 5.5 and compared with the work presented in this thesis. We will see that many of the device designs in this growing field are promising in their ability to confine light, often in extremely small volumes. However, a majority of the efforts in lab-on-a-chip research and technology development have thus far relied on external light sources (e.g., tabletop lasers or broadband white light) and required delicate alignment schemes that are not realistic for point-of-care handheld applications. Thus, the development of sensor designs that can circumvent these issues can accelerate the practical realization of truly portable, point-of-care diagnostic devices.

As reviewed by Hunt and Armani [11] as well as Fan and White [58], optical label-free sensors can be categorized into evanescent-field schemes⁶, resonant cavity approaches, and plasmonics approaches, with some designs drawing upon themes from multiple categories. Evanescent sensing was proposed in the 1960s based on total internal reflection and spectroscopy measurements [59, 60], and has been implemented in numerous device geometries and materials. As an extension of evanescent-based detection, resonant cavity-based sensing confines light of a discrete set of wavelengths, determined by the cavity dimensions. The attachment of molecules near the resonator changes the power spectrum of the device. Variations in evanescent and cavity-based

⁶ Evanescent field devices can include waveguide-based approaches as well as interferometric techniques.

sensor designs, including the range of materials used, the mode profiles, and the method of analyte delivery, yield a diverse set of prototypes for various target applications [28, 43-45, 47-57, 61-70].

Surface plasmon resonance (SPR) devices, where an electromagnetic wave propagates at a metal-dielectric interface, have been employed in angular, spectral, and localized detection configurations, and were the first index-of-refraction biosensors commercialized [71]. However, angular and spectral surface plasmon-based devices often require the incorporation of coupling prisms in addition to the ability to sweep incidence angle or wavelength. Moreover, even the structures that generate highly localized plasmon fields through nanoparticle or nanohole arrays instead of films [72-74] can suffer from metal absorption loss. In contrast, all-dielectric structures that are compatible with compact and easily coupled light sources such as VCSELs could provide improved efficiency at wavelengths where metallic structures are lossy, while significantly simplifying and reducing the cost of the overall system. Eliminating the reliance on large external lasers, LEDs, or broadband sources utilized for many biosensors, Figure 2-9 depicts our label-free sensor designed for integration with arrays of VCSELs.

In this type of index-of-refraction-based label-free sensing, it is useful to note that contrast agents or labels can be accommodated, but are only needed for applications where the intrinsic refractive index of the biological element to be detected is indistinguishable from the background solution for the desired limit-of-detection. Many proteins and other biochemical species of interest have refractive indices on the order of $n = 1.43\text{-}1.5$ [72]. Phosphate buffered saline (PBS), a common diluting agent, has a refractive index of ~ 1.332 , and extracellular fluid in a cell has a refractive index of $\sim 1.35\text{-}1.36$, both similar to that of water ($n = 1.333$ for the VIS-NIR wavelengths of interest).

Hence, depending on the background delivery solution, it may be possible to detect binding events *in situ* without labels; in cases where the analyte to be detected is too similar to the background solution, flushing with other aqueous solutions or allowing the sensing chamber to fill with low-refractive-index air or other gases after binding has occurred can improve the index contrast and detection sensitivity.

2.5 Introduction to Sensor Figures of Merit

Since we aim to demonstrate cost-effective and portable devices, the main challenge is to engineer the behavior of all the components of the miniaturized and integrated sensor system while maintaining adequate performance. In designing our label-free sensor, there are several important figures of merit or performance metrics to consider. In this section, we introduce some of the main hallmarks for device performance that will be discussed throughout the following chapters, including the detection sensitivity and limit-of-detection, signal-to-noise ratio, operating range, and temperature behavior. We also note the fundamental limits for different types of sensor designs, as recently reported by Yu and Fan [75].

As we will see in Chapter 4, a common definition for sensitivity with refractive index label-free sensors is the shift in wavelength for a given change in refractive index, expressed in nm/RIU. Since the spectrum shape can also change during a binding event, one must decide where to measure the shift (e.g., to measure the change in peak location, or to track the change at another position on the curve, such as the point of highest slope). In addition, depending on the design of the refractive index sensor, operating conditions (for instance, the specific sensor/analyte optical properties, or the spectral and spatial profile of the incident light) can alter the nm/RIU shift. Hence, for the most significant

comparisons, one should evaluate sensors that are targeting the same type of analyte and operating conditions. Nevertheless, the common nm/RIU metric can be used as a means for judging sensor performance. Some of the highest values of sensitivity are observed for SPR-based sensors, which can easily surpass 10^4 nm/RIU, compared to the $\sim 10^2\text{-}10^3$ nm/RIU calculated and shown for our all-dielectric devices in Chapters 3-5.

As discussed by Yu and Fan, for systems involving a single resonance mode, the spectral sensitivity has an upper bound of λ/n , where n is the refractive index of the medium [75]. While this implies that increasing the wavelength to the telecommunications band of 1.55 μm , for instance, where VCSELs are being developed [38, 76-78] would improve the sensitivity by a factor of ~ 2 compared to the 650-900 nm range, we again note that in our applications, the compatibility with integrated fluorimeters that can take advantage of FDA-approved molecular probes and emerging fluorescent proteins in the VIS-low NIR range is paramount.

Fortunately, nm/RIU sensitivity alone does not adequately measure the sensor performance; rather, the limit-of-detection, or smallest refractive index shift measurable, is often the more telling metric. For a collection of the detection limits reported in literature, we direct the reader to a review by Fan *et al.* [68] covering optical label-free techniques. We note here that the detection limit can be represented as the product of the sensitivity and the quality factor, Q [70]. Thus, although SPR systems boast a high sensitivity, their low Q (often on the order of $\sim 1\text{-}10$) means that dielectric resonators that have historically shown lower sensitivity, but can offer higher Qs, actually have comparable performance [70, 75].

Yu and Fan have recently noted that the extraordinary⁷ sensitivity of conventional SPR devices stems from the utilization of a continuum of modes, each with a different wavevector; this is not unique to SPR systems, and hence can be employed to design low-loss, high-Q dielectric sensors with extraordinary sensitivity [75]. In their study, an example waveguide suspended above a prism designed for 1550 nm wavelength light was shown to have calculated sensitivity of 28 000 nm/RIU, ~28 times larger than the 1000 nm/RIU calculated limit for sensing with a single optical mode for the same wavelength. Combining high nm/RIU sensitivity with the higher quality factors that are possible in dielectric systems compared with SPR systems promises to yield a better ultimate limit-of-detection for dielectric resonators.

In addition to the resonator component, one must also consider the other sensor elements and their effect on the device performance. In amplitude-sensing optical systems where we collect intensity as a function of wavelength, our fundamental limit-of-detection is set from noise in the system. The uncertainty or noise in the x -axis (wavelength) combined with the uncertainty in the y -axis (intensity, or number of photons) dictate this limit. For wavelength precision, we rely on a VCSEL's response to temperature to reproducibly tune the lasing wavelength. As we will see in Section 4.1.4, VCSEL temperature tuning results in a reproducible shift of 0.06 nm/°C; by controlling the temperature reliably in steps of 0.5 °C, this provides an incremental wavelength control of ~0.03 nm for VCSELs at 670 nm. This is smaller than the minimum linewidth that can be measured by many optical spectrometers, providing excellent wavelength resolution without the need for cumbersome equipment.

⁷ Extraordinary is defined in Yu and Fan [75] as having sensitivity, normalized to the λ/n single-mode limit, greater than unity.

For intensity precision, both the VCSEL and detector performance should be considered. One must achieve as stable of an excitation intensity as possible in order to maximize the detection of small changes in transmission and reflection spectra. In VCSELs, intensity stability is characterized by the relative intensity noise (RIN), which is defined as

$$\frac{\langle \Delta P^2 \rangle}{P_{avg}^2} \quad (2-4)$$

where ΔP^2 is the mean-square of the assumed Gaussian noise distribution and P_{avg} is the average output power [79]. It is known that VCSELs offer very stable sources over both low and high frequencies, with RIN measured to be much better than -120 dB/Hz in 675 nm VCSELs at frequencies down to 10 Hz [80]. In this work, we quantify the intensity noise from measurements lasting up to a few hours, for various VCSEL and TEC biasing configurations, in Chapter 4. Along with RIN, both shot noise, from photon arrival and dark current, as well as thermal (Johnson-Nyquist) noise, contribute to the limit of intensity precision. These factors, as well as some techniques to mitigate noise to achieve 5.0 pA/mm² dark current in our detectors, are discussed in more detail by O'Sullivan et al. [37] and in Chapter 4.

In addition to a sensor's limit-of-detection and the related noise performance, the system's operating range is a useful metric. It is common for PIN photodiodes to have over nine orders of magnitude linear dynamic range [31], which is generally adequate for biological sensing. A more pressing issue in the sensor's operating range is the ability of the sensor to be insensitive or adaptable to temperature swings in the environment; indeed, in fields such as silicon photonics, performance degradation with ambient temperature variations is well known and the subject of much effort [81-84]. Fortunately, the thermal behavior of all-dielectric photonic crystal devices like those created in this

work offers better stability than temperature-sensitive Si-based counterparts due to intrinsic differences in the materials' thermal coefficients. Chapter 4 will examine the effect of temperature on our VCSEL wavelength, power, settling time during bias changes, and stability for a wide operating range.

Finally, the sensor robustness or reliability is a significant design criterion and figure of merit. While a device in the laboratory could be extremely sensitive and have a high dynamic range, if the operation is not robust to variables in point-of-care environments, achieving portability will be a struggle. Hence, it is often advantageous to trade some sensitivity for a larger operating range, tunability, and ease of use in the field. The performance of the individual components of our sensor and the ensemble sensitivity are discussed in further detail in Chapters 4 and 5, with a focus on tunable components to accommodate environmental changes. We will see that a key device design challenge to achieve our desired performance metrics is how to enhance the interaction of light and the analytes in an area that is easily accessible to the biomolecules of interest. Thus, the next sections will introduce useful techniques for engineering photonic materials that can amplify the interaction between light and matter.

2.6 Summary

The development of rapid and integrated sensing technologies for lab-on-a-chip systems has the potential to change the landscape of global health monitoring and enable new diagnostic capabilities. Optical methods, and label-free techniques in particular, are attractive because they lend themselves well to integration with other mechanisms, and can be compact, lightweight, and non-destructive. VCSELs can address the size, cost, and complexity drawbacks of many sensor designs, enabling real-time multi-modality analysis

with integrated arrays. Prior work in our research group focused on VCSEL-based fluorescence sensors at the challenging operating wavelength of 670 nm to take advantage of newly emerging deep-red fluorescent proteins and fluorescent dyes such as Cy5.5 which are FDA-approved and already in pre-clinical use. However, the complexity and costs attached to fluorescence sensing currently limit its usefulness for many point-of-care applications, especially in resource-limited environments. Designing label-free sensors that offer simplified sample preparation to complement or even replace fluorescence techniques is thus the focus of this work. In order to demonstrate label-free analyte detection that can be implemented side-by-side with widely used fluorescence techniques, we choose to design our sensors to operate at 670 nm. Moreover, we develop sensing schemes that feature shared sample delivery, light source control, and detection to enable parallel, multi-modality measurements.

Important figures of merit to consider in the design and characterization of the system include the sensor's limit-of-detection, signal-to-noise ratio, operating range, and temperature behavior. To achieve a reasonable limit-of-detection, while providing tunable sensors that are substantially smaller and less costly than many of today's options, one can take advantage of intensity enhancements arising from resonances. As the next chapter, "Photonic Crystal Slabs for Label-free Sensing," will describe, utilizing guided resonances in photonic crystal slabs can enhance the interaction of light and matter for efficient label-free biochemical detection. The photonic crystals employed have a number of properties that make them particularly well-suited for low-cost lab-on-a-chip systems.

Chapter 3

Photonic Crystal Slabs for Label-Free Sensing

“If we wish to make a new world, we have the material ready.”

- Robert Quillen

Many of the technological advances in human history have stemmed from our understanding of materials and our ability to engineer unique and desirable material properties for a number of applications. From our prehistoric ancestors who constructed tools from durable stone and iron, to early semiconductor device engineers who learned to precisely control a material's conductivity, our ability to design and fabricate useful structures relies on a growing collection of natural and man-made materials. In the last century, we have seen how tailoring a semiconductor's electrical properties enabled the invention and first demonstration of the transistor, which in turn brought about an information technology revolution that continues to transform our society's computation, data storage, and communication capabilities. In the last few decades, a new frontier of research has emerged, centered on the control and characterization of a material's *optical* properties.

The discovery of a new kind of artificial material, coined a “photonic crystal” by John and Yablonovitch in the late 1980s, has created a new paradigm for optical device design and fabrication [85-87]. Photonic crystals are periodic arrangements of materials that have different dielectric constants or indices of refraction. Just as the atoms in an electronic material’s lattice present a periodic potential to an electron, and determine if and how electrons propagate, the repeating elements or “artificial atoms” of a photonic crystal can regulate photon propagation. Photonic crystals can mold the flow of photons at length scales smaller than the wavelength of incident light, pinning energy to an optical cavity, directing it along a waveguide, or confining it to a surface.

Photonic crystals can be designed with periodicity in one, two, and three dimensions. A simple example of a 1D photonic crystal is a distributed Bragg reflector (DBR), such as those used to form the mirrors of VCSELs. 2D photonic crystals are frequently used to confine light in waveguides and cavities, and can be found in commercial products such as photonic crystal fibers. While 3D periodicity provides the ultimate control by confining light in all three dimensions, the fabrication of such structures remains a significant roadblock to practical devices. A much more easily fabricated structure that is particularly well-suited for confining light to a surface for efficient overlap of intensity and biochemical samples is a 2D photonic crystal slab. As shown in Figure 3-1, a photonic crystal slab is defined by a material that is patterned to yield a periodic array of posts or holes. In this example, the contrast between the slab and the surrounding air and substrate confines the light in the z direction, and the periodicity from the patterning confines the photons in the x and y directions.

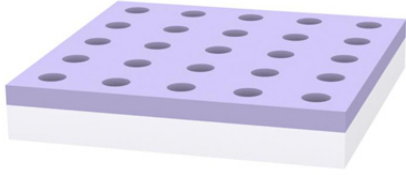


Figure 3-1: A 2D photonic crystal slab, with a square lattice of air holes.

As we shall see in this chapter, these photonic crystal slabs provide guided resonance modes that are well-suited for compact and efficient optical devices. In the following sections, we introduce the physical origins of guided resonances (Section 3.1), highlight some of their useful properties (Section 3.2), and show the design and theoretical calculations for operation in the desirable VIS-NIR absorption transparency window (Section 3.3).

3.1 Introduction to Guided Resonances

The guided resonances that we employ in our sensor designs originate from the guided modes in uniform slabs of material. In order to provide a better understanding of the physical mechanisms that produce the resonances, one can simplify our 2D slab to a 1D system where the periodicity is in only one of the lateral directions, as discussed by Suh *et al.* and Joannopoulos *et al.* [88, 89]. In this 1D structure, there are two types of modes, shown in Figure 3-2. The radiation modes form a continuum, shown in green, above the light line. Such modes are lossy and propagate in the space surrounding the slab. The other modes, shown below the light line, are guided modes that are completely confined within the slab of material and do not radiate outward. In this scenario, there is no overlap between these two types of modes, as external radiation cannot excite the guided mode and vice versa.

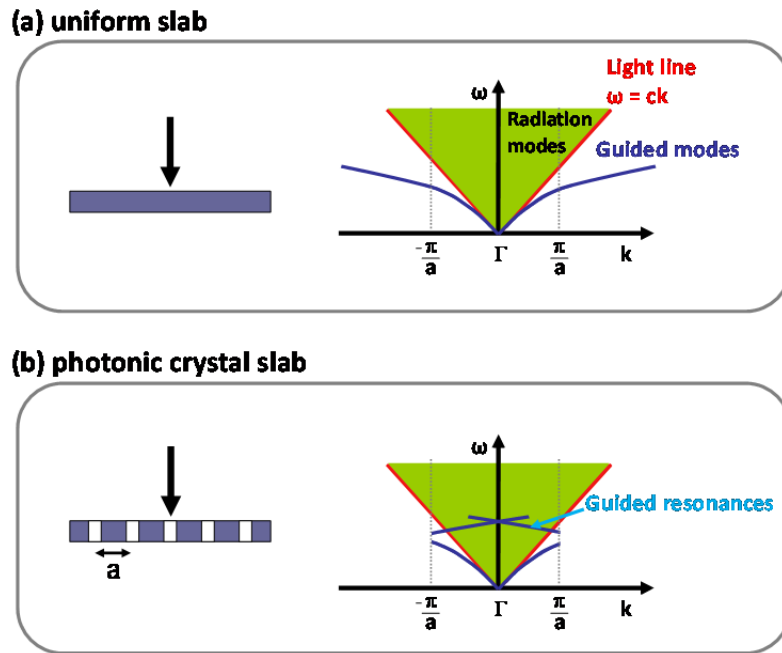


Figure 3-2: (a) A uniform slab (side view) and its frequency vs. wavevector diagram showing separate radiation and guided modes. (b) The addition of scattering elements, with periodicity a , in a photonic crystal slab causes the guided mode to fold, creating guided resonances that can couple to external radiation. Figure adapted from [90].

However, if one introduces periodic index contrast (for example, by patterning and etching holes), the new scattering elements will enable phase matching such that some of the guided modes can couple to the continuum of radiation modes. A photonic band gap where photons cannot propagate is created, as the dispersion relation of the guided mode folds at the Brillouin zone boundaries. The modes that have been folded to overlap with the radiation continuum now possess a finite lifetime and have become the guided resonances that we will make use of in our sensor.

While the photonic bandgap that has opened at the Brillouin zone boundaries is useful in designing omni-directional reflectors and devices where light is coupled laterally, in order to efficiently integrate the VCSELs previously mentioned, we concentrate on the

gamma point where the in-plane wave vector is zero. As we shall see in the next sections, this operating regime allows for easy coupling, and the guided resonances near this point offer interesting transmission and reflection features useful for biosensing applications.

3.2 Properties of Guided Resonances

When extending the photonic crystals described above to the case of a 2D slab, the spatial distribution of electric field power density often results in a majority of the power being trapped inside the photonic crystal slab and decaying away from the surface. Although the guided resonances are strongly confined within the slab, the ability to couple to the radiation continuum enables one to probe the volume adjacent to the slab surface easily with normally-incident light. The unique ability to excite and sense guided resonances with normally-incident light makes such photonic crystals particularly well-suited for use with arrays in a 3D configuration, as depicted earlier in Figure 2-2. This is extremely useful for portable biochemical sensors, as the elimination of waveguides and couplers brings down cost as well as assembly and testing complexity.

In addition to this beneficial normal-incidence coupling, a 2D photonic crystal slab's design flexibility enables one to create guided resonances for a number of applications. The guided resonance frequency and lifetime are determined by the photonic crystal's material properties and geometry, providing many options for engineering optical transmission functions. For example, as shown in Figure 3-3, one can design the photonic crystal slabs to have the majority of the surface intensity outside of the holes, making the resonance robust to etching non-uniformities or sidewall roughness, while simultaneously improving the overlap of the intensity with the areas where biorecognition elements would capture the analytes (Figure 3-3).

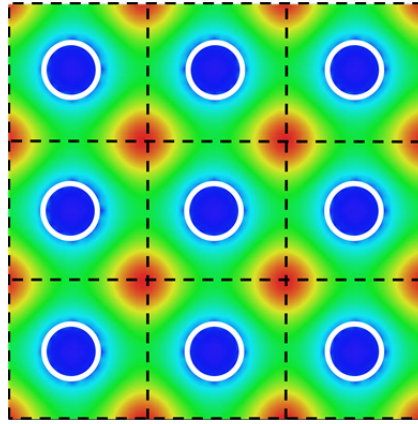


Figure 3-3: Energy profile (3x3 unit cells shown) on the photonic crystal surface. Intensity hot spots (red) are located outside of the holes (white outline), providing increased field intensity where biorecognition elements would capture analytes and also making the structure robust to sidewall and etching non-uniformities.

3.3 Design and Simulation for VIS-NIR

In order to design and simulate photonic crystals that produce resonances in our wavelengths of interest, we employed finite difference time domain (FDTD) methods as well as two implementations of rigorous coupled wave analysis (RCWA): a momentum-space version of the transfer-matrix method [91, 92] and S^4 , a Fourier Modal Method (FMM) platform written by Victor Liu of Professor Shanhui Fan's group at Stanford [93]. The recently developed S^4 is the preferred implementation, as it provides near-exact⁸ results for structures like the photonic crystal slabs discussed in this work, and converges faster than FDTD. The designs described in this section are suited for the desirable VIS-NIR transparency window of 650-900 nm, where one can benefit from the low absorption of water, lipids, hemoglobin, and oxyhemoglobin that would otherwise reduce the signal

⁸ If the dielectric profile could be exactly Fourier expanded into the reciprocal lattice vectors used in the simulation, then the results of the simulation are in fact exact. Convergence issues stem from the truncation of the Fourier series of the dielectric profile, not from an inherent discretization.

contrast of target biological samples. Specifically, we concentrate on resonances near 670 nm, 795 nm, 820 nm, and 850 nm to match existing VCSELs.

Table 3-1 shows some typical geometric parameters that correspond to resonances at these VIS-NIR wavelengths. The parameters were swept to find combinations that would provide a high quality resonance for ample sensitivity, while allowing ease of fabrication. In addition, as we will describe further in Chapters 4 and 5, one of the primary requirements for the implementation of VCSEL-based refractive index sensing without the use of bulky spectrometers is the ability to create a photonic crystal guided mode resonance with an appropriate Q. We will see that the FWHM of the resonance in fact needs to be at least a few times larger than the FWHM of the VCSEL. These considerations translated into reasonable ~1:1 aspect ratios, a thick enough photonic crystal layer to yield a uniform optical film, and a “fill factor” (i.e., hole area to slab surface ratio) large enough to allow for effective surface treatment and adequate binding area. Silicon nitride (SiNx) and fused silica were chosen for the photonic crystal layer and substrate, respectively, to ensure low-loss structures where fabrication could be optimized to provide high quality patterning, and to provide glass-like surfaces that are amenable to standard biochemistry surface treatments.

	Parameters for VIS-NIR Resonances
Periodicity	400-500 nm
Slab Thickness	150-300 nm
Hole Diameter	100-300 nm
Dielectric Constants	substrate: 2.132 (fused silica) slab: 4 (SiNx)

Table 3-1: Typical geometric and materials parameters used to generate guided resonance modes in the VIS-NIR.

As illustrated in Figure 3-4, changing geometrical parameters such as the periodicity, hole diameter, slab thickness, and etch depth provides control of the resonance shape and frequency. We take advantage of the doubly degenerate guided resonance modes and the two resulting peaks, with four slopes available to coincide with a probing VCSEL source. As we will see further in Chapters 4 and 5, the proof-of-concept device requires the photonic crystal guided resonances in aqueous solutions to coincide with the limited wavelength tuning range of VCSELs.

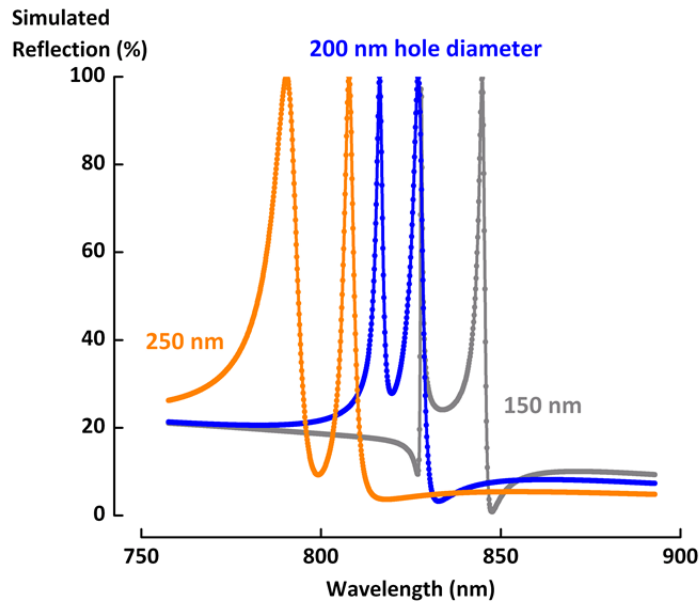


Figure 3-4: Effect of hole diameter on the photonic crystal guided resonance peak location and shape. Simulation results for SiNx on fused silica in air, with hole diameters of 250 nm (orange), 200 nm (blue), and 150 nm (grey) are shown.

To estimate our sensor's ability to detect refractive index shifts, simulations with different bulk index materials were studied. Figure 3-5 shows simulated reflection spectra for a 250 nm thick SiNx photonic crystal on fused silica with 500 nm hole pitch, 200 nm diameter, and 300 nm over-etch. Each curve represents a different solution of deionized (DI) water and isopropyl alcohol (IPA) filling the volume above the photonic crystal, including the holes. One can see a large variation in transmission, from near zero to

100%, over a narrow wavelength range. Plotting the simulated peak as a function of the refractive index of the medium that lies above the slab yields a fitted slope of 130 nm/RIU sensitivity (Figure 3-5b), comparable to other refractive index sensors [70], but with advantages in size, scalability, and cost when integrated with VCSEL and detector arrays.

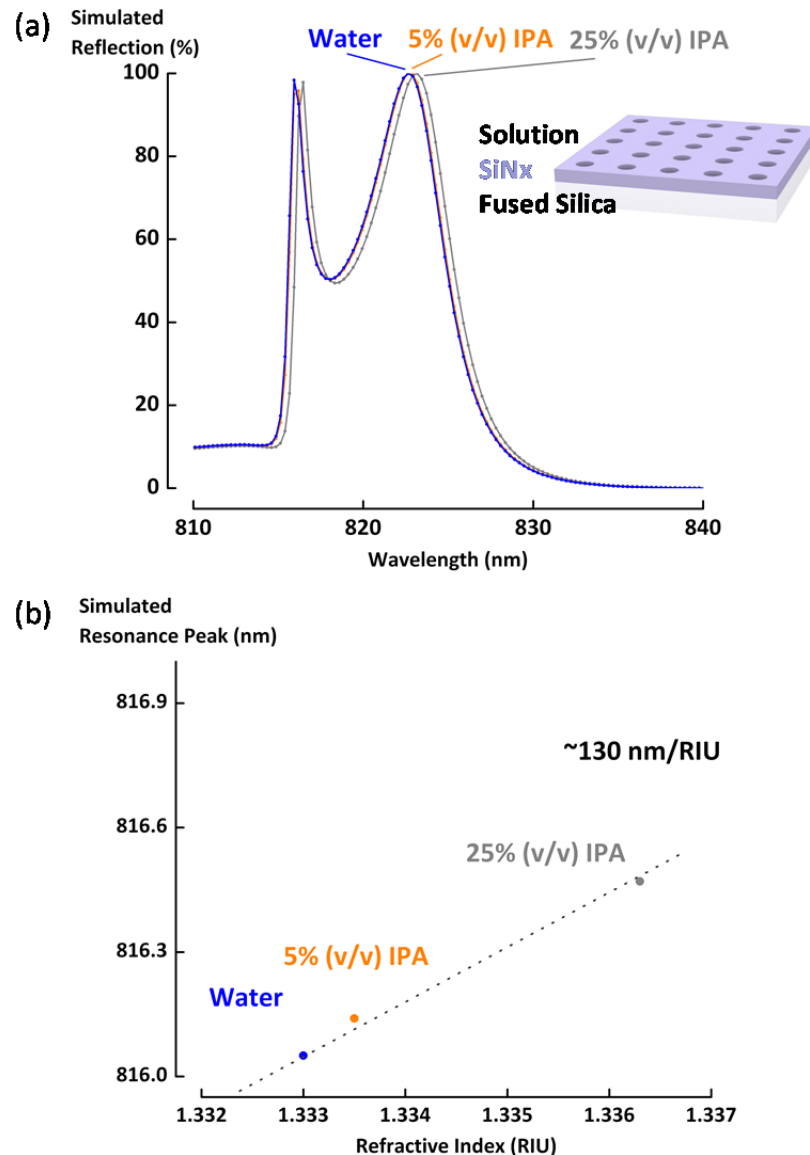


Figure 3-5: (a) FDTD simulation of reflection spectra for mixtures of IPA and water. (b) Simulated sensitivity of 130 nm/ RIU.

Similarly, for photonic crystal designs at 670 nm, with \sim 145 nm hole diameter, 400 nm pitch, 250 nm thickness, and 300 nm etch depth, we see two guided resonance modes (Figure 3-6a). When comparing the simulated reflection spectra of three different fluids (Figure 3-6b), we see an expected shift of \sim 130 nm/ RIU.

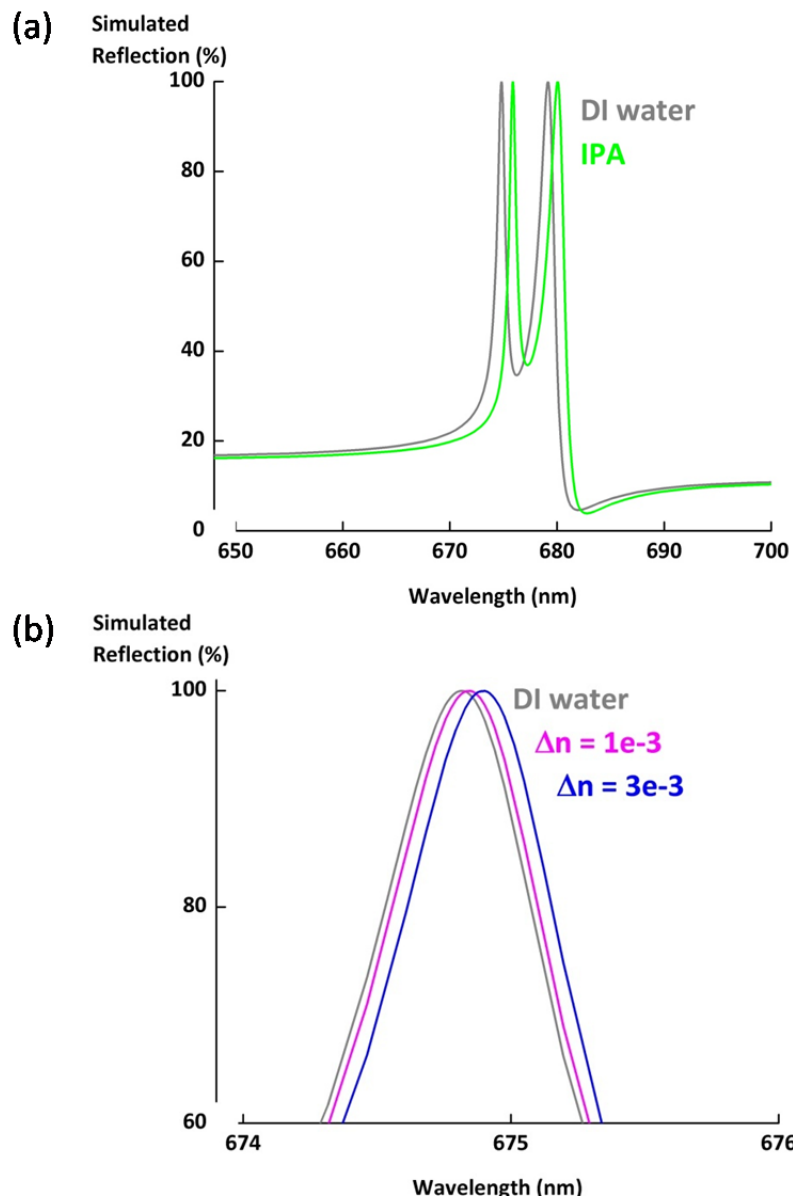


Figure 3-6: (a) Simulated reflection spectra for water and IPA above a photonic crystal slab designed for operation at \sim 675 nm and (b) Simulated peak shift for solutions of different refractive indices (1.333, 1.334, and 1.336).

In both the ~800 nm and ~670 nm designs shown, there are two doubly-degenerate TM-like and TE-like guided resonance modes that provide flexibility in testing and can be used to characterize the fabrication processes. The lower-wavelength TM-like mode, where the out-of-plane electric field extends further into the analyte [94], as well as the TE-like mode where the field is concentrated at the photonic crystal surface, can be utilized. To access a specific resonance, one can control VCSEL polarization through various techniques [95, 96]. If the photonic crystal sample is perfectly symmetric in x and y , however, the transmission response for normally incident light (regardless of polarization) will include both peaks, with a higher Q expected for the lower-wavelength TM-like mode. If there is any ellipticity in the photonic crystal hole shape, or if the beam probing the photonic crystal arrives at off-normal incidence, symmetry is broken. Consequently, one of the peaks can be more visible experimentally, and controlling the polarization of probing beam can improve the as-measured detection sensitivity.

Figure 3-7 compares the spectra observed when an external polarizer is rotated to modulate an aligned, broadband un-polarized light source. One can see that for the 0° and 90° polarizations, only the TE-like or TM-like modes appear, respectively. For 45° (approximately equal amounts of TE- and TM-polarized incoming light), both peaks appear, but the sharp transitions in the middle are blended. The as-fabricated sample yielded a higher quality TE-like resonance in this case. Observing each resonance in this manner also helped determine which samples had the most circular holes. Nevertheless, even if the photonic crystal holes were perfectly circular and the probing beam were perfectly-aligned, in practice there is a finite cone of incidence angles. Hence, the study of how polarization and the incoming angle of incidence affect the transmission behavior can provide valuable insight for experiments.

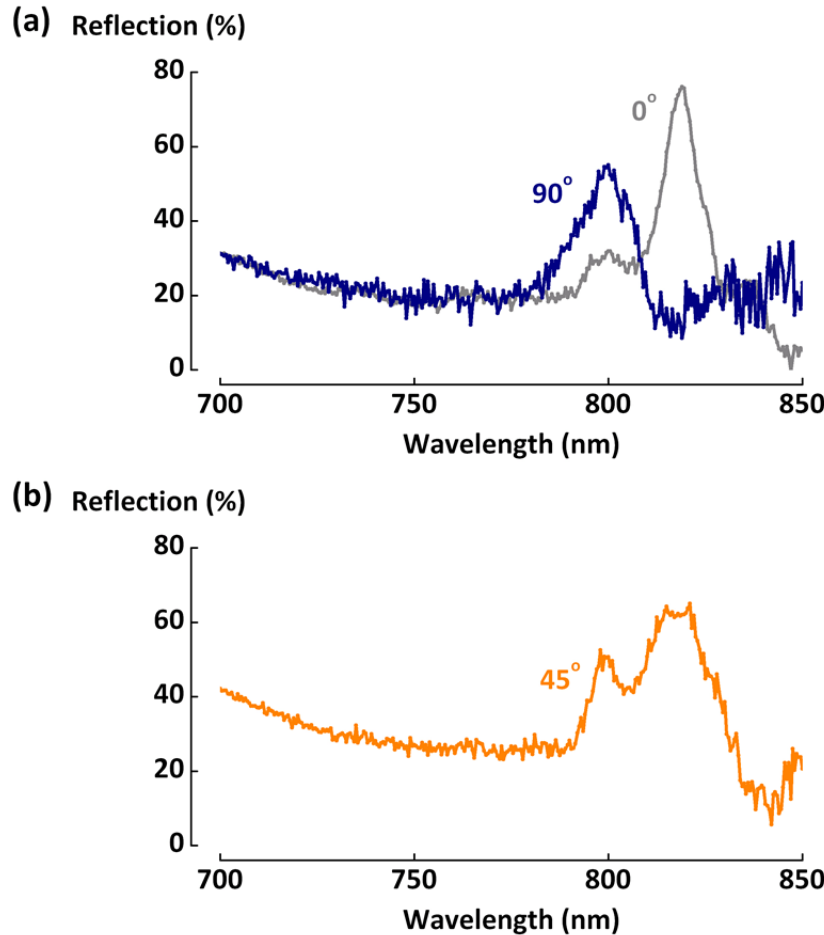


Figure 3-7: Photonic crystal spectra observed when a polarizer is rotated (a) 0° and 90° or (b) 45° show the quality of each resonance.

As shown in Figure 3-8, simulations indicate that an incidence angle of 2° can substantially change the resonance peak. However, the slope is somewhat preserved, allowing sensing with moderate enhancement in cases where more lenient alignment and packaging are needed. Even though a VCSEL's divergence is low, the angle of incidence on the photonic crystal slab must be considered during system design and packaging to preserve the guided resonance transmission function and optimize sensitivity. Thus, we will revisit the angular dependent behavior of the photonic crystal more closely when studying the interaction of VCSELs with the photonic crystals in Chapter 5.

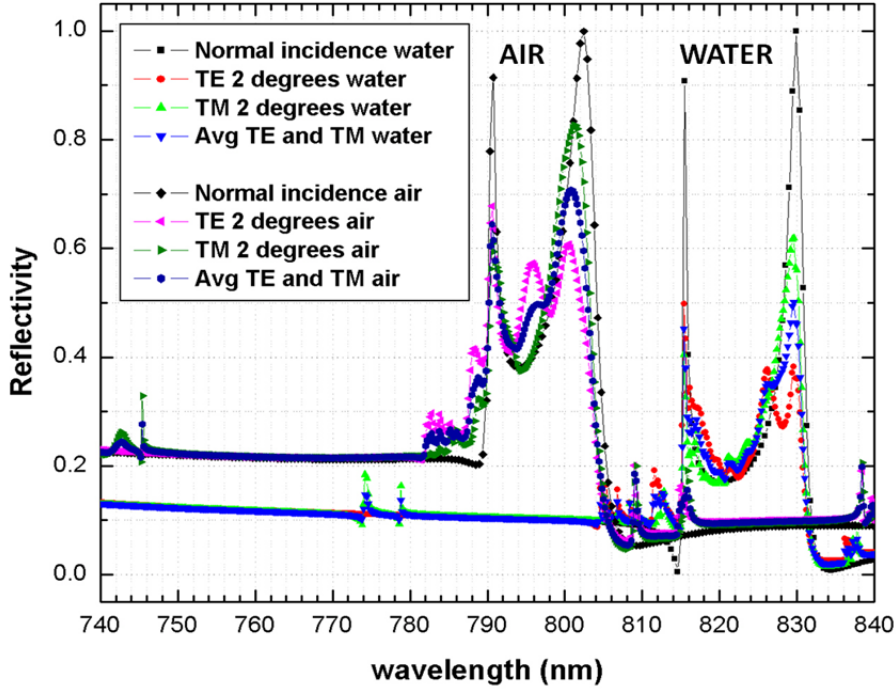


Figure 3-8: Simulation results for TE and TM off-normal incidence show a substantial change in peak to valley height, but a preserved slope when averaging behavior from a cone of up to 2°.

Finally, while we rely on the scattering matrix method and design for the VIS-NIR for the devices in this thesis, there are two items worth mentioning for future studies. Although the scattering matrix method for many simulations takes only minutes to converge, which is many times faster than typical FDTD methods for comparable structures and resolution, alternatives under development such as inverse design [97, 98] are attractive for the possibility of specifying a desired property (for instance, a high energy enhancement at the surface) and allowing optimization algorithms to determine a structure that will produce the specified behavior. Secondly, it is worth mentioning that due to the scale invariance of Maxwell's equations, the geometric parameters of these photonic crystal designs can be scaled, to enable operation at different wavelengths while

maintaining similar aspect ratios and fabrication processes [89]. Moreover, with lithographically defined photonic crystal areas, one can easily create different sections of photonic crystals with resonances at different wavelengths, all on one substrate. Such a scheme would allow for useful calibrations or referencing, as well as an extended operating range.

3.4 Summary

Recent advances in photonics design and nanofabrication make it possible to confine energy at sub-wavelength scales for enhanced interaction between light and matter. In particular, 2D photonic crystal slabs can be designed to have guided resonances that feature a very sharp variation in transmission coefficients over a narrow wavelength range, enabling sensitive detection of refractive index shifts near the slab. These resonances can be excited and sensed with normally incident light, making them uniquely well-suited for use in compact sensor arrays.

We design photonic crystal guided resonance sensors in the VIS-NIR wavelength range to take advantage of the transparency window for biological carrier fluids and enable parallel multi-modality sensing with existing VCSEL-based fluorimeters. The photonic crystal periodicity was chosen to be on the order of 400-500 nm, with \sim 100-200nm diameter holes, to create VIS-NIR resonances that would be appropriate for use with VCSELs. Such moderate-Q structures provide sensitivities of \sim 130 nm/RIU and can be fabricated with reasonable precision in university research laboratories.

This simulated sensitivity and the resulting limit-of-detection that we will measure in subsequent chapters are comparable to values achieved from other sensors, but less than the highest reported performance in literature. Moreover, simulations and initial

characterization of fabricated slabs indicate that an incidence angle of a few degrees can substantially change the resonance peak, meaning that careful design of the detection system and packaging is needed to optimize sensitivity. Despite these challenges, the integrated VCSEL and photonic crystal slab device platform provides a distinct advantage in sensor size, cost, coupling ease, and tunability for point-of-care applications. We will see that one can integrate the photonic crystal sensing surface with a light source and photodetector in a compact module for use in arrays with shared microfluidics and electronics. The following chapter describes the fabrication and assembly processes used to build such a prototype label-free sensor, the extensive characterization of each component to enable effective system integration for label-free sensing applications, and the initial broadband measurement of the key photonic crystal slab element.

Chapter 4

Sensor Fabrication and Characterization

“What I cannot create, I do not understand.”

- Richard Feynman

To produce a proof-of-concept label-free biosensor, several miniature components were fabricated, tested, and often redesigned or optimized in order for the system to function as an ensemble. This chapter describes the design challenges and rationale behind the fabrication and packaging techniques employed, and presents measurement results for each sensor element. Section 4.1 examines the VIS-NIR TEC/VCSEL/detector module that enables temperature and current tuning of the lasing wavelength. Since our label-free sensor aims to evade traditionally bulky and expensive broadband sources and spectrometers, the VCSEL tunability and intensity stability are crucial. Hence, we investigate the VCSEL behavior as a function of temperature and biasing conditions, reporting the power, spectrum, mode profile, noise, transients, and divergence.

Section 4.2 then describes the VIS-NIR photonic crystal slabs, surface treatment options, and fluidic delivery system to facilitate bulk refractive index sensing in aqueous solutions. The photonic crystal resonance is characterized in air, water and isopropyl alcohol (IPA) mixtures (Section 4.3), in preparation for use with VCSELs and detectors.

4.1 Integrated TEC, VCSEL, and Detector Module

As we introduced in Section 2.3, prior work on monolithically integrated VCSELs and detectors on GaAs [21, 30, 33, 34, 37, 42, 99] enables cost-effective and efficient fabrication, testing, and packaging. While the VCSEL and detector modules our group has previously designed for fluorescence sensing usually featured transverse multi-mode laser operation for high power [37], for label-free refractive index sensing with photonic crystals, this work targets single-mode operation to achieve a narrow linewidth and improve the resolution of transmission spectra.

Measuring transmission spectra with a narrow linewidth light source and point detectors instead of a broadband light source and bulky spectrometers requires the ability to tune the source emission wavelength. A VCSEL’s lasing wavelength can be altered by changing the current that is biasing the laser, the temperature of the laser, or the laser cavity. Although the use of micro-electro-mechanical systems (MEMS) for tuning the length of the cavity can provide a large lasing wavelength range and has been successfully demonstrated for a wide spectrum of applications, the fabrication is often complex and more costly than VCSELs that have no moving parts [100-105]. Thus, in this work, we focus on temperature and current tuning that allows us to alter the wavelength of as-fabricated lasers, by utilizing Peltier or thermoelectric coolers (TECs) that can be characterized with standard techniques.

4.1.1 Design and Fabrication

TECs are commercially available, with thousands of variations in size and performance, and serve as compact solutions for cooling, heating, and stabilizing telecommunications lasers, detectors, and a number of different electronic components.

A typical TEC element schematic is shown in Figure 4-1. The TEC consists of two dissimilar materials, illustrated in green and blue, placed in series electrically and in parallel thermally, with top and bottom contact plates. The dissimilar materials are often P and N doped semiconductors, as indicated in the figure. From the Peltier effect,⁹ one can heat or cool the top plate, depending on the direction of electrical current flow between the sandwiched, dissimilar materials.

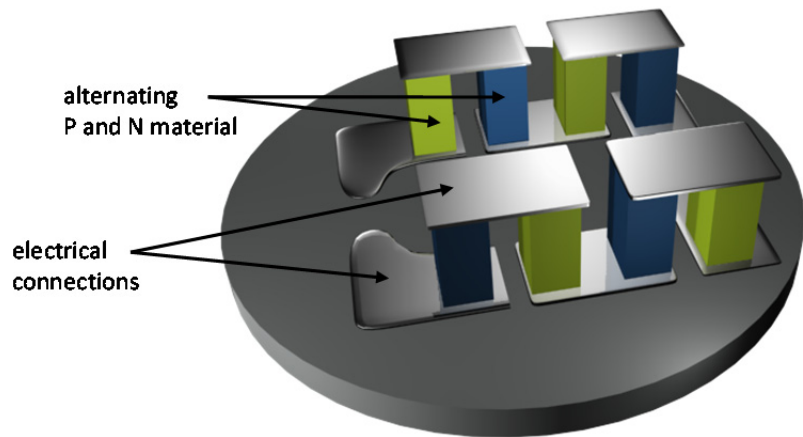


Figure 4-1: Schematic of a TEC, with the top ceramic plate removed to more easily observe the four P and N (denoted in green and blue) pellet pairs linked in series electrically and in parallel thermally.

The TECs used in our module consisted of P and N-type semiconductor pellets, with ceramic top and bottom plates and metal bonding pads. Since several TECs available were able to generate temperatures well beyond the range needed for VCSEL tuning, all with comparable efficiencies, the TECs used to control the temperature of the VCSEL were chosen primarily for their size and ease of integration with transistor-style

⁹ The Peltier effect was discovered by French watchmaker and part-time physicist Jean Charles Athanase Peltier in 1834.

packaging. The TEC top plate was chosen to allow placement of the integrated VCSEL/detector and any additional lasers bonded with thermal epoxy next to a thermocouple used for real-time read out and recording of the temperature at the device ground plane.

After initially using TECs with ceramic plates that needed to be trimmed to fit into a TO-5 style transistor package, later designs employed a newer 2.5 mm x 3.2 mm unit, only 1.4 mm high, as shown in Figure 4-2. The smaller size TEC maintained performance by utilizing eight P and N pellet pairs instead of four. The range of allowable currents for the TEC units (up to 1-2 Amperes, for the components used), the maximum allowable voltage (~0.5-1 V), and the maximum change in temperature possible between plates (~70° C), were all more than adequate for our desired VCSEL temperature tuning range. As we will see in Chapter 5, for tuning the VCSEL ~3 nm, TEC biases of approximately 300 mA can be used to sweep the temperature from ~8 °C to 50 °C.

Especially since the first type of TECs required diamond-sawing to trim the ceramic plates to a size that would fit on the TO-5 header (inner diameter 4.84 mm), resistance measurements were taken to verify TEC behavior before and after bonding with a temporary thermocouple, raising the integrated device yield. This ensured that the VCSELs and detectors that would be difficult to remove and reuse after bonding would only be paired with functional TECs. The largest component to be mounted on each TEC was the integrated VCSEL and detector, with most of the area needed for a large (~0.75 mm²) detector to provide ample opportunity to collect intensity reflected back from the photonic crystal.

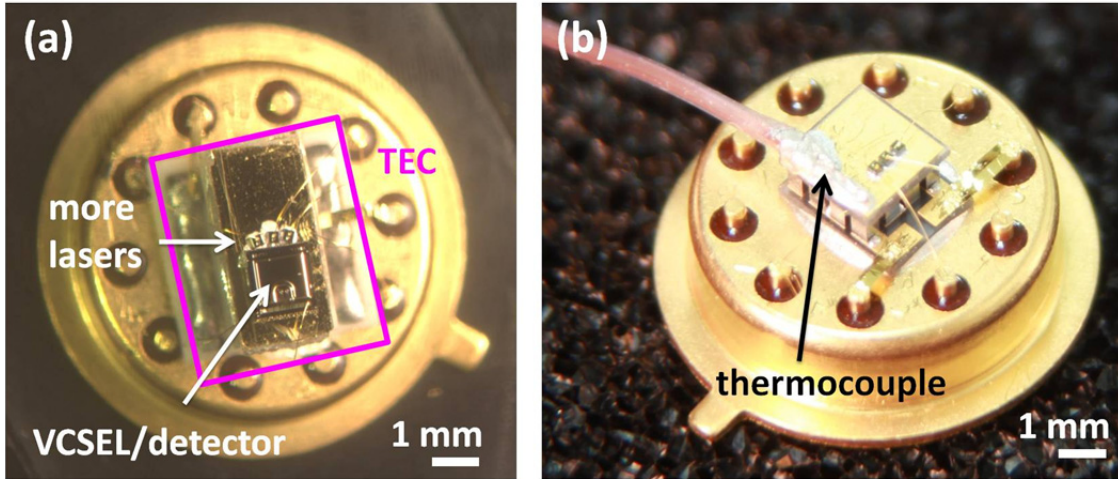


Figure 4-2: Photographs of two types of TECs used to control the VCSEL temperature. (a) A 4-pellet pair unit that needed to be trimmed to fit standard transistor packaging, with the monolithically integrated VCSEL/detector as well as three extra lasers at a different wavelength. (b) An 8-pellet pair TEC device with a slimmer profile. Three lasers are bonded, and a precision thermocouple is attached with conductive epoxy. The next step is the bonding of the monolithically integrated VCSEL/detector in the remaining space on the top metallized plate.

For our VIS-NIR wavelengths of interest, the AlGaAs/GaAs system is utilized to epitaxially grow the integrated VCSEL and detector. This material system features ideal lattice-matching, enabling high quality crystalline material growth, as well as a large contrast in refractive indices, yielding high reflectivity DBR mirrors.

Figure 4-3 depicts a typical VCSEL, with an oxide aperture and a PIN diode structure where carriers are injected and recombine in the intrinsic region. DBRs are used to provide high contrast VCSEL cavity mirrors. Optical gain is provided by multiple quantum wells in the center of the optical cavity that is formed by the top and bottom AlGaAs/GaAs DBRs. The composition of the quantum wells and barriers in the active region can be tuned for the target laser wavelength.

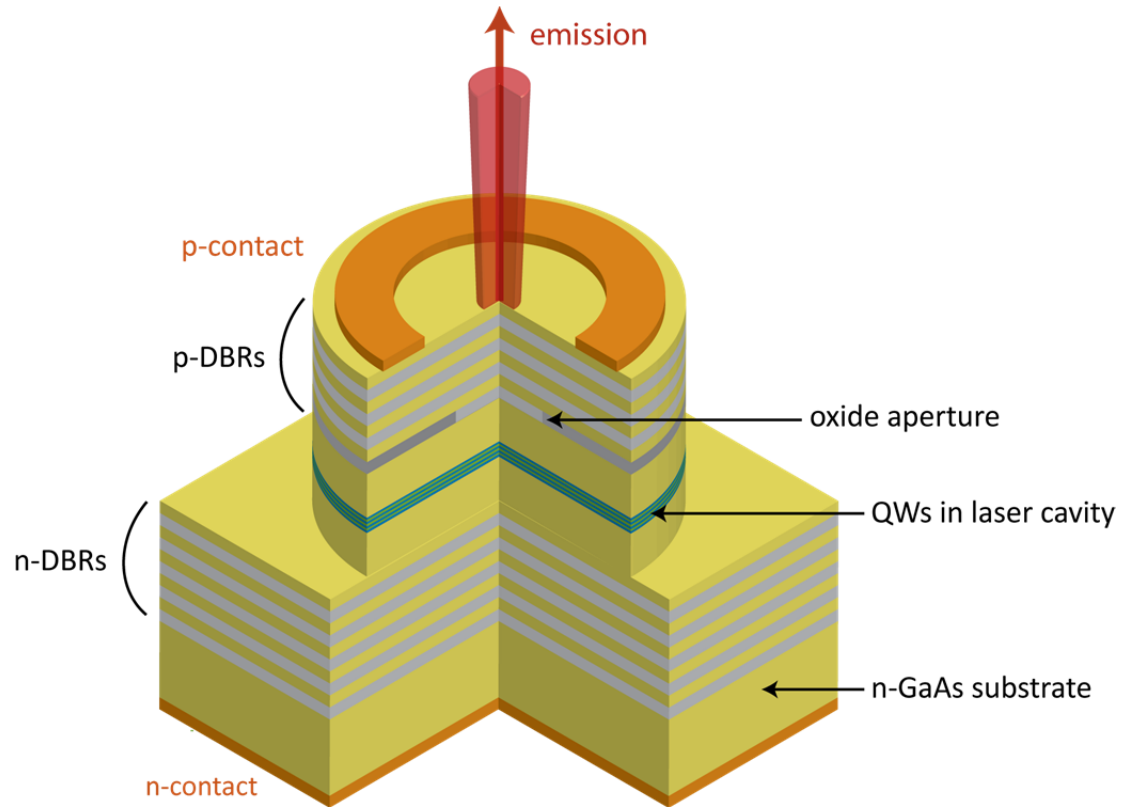


Figure 4-3: A typical VCSEL structure, with bottom n-contact, GaAs substrate, top and bottom DBRs defining a cavity, quantum wells inside the cavity, and a top ring contact. An oxide aperture confines the current and emission occurs normal to the substrate.

When fabricating an integrated VCSEL and detector structure, one may design the laser on top of the detector, or vice-versa. The design choice to locate the relatively thick¹⁰ (approximately 2 μm) detector absorption region above or below the VCSEL is significant, as it can greatly influence the overall device performance in addition to the

¹⁰ The thickness was chosen for high detector responsivity, absorbing over 95% of incident radiation for the emission spectrum of Cy5.5. It is useful to note that, while typically there is a tradeoff between detector responsivity and bandwidth, the bandwidths needed for observing biological systems (typically less than a few kHz) are easily achieved with PIN designs.

semiconductor device growth and subsequent processing. The main issues to consider in choosing the relative placements of the laser and detector are the quality of the epitaxial layers and the potential optical crosstalk between the laser and detector. Since detector dark current in GaAs etched-mesa photodiodes is limited by carrier generation from surface defect states of the thick absorption region, and not bulk crystal defects [31, 106], the noise performance of the detector is not expected to be highly dependent on the epitaxial growth quality of the bulk PIN layers.

The more critical element for this biosensor design is thus the high-quality VCSEL epitaxy, especially for the lasers at shorter wavelengths like 670 nm, as these require more DBR pairs. Hence, the VCSEL layers were grown on the substrate first, followed by the PIN photodetector, in a single recipe using metal organic vapor phase epitaxy (MOVPE). Measurements confirmed that the photodetector quality, specifically the dark current noise contribution, was not adversely affected by the presence of the underlying VCSEL.

The two primary sources of noise in photodiodes are shot noise, from both photon arrival and dark current, and thermal (Johnson-Nyquist) noise [51]. Dark current induced shot noise is also known as Generation-Recombination (GR) noise. These sources of noise can be represented by the following equations:

$$\text{Photon shot noise: } i_{shot}^2 = 2qI_{photo}B \quad (4-1)$$

$$\text{Generation-Recombination noise: } i_{GR}^2 = 2qI_{dark}B \quad (4-2)$$

$$\text{Thermal noise: } i_{thermal}^2 = \frac{4kTB}{R} \quad (4-3)$$

where I_{photo} is the photocurrent, I_{dark} is the dark current, B is the bandwidth of the measurement, R is the shunt resistance if the photodiode is modeled as a resistor, q is the

elementary charge of an electron, k is the Boltzmann constant, and T is the temperature.

The total noise is thus the sum of each noise source:

$$i_{noise}^2 = i_{shot}^2 + i_{G-R}^2 + i_{thermal}^2 \quad (4-4)$$

where i_{G-R}^2 can be affected the most with device engineering. The sensitivity of a photodetector is defined as the amount of light power detectable with a SNR of unity, and can be expressed as the noise equivalent power (NEP):

$$NEP = \frac{i_{noise}}{\Re} \quad (4-5)$$

in Watts/ $\sqrt{\text{Hertz}}$, where \Re is the responsivity of the detector in units of Amperes/Watt.

Thus, for a high sensitivity photodetector, one must maximize responsivity and reduce noise whenever possible. Shot noise from photon arrival is a fundamental, unavoidable factor that ultimately limits the detector sensitivity. At low bandwidths, the thermal noise near room temperature, or even at elevated temperatures when the VCSEL is being tuned, has a magnitude much smaller than that of shot noise sources. Hence, our efforts are concentrated on reducing i_{G-R}^2 , which is dependent on the dark current. The design choice of GaAs for the detector material already provides $\sim 10x$ lower dark current in comparison with Si photodiodes due to GaAs' lower intrinsic carrier concentration. Additional engineering of detector mesa sidewalls, with various passivation techniques [37] helps reduce the detector noise even further. The monolithically integrated GaAs photodetector was found to generate less than 5.0 pA/mm^2 dark current, when measured at reverse bias values up to 1 V, with internal quantum efficiencies η_{QE} greater than 75%.

While a single detector design responsivity – whose responsivity is shown in Figure 4-4 – can be used for operation from 650 nm to approximately 870 nm (which

corresponds to the band gap of GaAs at 1.42 eV), the VCSEL designs required for wavelengths spanning that range are quite different. As mentioned in Section 2.3, VCSELs at 670 nm need nearly double the number of $\lambda/4$ mirror layers required for 850 nm VCSELs, as the change in material composition to avoid absorption at shorter wavelengths results in reduced index contrast in the DBRs. The combination of thicker DBRs and lower thermal conductivity represents a significant design problem, particularly for biosensing applications where the operating temperature may need to be relatively high (near body temperature) and heat sinking is difficult.

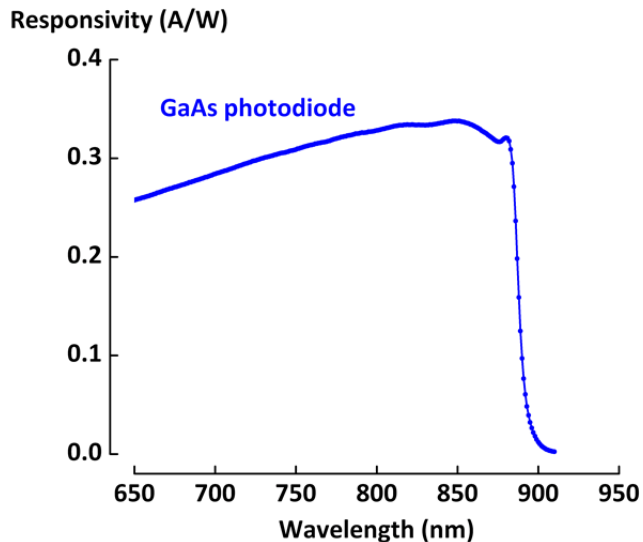


Figure 4-4: Responsivity vs. wavelength for a GaAs photodiode. The roll-off at ~870 nm corresponds to the band gap of GaAs at 1.42 eV.

Despite these technical challenges, operating at 670 nm is crucial for compatibility with FDA-approved fluorophores and emerging fluorescent proteins. Hence, fabrication processes were optimized to achieve integrated VCSELs at 670 nm, and a hybrid configuration incorporating additional industrial-grown VCSELs (MCom and Vixar, Inc.) with improved performance metrics was explored. Figure 4-5 depicts the layout of the monolithically integrated VCSEL/detector module, with two lasers (for design and test

flexibility) bonded onto an 8-pellet pair TEC. To facilitate testing, some of the TEC/VCSEL/detector units featured additional VCSELs of different wavelengths bonded on the top TEC plate and wired to vacant header pins. This enabled the characterization of photonic crystals resonant in different regimes by simply selecting different header pins in a custom MATLAB interface, without unplugging the header from its corresponding socket. In order to monitor the temperature of the die and of the ambient environment during experiments, a 40 gauge (0.076 mm diameter) insulated precision thermocouple (Omega Engineering, 5SRTC-TT-T-40-36) was added with conductive epoxy and paired with a digital recording thermometer with an accuracy of $+/- 0.1$ °C (Omega Engineering, HH-506-RA). Figure 4-6 shows a photograph of a 4-pellet pair TEC, with VCSELs, the detector, and the thermocouple.

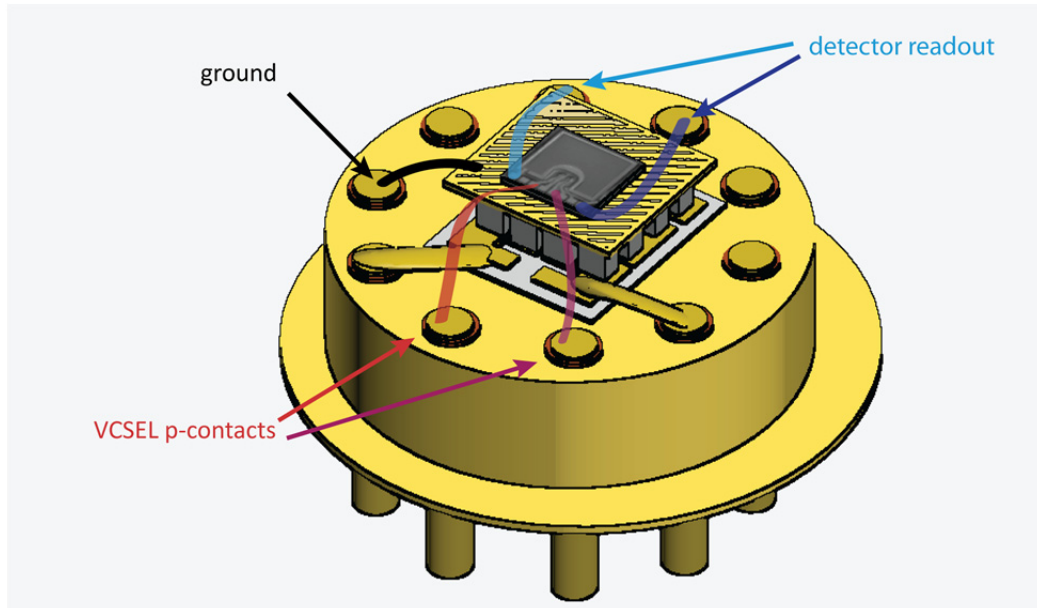


Figure 4-5: Layout design of the TO-5 header. A monolithically integrated pair of VCSELs and detector, with two VCSEL p-contacts and the detector readout signal occupying 4 pins, is bonded on an 8-pellet pair TEC. Thicker gold ribbons are used to provide larger ampacity for the TEC biasing. For TECs that are not metallized, a 0.5 mm thick quartz spacer coated with gold is bonded in between the TEC top ceramic plate and the laser dies to provide a ground plane.

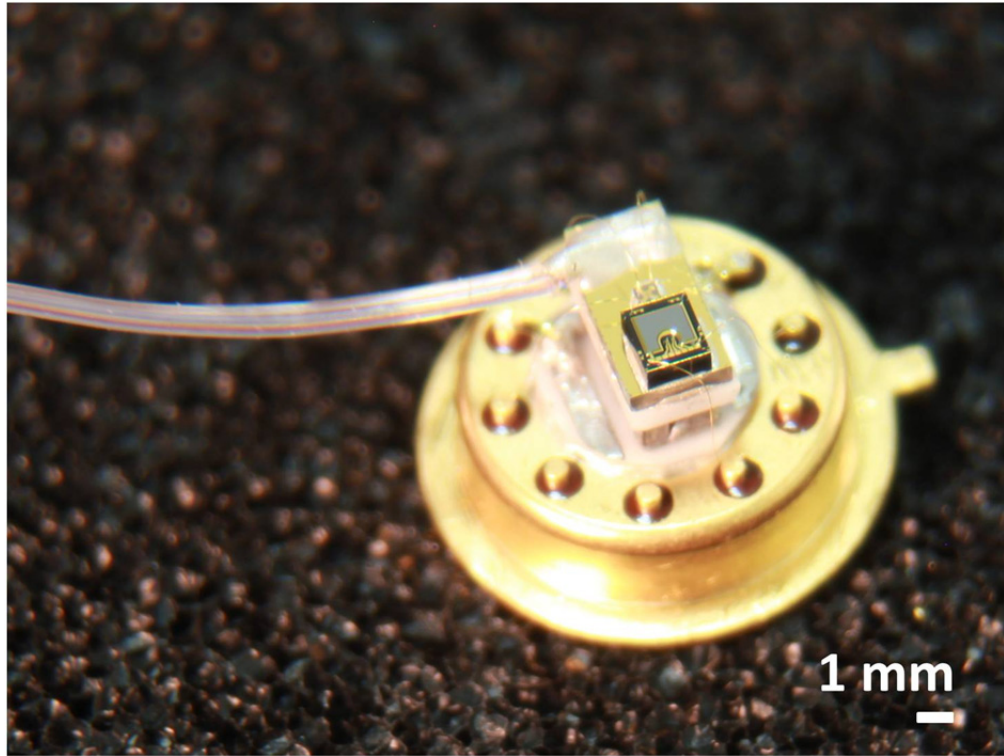


Figure 4-6: Photograph of a trimmed and bonded 4-pellet pair TEC, with an integrated VCSEL/detector, additional VCSELs, and the thermocouple, utilizing a TO-5 transistor header package. After the VCSEL/detector, extra VCSELs, and thermocouple are bonded to the TEC and wired to the header pins, a TO-can enclosure and collimating lens can be added.

4.1.2 Packaging and Measurement Setup

The TEC/VCSEL/detector modules were attached with epoxy to the center of standard TO-5 transistor packaging headers that have 10 pins, visible along the perimeter of the header in Figures 4-5 and 4-6. The typical pin wiring, as shown in Figure 4-5, includes top p-contacts for each VCSEL and readout contacts for the photodetector. Since the monolithically integrated VCSELs share a back n-contact that is connected to ground, each additional VCSEL only requires one header pin. For the initial tests with 4-pellet TECs that did not include a metallized ceramic top plate, a 0.5 mm quartz spacer with a

gold top layer was bonded on the top ceramic plate to provide a ground plane. The plane facilitated intermediate bonds that were sometimes needed when designing different layouts of lasers and detectors, so that no wires would interfere with the light traveling from the VCSELs to the photonic crystals and back to the detectors.

While multiple lasers can share the ground plane, care is taken to isolate the VCSEL and TEC driving current (on the order of a few mA to hundreds of mA, respectively) from the detector readout current (often on the order of pA and nA). This is achieved by splitting the signals from the 10 pins of the header into two DB-9 cables, one for biasing the TEC and VCSELs, and the other for receiving the photocurrent signal from the detectors, with each pin having metal shielding layers in addition to thermal insulation. Although standard 80 gauge gold wire was used to bond the contacts for the VCSEL and detector to the header pins, to provide larger ampacity (current-carrying capacity) for the TEC and allow us to fully characterize the temperature performance of our sensor, two to three gold ribbons, each 10 mils by 0.5 mils, were chosen to connect the TEC pads to their header pins.

The header sockets and DB-9 cables link the packaged TEC/VCSEL/ detector module to the rest of the measurement equipment. A laboratory cart with benchtop current sources, a lock-in amplifier, and a switchboard (described in more detail in the Appendix) is used to power, control, and measure the electronic signals. Figure 4-7 illustrates the main data paths for the electronics, with all communication utilizing IEEE-488 General Purpose Interface Bus (GPIB) connections and with the commands controlled by a MATLAB interface on a laptop computer.

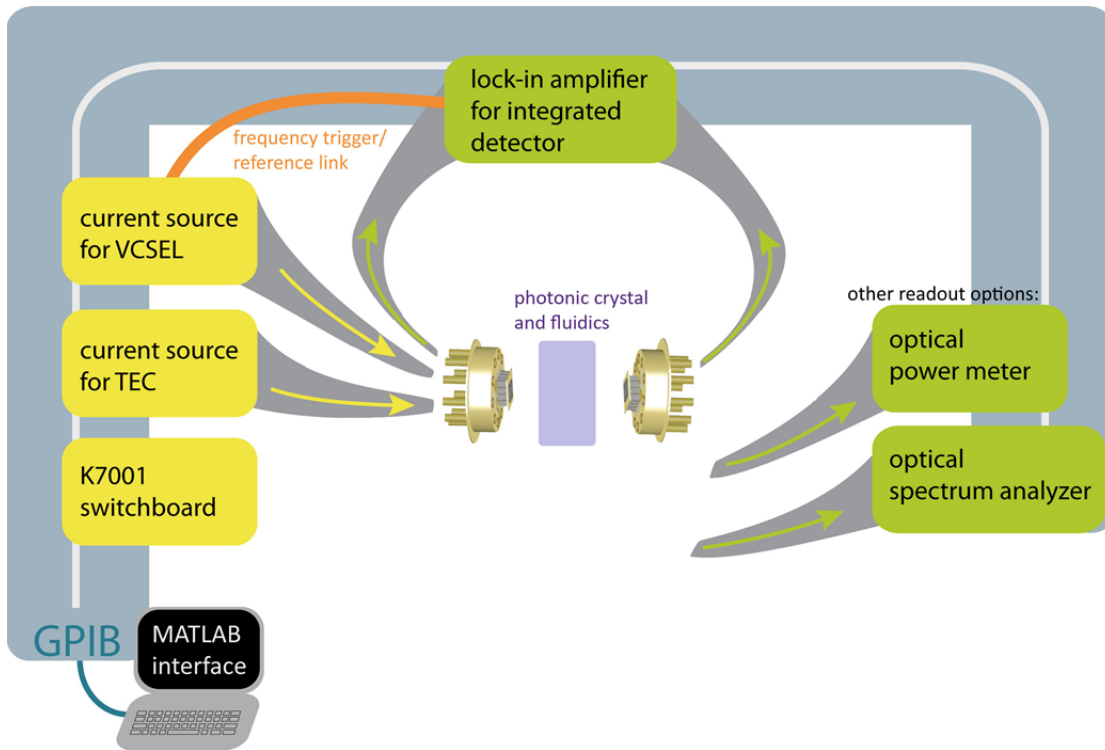


Figure 4-7: Diagram of laboratory testing equipment connections enabling characterization of the TEC/VCSEL/detector and photonic crystal in reflection and transmission, with GPIB protocols and a MATLAB interface.

In addition to designing the characterization setup to test the TEC/VCSEL/detector in a reflection configuration (with only one TO-5 package, driven by the equipment labeled yellow in Figure 4-8), we incorporated additional readout options to measure the TEC/VCSEL performance and photonic crystal response in a transmission configuration with a second TEC/VCSEL/detector unit. The reflection and transmission configurations will be utilized to demonstrate refractive index sensing in Chapter 5. This represents the two application spaces of *in vivo* and *in vitro* sensing, with the transmission-mode being restricted to *in vitro* applications or thin transparent *in vivo* studies (e.g., in skin), but providing higher power if needed. In practice, we found that the reflected signal off the photonic crystal could be readily used, with photocurrents on the order of nA (the transmission configuration resulted in currents that were several 100s of

nA), depending on how far away the photonic crystal was placed and if any collimating elements were inserted between it and the TEC/VCSEL/detector. One can recall that for fluorescence sensing mentioned in Chapter 2, the signal was lower (due to absorption), on the order of pA to nA, and noise was measured to be 5.0 pA/mm².

Moreover, since our label-free refractive index sensor features a transparent photonic crystal designed for minimum absorption loss, the photocurrent measured in transmission-mode was, as expected, ~3 orders of magnitude higher than that measured by the integrated detectors in a reflection configuration.¹¹ This means that the readout circuitry (in this case, the lock-in amplifier time constant and sensitivity settings) needs to be adjusted according to which geometry is employed. Furthermore, if one wanted to operate both of the detectors in the diagram shown in Figure 4-7 for sequential or simultaneous reflection and transmission measurements, separate amplifier circuitry for each configuration would likely be needed.

Figure 4-8 shows an example of photocurrent that was measured by the integrated detectors as a function of VCSEL bias. The shape of the curve follows the derivative of typical LI curves as expected, since the VCSEL is biased with an Alternating Current (AC) 1 mA sinusoidal peak-to-peak wave at 23 Hz overlaid on the standard DC biasing condition. This biasing scheme was used for both reflection and transmission measurements, to enable use of a lock-in amplifier to reduce electrical noise.

¹¹ Since the photonic crystal modulates the transmitted and reflected light by introducing a high reflectivity peak or transmission dip at certain wavelengths, here we refer to the photocurrent measured off-resonance, when the photonic crystal essentially transparent.

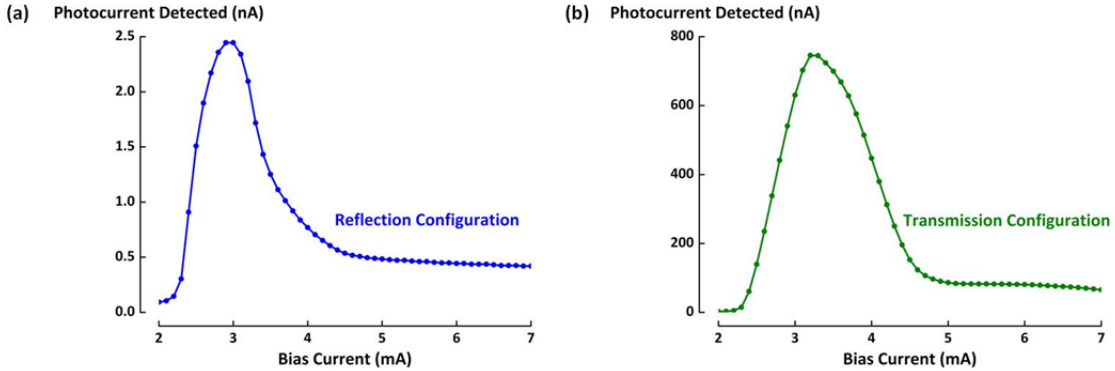


Figure 4-8: Measured photocurrent from the integrated detector in (a) reflection and (b) transmission configurations.

When not employing the integrated low-noise GaAs detector as the signal receiver, the laboratory test setup enabled characterization with a calibrated Newport 818-SL silicon photodiode and Newport 1830-C optical power meter. Another readout option for the characterization setup was to view the transmitted light, after a stage of fiber-coupled collimating optics, with an optical spectrum analyzer or a handheld spectrometer. Although the sensor's reflection design is clearly the most compact, each of these alternative configurations was employed to more fully characterize the VCSEL. For a solution more portable than the cable and socket design, the cabling and cart electronics can be replaced with a printed circuit board (PCB) and powered with a battery. As recently demonstrated [107], a CMOS low-noise current readout circuit with a capacitive transimpedance amplifier can reduce the noise from the cables, and serves as the next step towards wireless operation and data collection. A photograph of the miniature PCB with the integrated VCSELs and detectors bonded in place was shown earlier in Figure 1-2, below the photonic crystal and microfluidic delivery chip.

For flexibility in optical alignment adjustments and ease of re-bonding connections, most TEC/VCSEL/detector modules were tested with the wire bonds exposed. Moreover, the open configuration allowed space for the off-the-shelf precision

thermocouple wire without the need to route the wire out of a cap enclosure. However, as shown in Figure 4-9, the full packaging features a snugly fitting TO-cap to surround the transistor header. Starting from a standard cap, apertures were created through the top of the caps to allow for eventual attachment of a collimating lens, and the cap was spray-painted with matte black paint to minimize stray reflections. In future iterations of packaging, the thermocouple signals could be routed from the bottom, or integrated temperature and humidity sensors could be utilized.

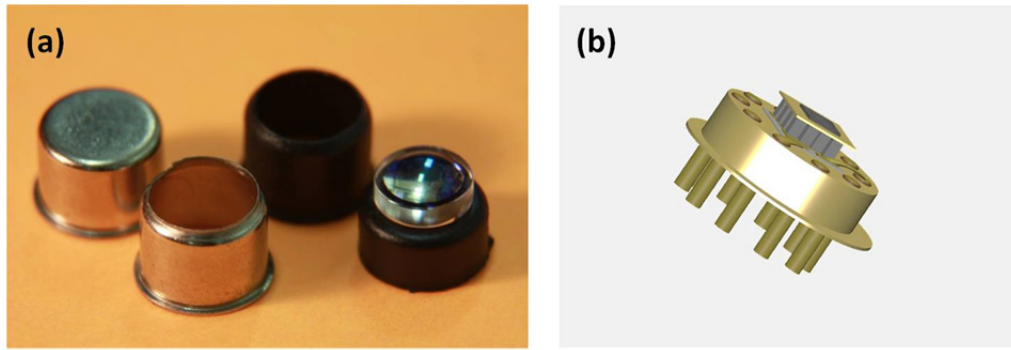


Figure 4-9: (a) TEC/VCSEL/detector packaging enclosure. An aperture is created on a standard TO-cap before it is spray painted matte black to prevent stray reflections, and an aspheric collimating lens is added. (b) The cap fits snugly over the TO-5 headers (shown here in a side view) that hold the TEC/VCSEL/detector.

4.1.3 TEC Performance

The TECs, VCSELs, and detectors were characterized independently before assembly to increase the overall yield. The primary TEC characteristics and performance metrics of interest for our label-free sensing scheme include the pellet resistance (as a check for functionality), maximum difference in temperature between the two plates (ΔT_{max}), maximum heat absorbed (Q_{max}), input bias current, and time required to cool or heat an object. The first indicator of functionality was the measured resistance value of the P and N pellet series; the TECs were verified with a precision multimeter to have

resistance values on the order of 0.2 - 1 Ω before and after the TEC was trimmed and bonded to the TO-5 header.

The VCSEL temperature range for our refractive index sensing was chosen to be ~ 8 °C to 50 °C measured at the VCSEL die ground plane on top of the TEC top plate. This corresponds to the coldest temperature that, with a room dehumidifier, would reliably avoid condensation that could short the optoelectronics, and the highest temperature where the VCSEL would still lase. This range was well below the DTmax of the TECs used (which was specified at 67-70 °C), so was not critical. Similarly, the Qmax specification for the TECs was 0.5 W, which was more than adequate to accommodate the heat generated for extended VCSEL tuning (0.13 W). Input currents used for extended tuning ranged from -350 mA (for cooling to ~ 8 °C) to 350 mA (for heating to ~ 50 °C).

The input currents were specified in a MATLAB-controlled script that ramped the TEC bias gradually, and could be programmed to pause long enough to allow the temperature to settle. This is critical since the TEC biasing (and the resulting temperature at the VCSEL), in combination with the VCSEL biasing, sets the intensity and wavelength of the laser. Since our sensing scheme consists of measuring the laser intensity reflected off our photonic crystal for a range of VCSEL wavelengths, the full characterization of the tunable VCSEL required an examination of all biasing transients. The 40 gauge insulated precision thermocouple and digital recording thermometer were used to record the temperature at the VCSEL and of the ambient environment simultaneously. With this data on the settling time (which was dependent on the initial conditions and temperature gradient desired), the MATLAB control script was adjusted to allow for stabilization during various tuning routines. Figure 4-10 depicts a typical time response for the TEC, with settling times on the order of 40 seconds for a few degrees change in temperature.

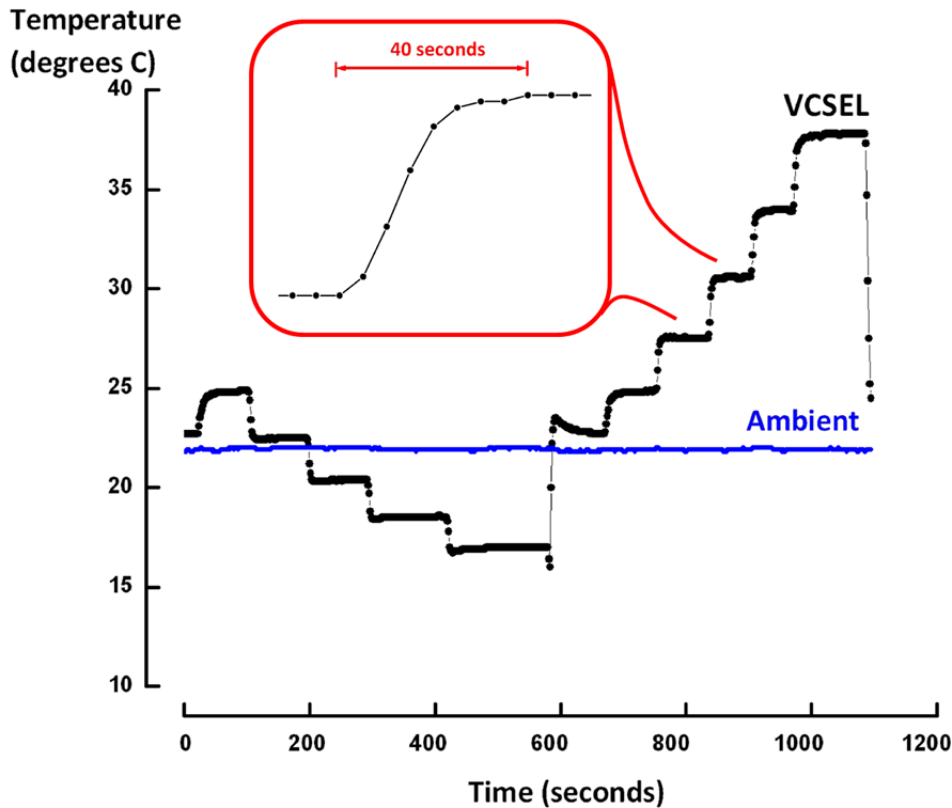


Figure 4-10: Time transients were observed, as expected, during thermal tuning. In this example, we cool and heat the VCSEL biased above threshold, by stepping the current driving the TEC every 100 seconds. Typical transients last 40 seconds as we ramp the TEC current 50-75 mA every 100 seconds.

4.1.4 VCSEL Performance

After characterizing the TEC, the VCSEL performance was measured. The main goal of the VCSEL characterization was to identify the wavelength tuning range and note the beam quality (e.g., stability, spectrum, divergence) to determine if our tuned VCSEL and integrated detector could replace the traditional broadband source and spectrometer. The primary results of interest used to determine the viable wavelength tuning range were the optical output as a function of current (LI curve) that depicted the laser threshold at different temperatures, the optical spectrum as a function of biasing conditions, and the

spatial mode profile. Since our photonic crystal features all-dielectric low-loss materials, and the absorption through many biological specimens at VIS-NIR wavelengths is low, the power output of the VCSEL (on the order of ~1 mW) was sufficient for both transmission and reflection detection. Figures 4-11 and 4-12 illustrate measured LI curves at different TEC biasing conditions, for 670 nm and 822 nm VCSELs. In each of the measurements, the LI curve for different temperatures was recorded using a calibrated Newport 1830-C optical power meter; the thresholds were noted so that we could operate at ~10% above threshold at various temperatures to achieve stable lasing, while maintaining single-mode emission and avoiding large bias currents that lead to multi-mode behavior.

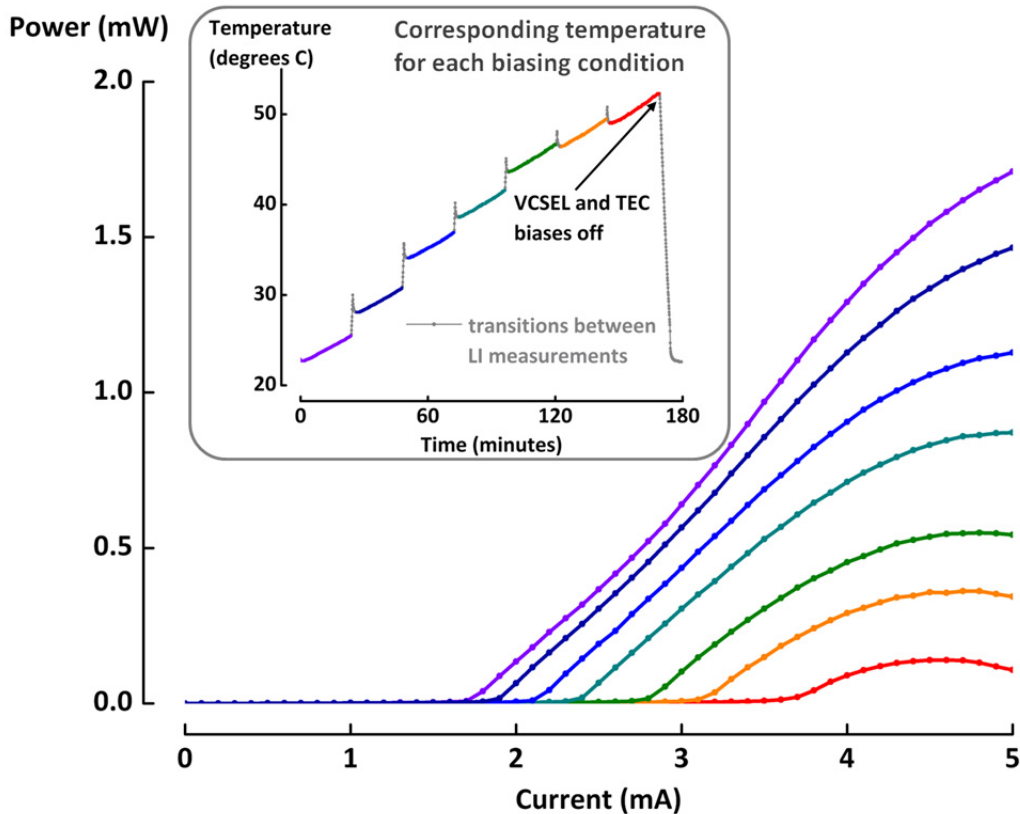


Figure 4-11: LI curve for a 670 nm VCSEL at seven different temperatures ranges set by the TEC. The VCSEL current biases shown here represent the full operating range (5 mA maximum current), hence we observe rollover.

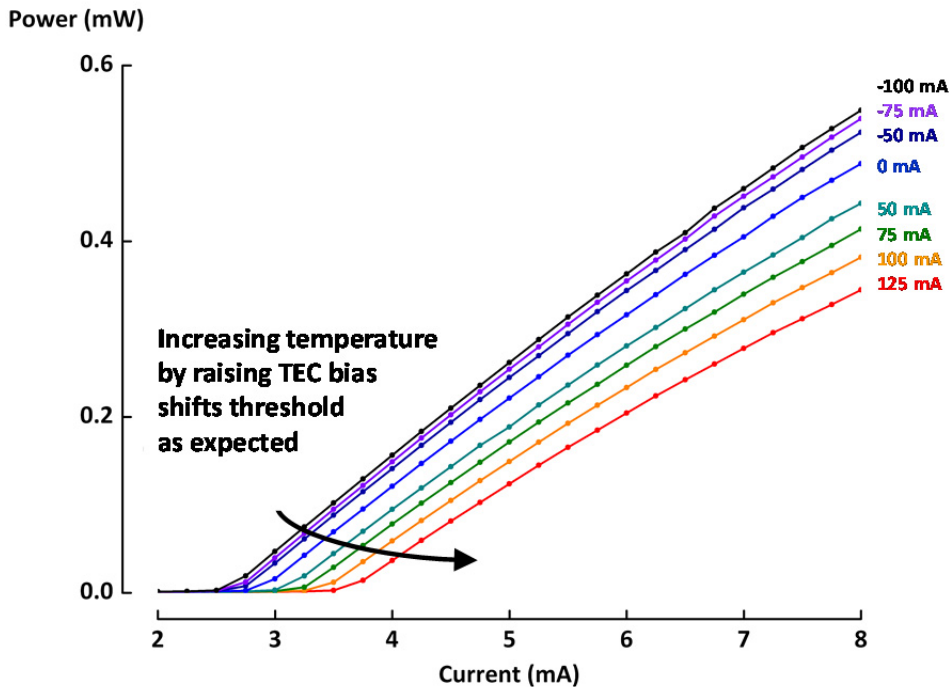


Figure 4-12: LI curve at eight different TEC settings (-100 mA, -75 mA, -50 mA, 0 mA, 50 mA, 75 mA, 100 mA, and 125 mA) and their corresponding temperature ranges (~10-15 °C, 15-17 °C, 17-20 °C, 24-27 °C, 32-35 °C, 36-40 °C, 41-45 °C, and 48-51 °C), for a 822 nm VCSEL. Compared to the operating conditions used in Figure 4-11, this VCSEL is being operated at current biases closer to threshold (not reaching the 12 mA maximum operating current).

In Figure 4-11, the VCSEL bias was ramped from 0 mA to the maximum operating current (5 mA for this laser) for each of seven TEC bias settings. The corresponding thresholds for each of these settings were 1.7 mA, 1.9 mA, 2.1 mA, 2.35 mA, 2.75 mA, 3.1 mA, and 3.6 mA. As expected, one can clearly observe rollover, especially in the higher temperature data. In order to preserve single-mode behavior, the biasing chosen for each VCSEL was closer to threshold. In addition to optimizing the TEC and laser biasing conditions and measuring the power output, it was crucial to view the frequency or wavelength content of the emitted light. An OSA was used for VCSEL linewidth

characterization, along with an external collimating lens and fiber-coupler. In general, the expected center lasing wavelength for a M -lambda cavity can be described as

$$\lambda_C = \frac{2 \sum_i n_i l_i}{M} \quad (4-6)$$

where n_i and l_i represent the refractive index and thickness of each layer in the cavity, and $\sum_i n_i l_i$ forms an effective cavity length. A change in temperature affects not only the thickness of the layers (through thermal expansion), but also the refractive index. The thermal tuning of the laser cavity resonance can be obtained by differentiating both sides of Equation 4-6. This leads to:

$$\frac{1}{\lambda_C} \frac{\partial \lambda_C}{\partial T} = \frac{\sum_i \alpha_i n_{i0} l_i + \sum_i \beta_i n_{i0} l_{i0}}{\sum_i n_{i0} l_i} \quad (4-7)$$

where n_{i0} and l_{i0} are the initial refractive index and material thickness at room temperature, respectively. α_i and β_i represent the temperature coefficients of the index change and thermal expansion, respectively, and are related to temperature by the following expressions:

$$n_i = n_{i0}(1 + \alpha_i \Delta T) \quad (4-8)$$

$$l_i = l_{i0}(1 + \beta_i \Delta T) \quad (4-9)$$

where ΔT is the change in temperature [108]. Figures 4-13 and 4-14 show the spectra for a 670 nm VCSEL at room temperature¹² and highlight the quick progression from a narrow FWHM to a broader multi-mode line shape if current tuning is employed.

¹² The TEC is not biased for this test; however, there is self-heating from the VCSEL such that the higher VCSEL input currents will raise the effective operating temperature. For example, operating just above threshold at 1.75 mA versus at the maximum input current of 5 mA results in a change in measured die temperature on the order of a few degrees.

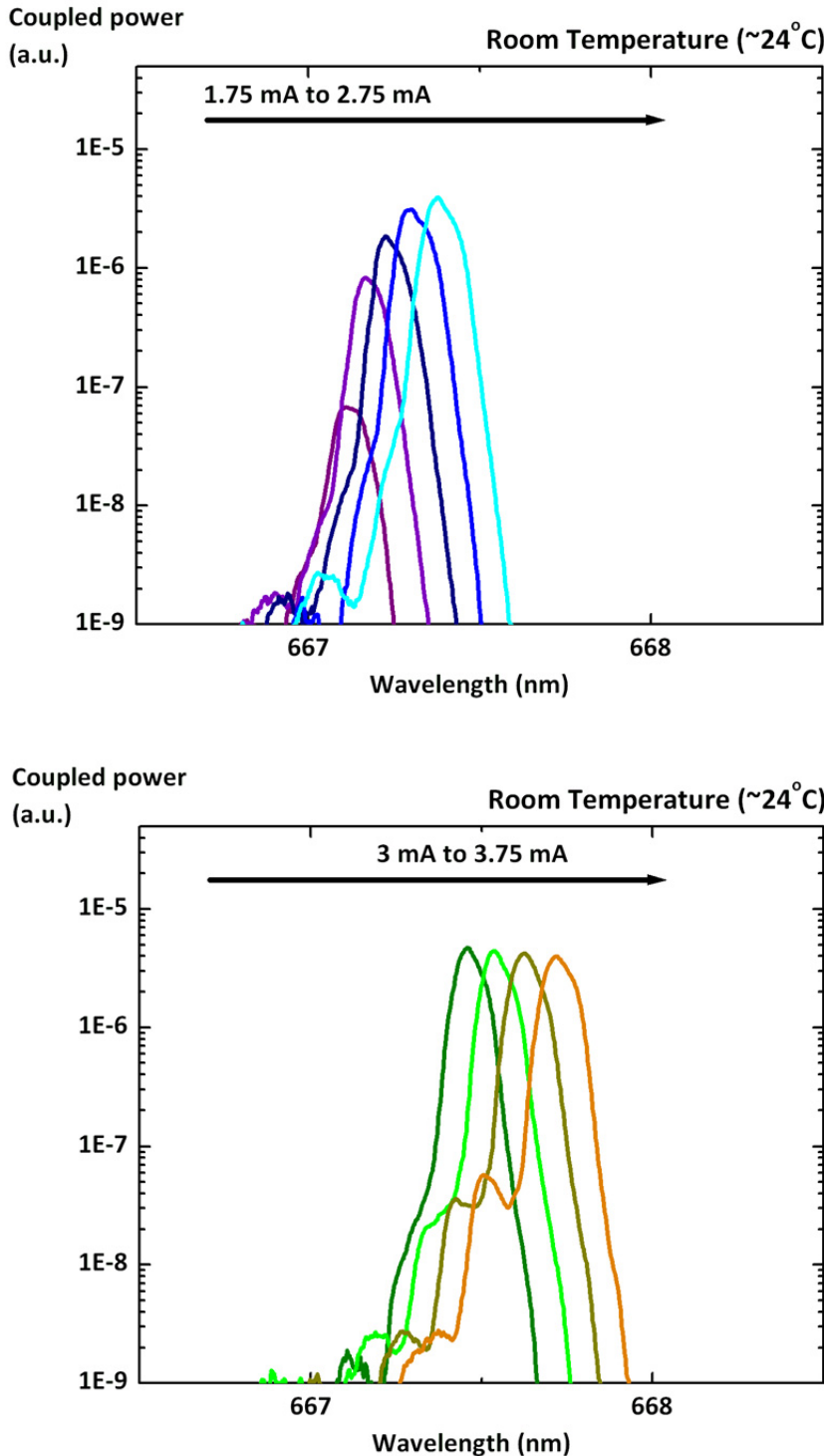


Figure 4-13: Power spectra for a 670 nm VCSEL under current tuning. Each curve represents an increment of 0.25 mA. A ~ 0.2 nm FWHM is seen through moderate biases, with more than 3 orders of side mode suppression near threshold.

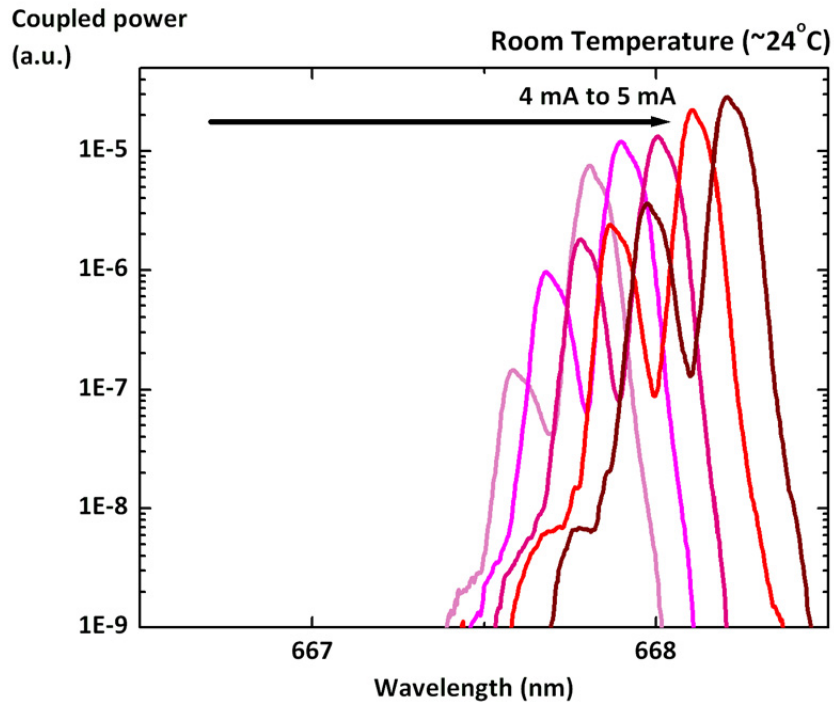


Figure 4-14: Power spectra for the same 670 nm VCSEL shown in Figure 4-13, now biased from 4 to 5 mA, again in increments of 0.25 mA. The effective FWHM has broadened significantly in this multi-mode regime.

Since single-mode operation will result in better wavelength resolution when recording the intensity spectrum during refractive index sensing, the VCSEL mode profile was investigated further. Because a VCSEL's cavity length is on the order of $2 \mu\text{m}$, only a single longitudinal mode should have enough gain to lase¹³. Generally, the laser designer aims to align this longitudinal mode near the center of the gain bandwidth spectrum to allow tuning in both directions; for lasers intended for only cooled or only heated operation, the alignment can be shifted for optimum overlap. The data in Figures 4-13 and 4-14 and similar data observed at different temperatures are consistent with a single

¹³ A VCSEL's short cavity yields mode spacing that is spread more sparsely than edge-emitting laser longitudinal modes. As a consequence, secondary longitudinal modes do not overlap the gain spectrum.

longitudinal mode, and the appearance of multiple transverse modes. These transverse modes can also be viewed spatially with the aid of a camera to help determine the best operating parameters for high-resolution label-free sensing. Figure 4-15 shows the measured profile of a single-mode 822 nm VCSEL matching our desired beam quality.

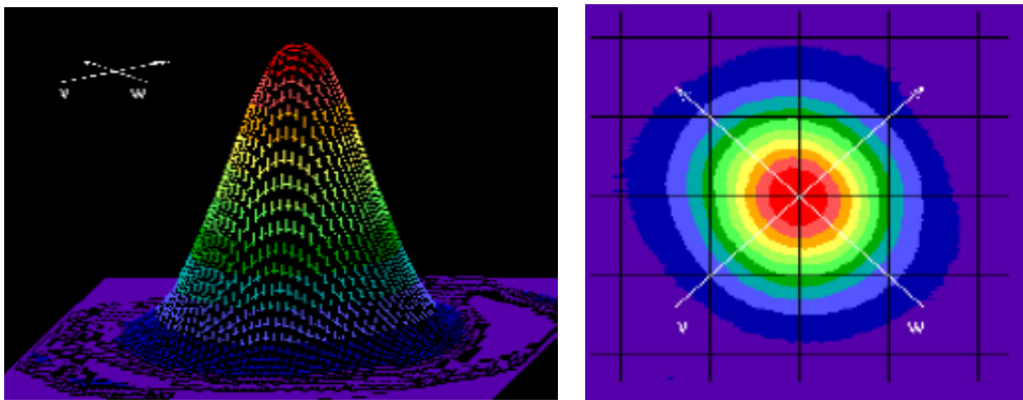


Figure 4-15: Measured 822 nm VCSEL 3D and top-view beam profile showing single-mode, circular beams. Beam profile cameras were used in conjunction with an optical spectrum analyzer to investigate the presence of transverse modes.

With a combination of viewing VCSEL linewidths with our OSA and the use of beam profiling cameras, VCSELs that were able to produce single-mode lasing were selected. For our limited sample size, this meant discarding ~2 VCSELs out of nearly 50 bonded and tested lasers; in industrial manufacturing settings, many of these tests can be performed at the wafer level as part of a cost-effective yield management process.

After selecting VCSELs based on the LI curves, current tuning spectra, and beam profile, the precision tuning of the wavelength was further examined. Current tuning provided a wavelength shift of ~0.4 nm/mA, while temperature tuning provided ~0.06 nm/ °C. This means that to shift the lasing wavelength 1 nm from current tuning, one must change the VCSEL bias ~2.5 mA; from Figure 4-14, we saw that this can lead to a drastic change in the spectrum linewidth, greatly reducing the detection resolution

capabilities. In comparison, shifting the lasing wavelength 1 nm by temperature tuning can still result in a single-mode peak, with ~ 3 orders of magnitude side mode suppression, as shown in Figure 4-16, and is preferable whenever possible.

For a measurement setup with a thermocouple and digital recording thermometer precision ± 0.1 °C, controlling the temperature reliably in steps of 0.5 °C yields an incremental wavelength control of ~ 0.03 nm. This is smaller than the minimum linewidth that can be measured with our laboratory OSA (0.08 nm), providing excellent wavelength resolution for label-free sensing without the need for large and bulky spectrometers. More importantly, temperature tuning offers a repeatable means of tuning the center VCSEL wavelength while maintaining a narrow linewidth.

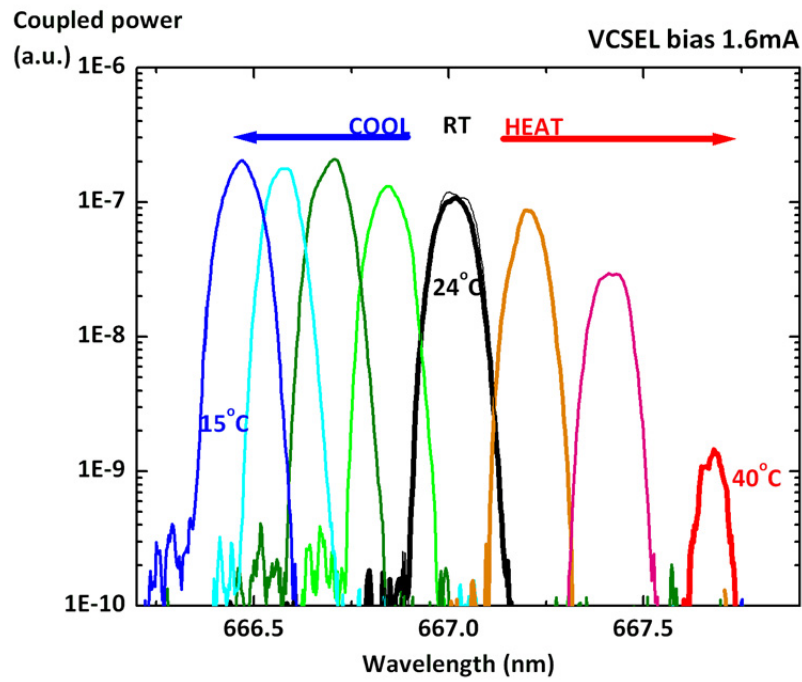


Figure 4-16: With the 670 nm VCSEL held above threshold at a low bias of 1.6 mA, temperature tuning provides a precise shift, while preserving the laser's narrow linewidth.

As Figure 4-16 illustrates, the optical spectrum measured at a steady 1.6 mA VCSEL bias under different temperature conditions is narrow and can be tuned 1.5 nm without compromising linewidth for a 670 nm laser. In VCSELs fabricated for longer wavelengths, the thermal challenges are much more manageable, and the resulting single-mode tunability ranges can be larger (for example, with over 5 nm range at 780 nm and ~9 nm at 850 nm), depending on the success of thermal device engineering efforts. As we will see in Chapter 5, obtaining larger VCSEL tuning ranges would be useful for many applications where a wider wavelength spectrum would ensure that the photonic crystal resonance falls within the VCSEL range. Achieving extended VCSEL tuning ranges greater than ~10 nm necessitates the implementation of more complex structures such as MEMS-tunable DBR elements [100, 101, 103-105], and can be an attractive option.

The final two TEC/VCSEL/detector characterization measurements of note are the intensity stability over time, and the beam divergence. While intensity drift can be measured or normalized by monitoring a nearby VCSEL in the same array or regulating the VCSEL current bias, such measures may not be necessary in many cases. VCSELs are known to be extremely stable and are regularly employed for demanding optical communications, sensing, and metrology applications. Figure 4-17 shows an example trace of a VCSEL biased at 3 mA for over 2 hours. We observe that there is ~0.7% peak-to-peak variation in intensity over this duration. VCSEL lifetimes are known in industry to easily surpass 100000 hours [109-111], and are thus an advantageous source compared to less efficient and shorter lifetime broadband sources such as Quartz Tungsten Halogen (QTH) bulbs.

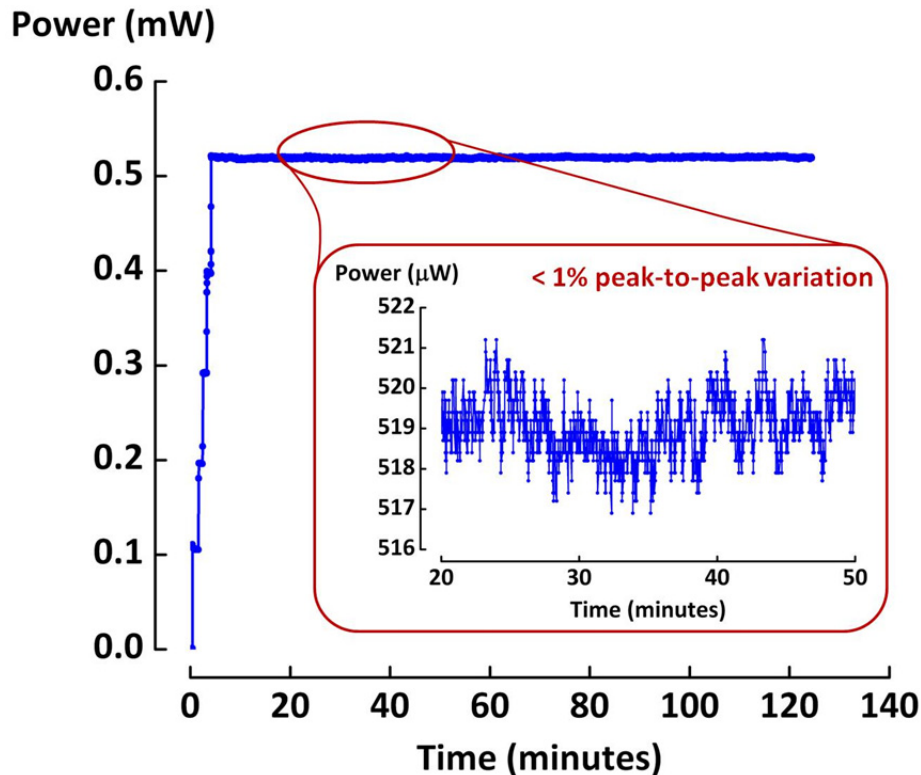


Figure 4-17: Power of a 670 nm VCSEL biased at 3 mA, where the laser threshold was 1.5 mA, measured for over two hours. The peak-to-peak variation was ~0.7%.

In addition to measuring long-term stability at various bias points, we examined the transients in power that result from rapid switching of bias conditions (replicating the bias sequence that will be used in Chapter 5 to sweep the wavelength during label-free sensing). The settling times, as well as the absolute values of the power output for various TEC and VCSEL bias pairs, are crucial to orchestrate the measurement of the intensity vs. wavelength for different aqueous solutions during label-free sensing. Just as the background “envelope” spectrum of a white light source is subtracted to enable clear viewing of spectral shifts in conventional spectrometer-based label-free sensing, VCSEL and point-detector-based sensing benefits from background subtraction. In our configuration, the background is the LI curve.

Figure 4-18 depicts this LI curve for a 822 nm VCSEL with 50 mA driving the TEC and various bias points for the VCSEL current. With each point (3.5 mA, 4 mA, 4.5 mA, 6 mA, and 12 mA shown) held for 1000 seconds, one can see the power is stable for the biasing conditions most used in this work, and also at the higher 6 and 12 mA bias points, after a slight transient that occurs when switching the bias conditions. This time lag was consequently used to set pauses in the MATLAB characterization scripts during the refractive index sensing measurements described further in Chapter 5. Similar graphs were created for numerous TEC and VCSEL biasing configurations, to quantify both the settling times and the laser power for each biasing pair.

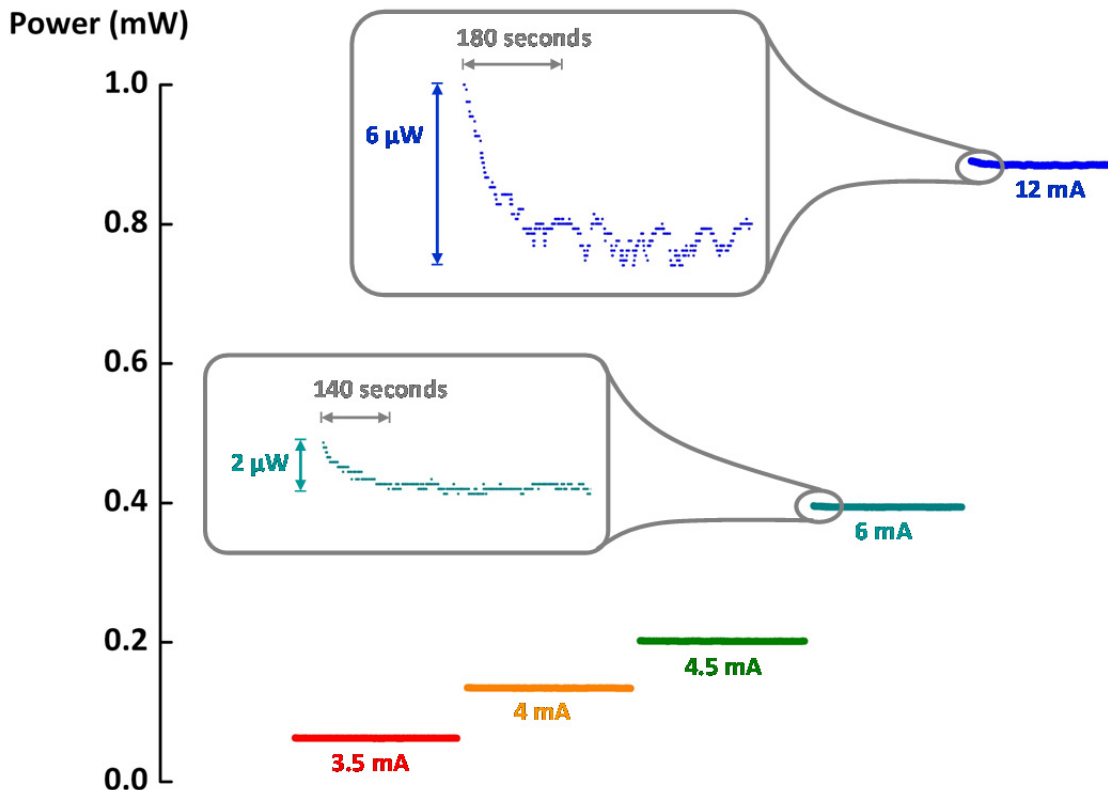


Figure 4-18: Stable transmitted power for a 822 nm VCSEL with 50 mA driving the TEC and different VCSEL bias points (3.5 mA, 4 mA, 4.5 mA, 6 mA, and 12 mA shown here), each held for 1000 seconds.

Besides the power, frequency content, single- or multi-mode lasing, tunability, and transient behavior shown in this section thus far, the beam divergence is a useful performance metric. Divergence of a laser beam is a measure of how fast the beam expands from its waist, describing how parallel or collimated the light rays are as they travel away from the source. Our VCSEL divergence was measured with a 14-bit 1.4 MPixel CCD camera (WinCamD UCD12, DataRay, Inc.), and for numerous units tested, had a half-width $1/e^2$ value of 7-9°. This is quite narrow, especially compared to the ~30° half angle divergence that one would measure for typical fiber-coupled QTH lamps or LEDs. As will be discussed further in Chapter 5, the divergence is important for engineering packaging elements such as collimating lenses or micro-optics lens arrays for arrayed VCSELs, and for ensuring as-designed optical responses from near-normal-incidence probing of the photonic crystal.

4.2 Photonic Crystal Slabs and Fluidic Delivery

To fabricate the VIS-NIR photonic crystals described and simulated in Chapter 3, both well-developed and emerging processing techniques were used. This section describes the deposition, patterning, and etching processes for the all-dielectric photonic crystal structures. We then discuss surface treatment for the photonic crystal and fluidic chamber design to enable bulk sensitivity characterization.

4.2.1 Thin Film Deposition

Starting with a fused silica substrate (Hoya, 4W55 high precision wafer) that has undergone a Piranha clean of 5:1 Sulfuric Acid: Hydrogen peroxide at $\sim 110\pm10$ °C for 20 minutes, a layer of stoichiometric SiNx is deposited with Plasma Enhanced Chemical

Vapor Deposition (PECVD) or Low Pressure Chemical Vapor Deposition (LPCVD). PECVD was most often used, as it allowed for low-temperature, low-stress deposition films with a platen that could easily accommodate pieces and wafers of various types. A cleaning cycle was first run to coat the walls of the deposition chamber with nitride, followed by a calibration sample that was used to measure the as-grown SiNx thickness on Si and fused silica dummy samples, before deposition on the actual target sample. The nitride deposition consisted of 2% Silane (SiH_4) at 2000 sccm and 100% Ammonia (NH_3) at 35 sccm. Uniformity was measured with an ellipsometer to be within 1% over a 4 inch wafer, after approximately 30 minutes of deposition to reach a 250 nm thick film.

4.2.2 Interference Lithography

While today's lithography equipment used in the semiconductor industry can pattern transistor gates on the order of 25 nm, the lithography processes available at a research university nanofabrication facility are limited, with patterning tools often having a resolution on the order of 1-2 μm . Many researchers consequently utilize electron beam (e-beam) lithography to define photonic crystal structures. However, for large area patterning, e-beam lithography requires stitching of exposed areas together, causing alignment issues; moreover, it is a serial process, writing one feature at a time, and as a result, can be extremely time consuming and costly.

Consequently, we looked to alternatives for defining our 150-200 nm diameter photonic crystal features, with interference lithography and nanoimprint lithography (discussed in Section 4.2.4) having many benefits. An interference lithography system can be thought of as an off-axis Michelson interferometer, utilizing the constructive and destructive interaction between two or more beams to expose patterns in photoresist. The

starting laser beam is large for the system used by our collaborators in the Center for High Technology Materials at the University of New Mexico, and, unlike conventional photolithography, there is no need for complex optical components or expensive masks to produce very small structures, on the order of 20 nm [112].

Figure 4-19 shows the interference lithography setup used not only to directly pattern our SiNx/fused silica samples, but also to define templates for subsequent use in nanoimprint lithography on unconventional substrates. A neodymium-doped yttrium aluminum garnet (Nd:YAG) laser, tripled in frequency from 1.06 μm to 355 nm, is the coherent light source, with a pulsed energy of 50 mJ and a 60 Hz repetition rate. A diverging lens expands the beam to 6 inches diameter, such that part of the beam illuminates the wafer and part of the beam is incident on the top mirror and reflected down to the wafer. This creates a standing wave pattern in the regions of overlap of the two beams, provided the overlap distance is shorter than the longitudinal coherence length of the laser. The period of the interference pattern is

$$\Lambda = \frac{\lambda}{2 n \sin \theta} \quad (4-10)$$

where λ is the wavelength of the laser, n is the index of the medium in which it travels to contact the resist, and θ is the incident angle. With a single exposure, one can achieve a 1D periodic pattern; with two exposures, rotating the sample 90° for the second exposure, a 2D square lattice pattern is created. By varying the angles and number of exposures, hexagonal and even chiral materials have been demonstrated. Recently, the same equipment used for our samples was able to pattern helical 3D photonic crystal structures from six exposures with 60° rotations [113], which may lead the way for future photonic crystal-based sensing architectures with another dimension of control.

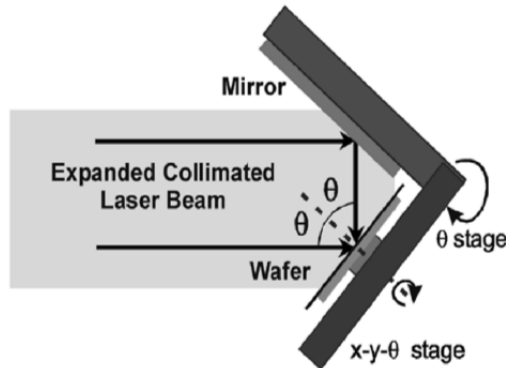


Figure 4-19: Schematic of the interference lithography setup. A 355 nm Nd:YAG laser is incident on the wafer from two directions, creating an interference pattern at the wafer.

The setup in Figure 4-19 was used to define our 2D array of holes over samples as large as 4 inch wafers. First, on top of the PECVD or LPCVD SiNx layer, an anti-reflective coating (Brewer Science, ARC i-CON-16 conformal BARC) to control substrate reflectivity and enhance the critical dimension control was spun on. On top of the anti-reflective layer, positive photoresist was coated. The resist was baked on a hotplate at 90 °C, followed by a double exposure with 90° rotation, using black paper mounted above the wafer when needed to define different size photonic crystal areas. The samples were developed with tetramethylammonium hydroxide developer, then coated with 50 nm of chrome (Cr) at Stanford to serve as a mask for subsequent pattern transfer of the photonic crystal holes. The pattern from the chrome is transferred via an acetone liftoff process, where the exposed sidewalls of the resist pillars allow the posts to be removed, as shown in Figure 4-20.

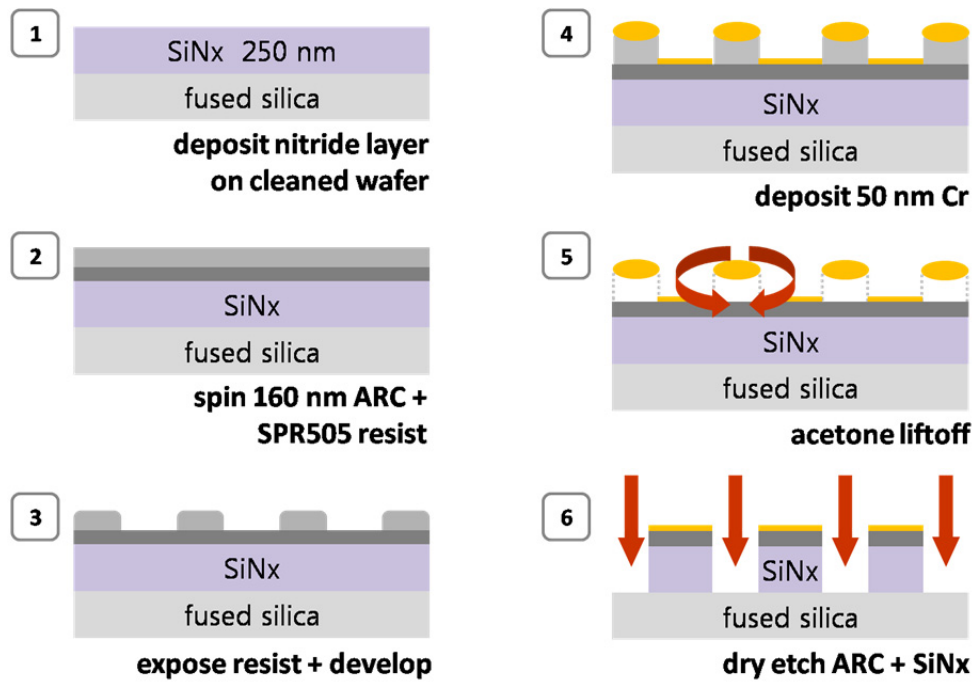


Figure 4-20: Deposition, lithography, and etch process for 2D photonic crystals.

4.2.3 Etching

With the photoresist posts removed via liftoff (shown in Step 5 of Figure 4-20), the Cr mask on the remaining surface (Step 6) defines the areas that are etched: first the anti-reflective coating (ARC) and then the SiNx, with a timed stop on the fused silica. After comparing sidewall roughness from available etch procedures with a variety of fluorine-based chemistries compatible with our entire processing flow, an anisotropic dry etch with NF₃ was used to produce the photonic crystal holes. Both Scanning Electron Microscopy (SEM) and Focused Ion Beam (FIB) tools were employed to help optimize the etch process chemistries and parameters, as illustrated in Figures 4-21 and 4-22. The SEM and FIB analysis also confirmed as-fabricated geometries, uniformity, and the quality of edges and sidewalls. Figure 4-22 depicts cross sections that were filled with platinum (Pt) and then milled to increase contrast.

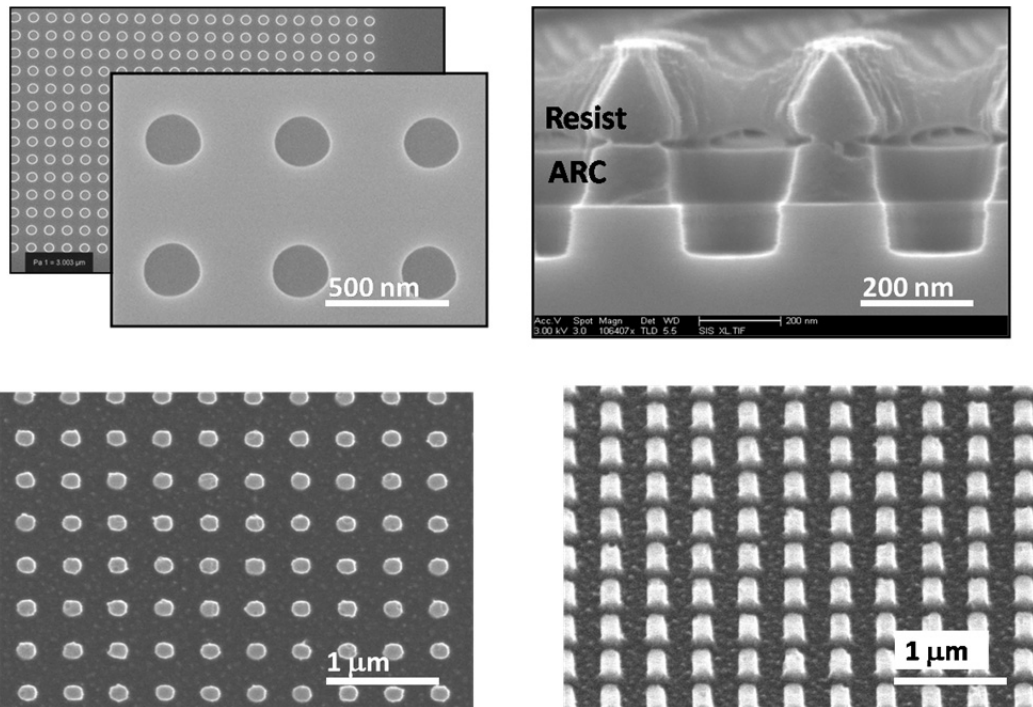


Figure 4-21: Scanning Electron Microscopy (SEM) images after lithography and etching show the SiNx photonic crystals with pitch 500 nm and hole diameters of ~200 nm for resonances in the VIS-NIR.

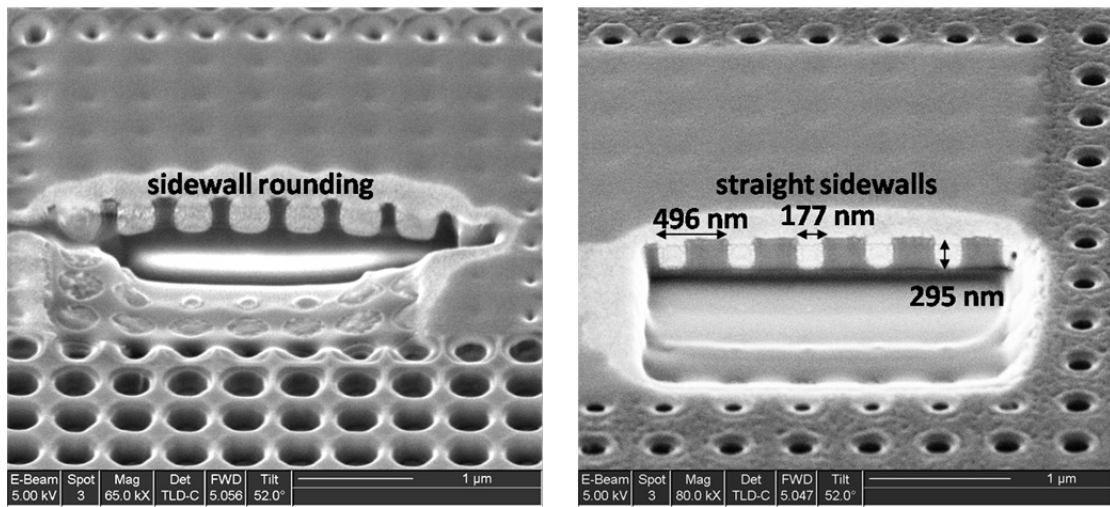


Figure 4-22: SEM images taken immediately after using a Focused Ion Beam (FIB) to fill the photonic crystal holes with Pt and mill trenches. This allowed for high-contrast imaging of the sidewall shapes to improve processing parameters.

With the etch complete, the photonic crystals are cleaned with a descum O₂ plasma and can then progress to any surface treatment or fluid testing, discussed in Section 4.2.5 and 4.2.6. Alternatively, using nanoimprint lithography techniques – which will be described next – the original interference lithography samples can be utilized to create many copies of samples for extensive testing.

4.2.4 Nanoimprint Lithography Alternatives

After creating a “master” template from lithography and etching techniques, one can transfer the master pattern to “son or daughter” samples through nanoimprint lithography. Nanoimprint lithography is a 1:1 embossing or stamping process that can be extremely low-cost, high-resolution (nm-scale feature sizes), and high-throughput, covering an entire wafer [114].

We utilized nanoimprint lithography to pattern large areas (~1.2 cm x 1.2 cm) of 2D photonic crystals for samples resonant at 670 nm. The samples began with SiNx on fused silica substrates, which was then coated with a Cr mask, photoresist, and an imprinting resin comprised of 80% benzylmethacrylate, 10% methacryloxypropyl-terminated polydimethylsiloxane, 5% polybenzylmethacrylate, and 5% trigonox 21ls curing agent. A square or hexagonal periodic lattice of holes was introduced onto the SiNx layer by thermal nanoimprint lithography. The master nanoimprint stamp for 670 nm resonances featured a lattice period of 400 nm and hole radius of 72 nm. Low pressure (25 atm) and low temperature heat (120-130 °C) was applied for 5 minutes, leaving near-zero residue in a simple 4-step process. The imprint mold was removed, and O₂ reactive ion etching using the Cr mask was performed, followed by Cr mask removal.

Such a technique provides a large-area, high-throughput, low-cost process that can accommodate unconventional substrates, which will be of interest in Chapter 6.

4.2.5 Surface Treatment Studies

In addition to the importance of the fabricated geometry in photonic crystal slabs, the surfaces left after processing are of interest. Especially when pushing the limits of detection sensitivity, the affinity binding approaches discussed in Section 2.1 are important to consider as part of the sensor surface design and fabrication. Some of the key parameters of any surface treatment that influence the biosensor performance include the effect of immobilization¹⁴ on the biorecognition element, the surface molecules' orientation (and its effect on affinity), and the effect of variations in surface coverage on the biorecognition elements' capabilities.

While a lengthy investigation of surface chemistries is outside the scope of this thesis, we direct the reader to work in the growing area of surface treatments for biosensors [11, 115-117] and highlight our primary options for surface treatment here. The use of SiNx and fused silica for our all-dielectric photonic crystal allows for glass-like surfaces to utilize effective techniques from biochemistry for attaching a capture layer. Surface treatments such as chemical etching techniques, vapor or plasma deposition, and the formation of self-assembled monolayers (SAMs) are often used to alter a surface's wettability. The resulting hydrophobicity or hydrophilicity of a surface offers insight into the surface's preferred type of binding; hydrophobicity indicates that a surface tends to

¹⁴ I.e., the process by which a biological element is attached. Options include adsorption, entrapment, and covalent bonding.

interact with non-polar functional groups via dispersion, while hydrophobicity indicates polar interaction.

For oxide surfaces such as TiO₂ or SiO₂, the first step is generally to create surface hydroxyl groups that can subsequently be attached to amines, thiols, and carboxylates. For silica-based materials, this often involves silane coupling agents that can either be hydrolyzed to form a silica-based polymeric coating via surface condensation, or reacted with surface silanols (without hydrolysis) to form covalently attached monolayers on the surface. The surface silanols or “grafting” approach is often preferred, as the resulting monolayer promotes high binding efficiency and is less likely than a thick silane layer to negatively affect optical transduction due to absorption.

An example of our SiNx surface treated with Hexamethyldisilazane (HMDS) or CF₃ is shown in Figure 4-23a and Figure 4-23b, respectively. The side view of a water droplet allows for measurement of the contact angles, which are 45° for HMDS-treated SiNx and 104° for CF₃-treated SiNx. These preliminary studies provide some indication of how surface treatments can be used to help engineer the interaction of the analytes at the photonic crystal sensor surface, and raise questions for future work. For example, studies on any optical effects of the surface treatment or an examination of the longevity of the surface coatings could be useful for many applications. These initial studies were completed on SiNx surfaces that had not been patterned with photonic crystals, and thus further investigation on patterned surfaces will provide more insight to the degree of surface engineering possible on our sensors.

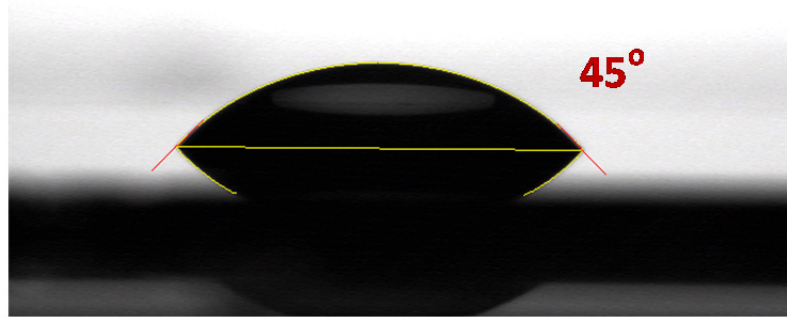
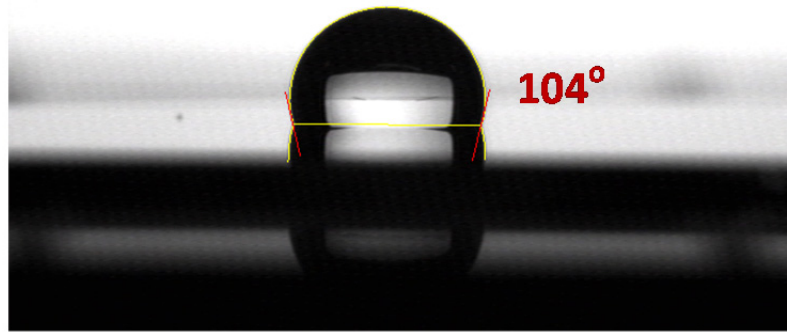
(a) Hexamethyldisilazane (HMDS)**(b) CF₃**

Figure 4-23: Contact angle images for DI water droplets on SiNx surfaces demonstrate the effect of surface treatments on hydrophobicity. Angles of 45° and 104° were measured for the (a) HMDS and (b) CF₃treated samples, respectively.

4.2.6 Fluidic Chamber Construction

The final piece needed to enable characterization of the photonic crystal was the construction of the fluidic chamber such that analytes could flow on top of the photonic crystal slab. The photonic crystal samples were diced (either before patterning or after),

into $\sim 1 \text{ cm} \times 1 \text{ cm}$ pieces. Samples were mounted with adhesive polyimide (Kapton) film and index-matching fluid onto a fused silica interferometry flat with a 30-minute wedge that minimized interference between the fused silica surfaces. A Teflon spacer with an aperture, O-rings, and another fused silica interferometry flat, compressed with cage optomechanical mounts, formed the macrofluidic chamber. Wire-trimmed syringe tips were inserted into the Teflon spacer after a channel was cleared, and polyethylene tubing was used to connect the syringe tips to the incoming and outgoing reservoirs. To prevent leaks, plastic paraffin was layered around the Teflon.

Figure 4-24 illustrates the design of the initial fluidic chamber and the prototype with the photonic crystal in place. This macrofluidic chamber enabled easy delivery of bulk solutions to the photonic crystal surface, with manual flushing of the chamber in between solutions. Integration of the photonic crystal with PDMS-based microfluidic channels that allow for pneumatic controlled valves and pumping action in later prototypes is described in Chapter 5.

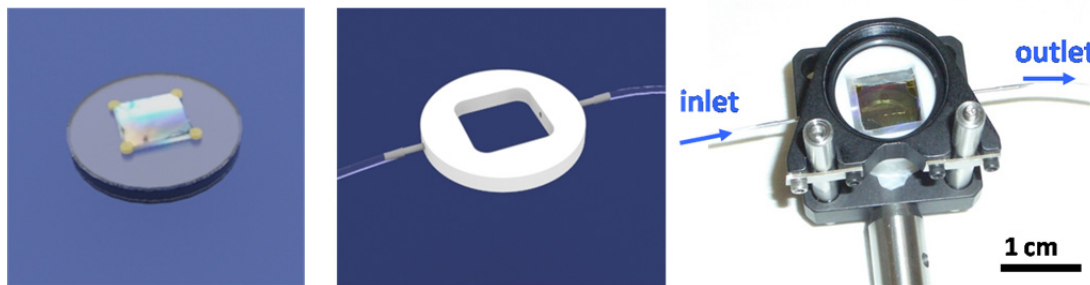


Figure 4-24: Illustration and photograph depicting the design and assembly of a macrofluidic chamber for initial tests with a large $12 \text{ mm} \times 12 \text{ mm}$ photonic crystal slab. Interferometry flats, index-matching fluid, Kapton tape, a Teflon disc, syringe tips, polyethylene tubing and plastic paraffin sealing film are compatible with standard cage optomechanical mounts.

4.3 Photonic Crystal Resonance Characterization

With the fabrication and assembly steps described in Section 4.2 complete, the photonic crystal was characterized with broadband light to confirm that the resonance peaks would overlap with the VCSEL wavelength range. Photonic crystal samples with the macrofluidic channel were first analyzed with a Cary 500 spectrophotometer, pictured in Figure 4-25, with pinholes for limiting the angle of incidence and a polarizer to observe any ellipticity. Although the limited sample chamber size did not allow for additional optical components to further correct the spectrophotometer beam shape, even with a large beam spot (1 mm x 3 mm), the expected dual resonance peaks were clearly observed in both air and aqueous solutions. Figure 4-26 shows the measured reflection vs. wavelength for two different samples in air and water, respectively, falling within the VIS-NIR design range.

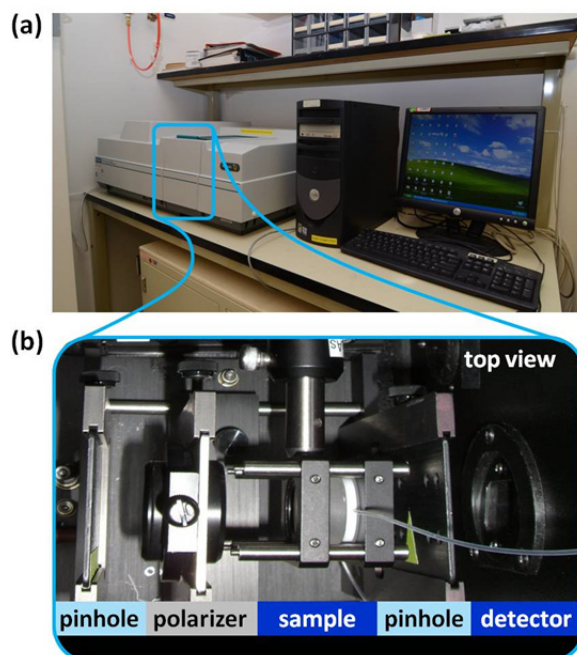


Figure 4-25: (a) Cary 500 spectrophotometer and (b) a top view inside the testing chamber, with photonic crystal and macrofluidic cell.

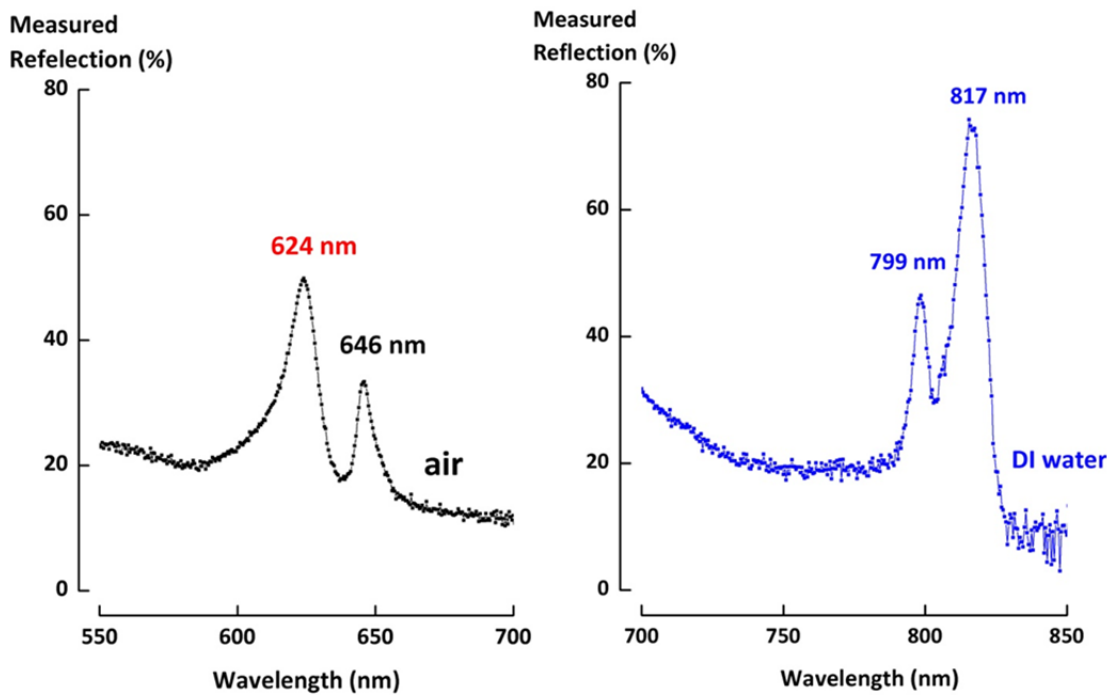


Figure 4-26: Measured reflection spectra from two different photonic crystal samples designed for use with 670 nm VCSELs (left) and 795 or 822 nm VCSELs (right). The sample yielding the 624 nm and 646 nm peaks in air was fabricated with nanoimprint lithography and the lower-wavelength resonance (labeled in red) was later used for aqueous sensing (discussed in Chapter 5).

The sample producing the data on the left was fabricated with nanoimprint lithography and used later for aqueous sensing at 670 nm; the sample producing the data on the right was fabricated with interference lithography and can be used for future integration with 822 nm VCSELs. Comparing the behavior of the photonic crystals in experiment to that predicted by simulation, we see a clear match in peak location and relative spacing between the two resonances, with some variation in peak shape. Figure 4-27 shows the experimental vs. simulation results for a photonic crystal structure with 250 nm diameter holes and a 300 nm etch, tested in air. We hypothesize that the broadening results from off-normal incidence light, as will be discussed further in Chapter 5.

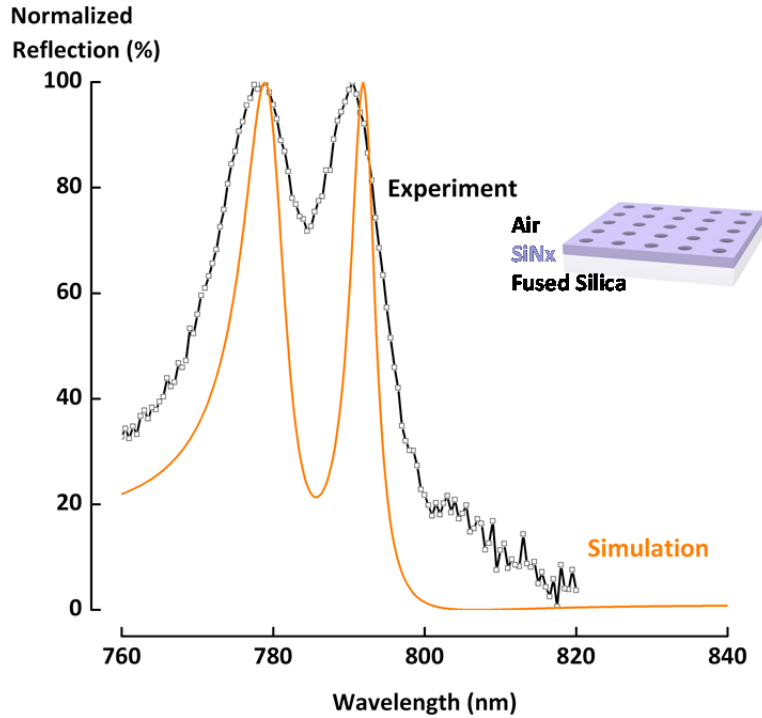


Figure 4-27: Measured normalized reflection for a photonic crystal sample in air matches the peak locations predicted by FDTD simulation. Some broadening is hypothesized to occur from off-normal incidence light, as will be discussed in Chapter 5.

This same photonic crystal sample with DI water produced the spectrum shown in Figure 4-28. One can see that the two peaks have smeared, with only a shoulder left visible in the experimental data (blue). Furthermore, the blended peak has shifted approximately 8 nm from what would be expected with the FDTD simulation. We hypothesize that the non-uniformity of the photonic crystal sample is responsible, as light traveling through DI water will shift due to Snell's Law to probe a slightly different spot on the sample compared to the light traveling through air. As we shall discuss further in Chapter 5, the non-uniformity of the sample as well as the angular-dependent photonic crystal reflection spectra are a concern when implementing our new VCSEL-based detection method, and will require careful design of the measurement system. Based on

the initial spectra measurements, in subsequent experiments, the photonic crystal location was optimized in aqueous solutions before flowing other aqueous solutions to detect refractive index shifts. For example, in Figure 4-29, we measure the same sample used in Figure 4-28, but the beam is incident on a different location. In this case, one can see the two peaks clearly with peak widths of 9.8 nm and 4.4 nm in DI water, corresponding to Qs of 83 and 181, respectively. While this is less than the as-designed Q, it is sufficient for viewing shifts as low as 0.2 nm that would a multi-mode VCSEL linewidth. With improvements in fabrication, in Chapter 5 we will aim to operate with single-mode VCSELs, for increased resolution and better sensitivity. First, however, we characterize the sensor with standard broadband sources and spectrometers.

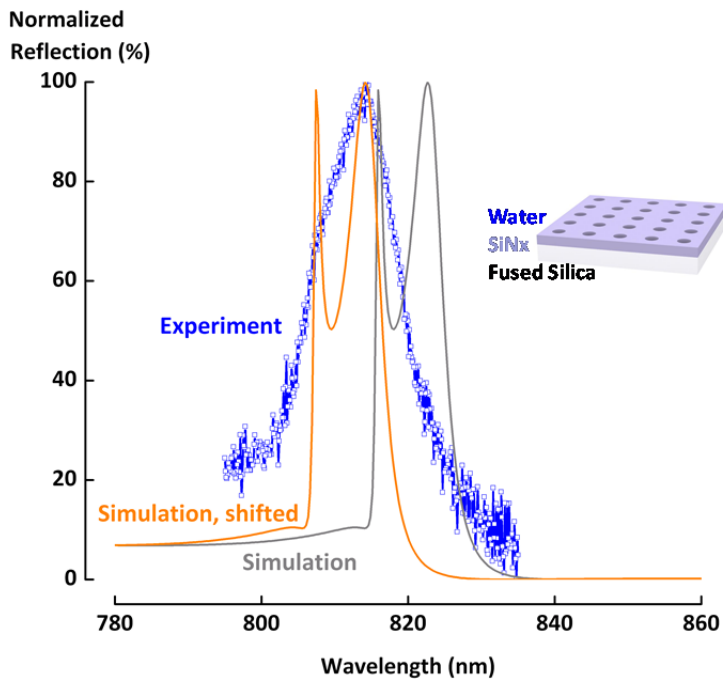


Figure 4-28: Measured normalized reflection for the same photonic crystal sample as shown in Figure 4-27, with DI water compared to FDTD simulations. The photonic crystal probing location was not moved or optimized compared to that used in Figure 4-27 in air, and the non-uniformity likely caused both the blending and 8 nm shift from expected peak values.

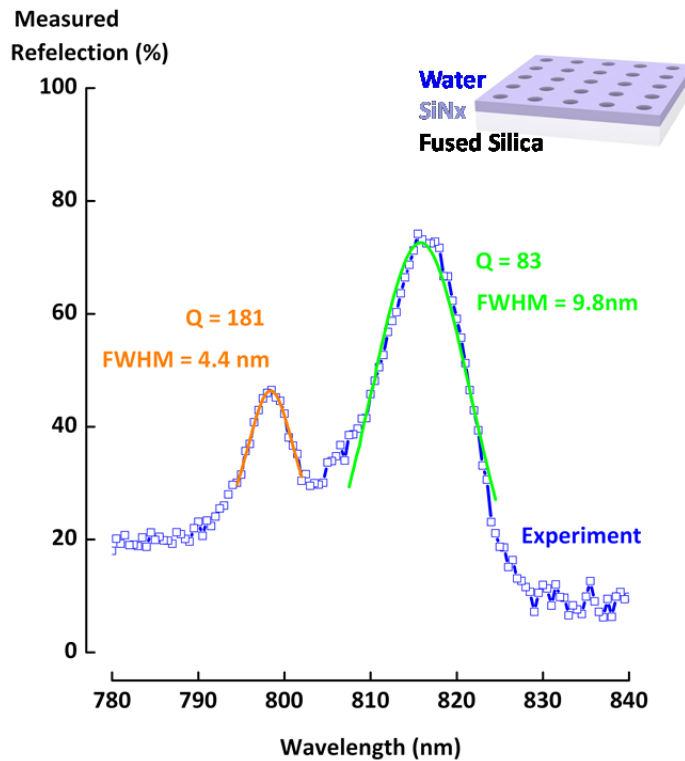


Figure 4-29: Measured normalized reflection for the same photonic crystal sample as shown in Figure 4-27, with DI water. Moderate Qs of 83 and 181 are robust to fabrication defects while providing enhancement for observation of peak-shifting.

In order to evaluate our biosensors' sensitivity with a standard broadband source, we performed transmission and reflection measurements with a series of titrated solutions contacting the photonic crystal sensing surface. The most common ways to measure sensitivity include shifts of spectral features for a given change in refractive index (nm/RIU), changes in intensity for given refractive index changes (dI/RIU), a minimum detectable quantity (ng/ml), and a refractive index limit-of-detection (RIU) for the system as a whole. Despite the blended peaks that resulted when swapping air for DI water without re-optimizing the position of the incident beam on the photonic crystal, we can test the sensitivity of the sensor with bulk solutions and obtain reasonable results with some curve fitting.

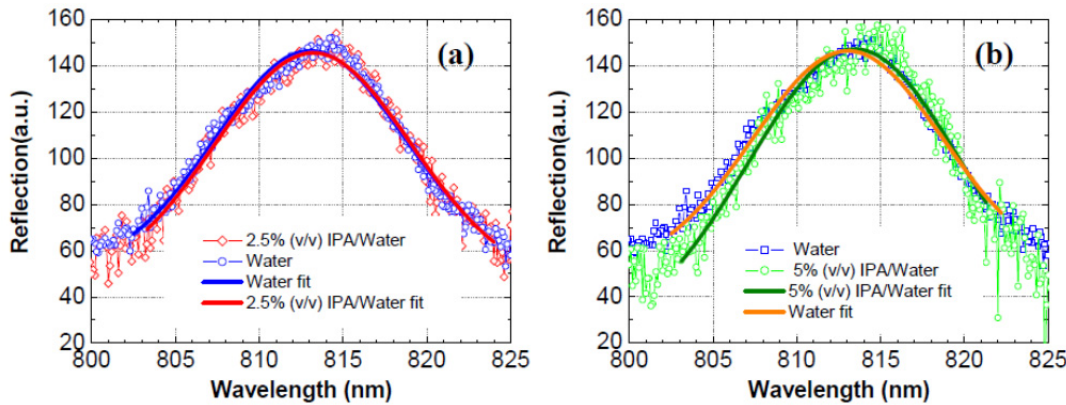


Figure 4-30: Measured normalized reflection for different water and IPA solutions.

With peak fitting, one can differentiate water and 5% IPA solutions clearly, corresponding to a resolved index change of $\sim 1.5 \times 10^{-3}$ RIU.

As shown in Figure 4-30, with the slope of the blended resonance peaks fairly well preserved on the lower and higher wavelengths, we can observe a wavelength shift of 0.2 nm between the spectra for DI water and that of 5% IPA/water. This wavelength shift is in good agreement with our expectations from simulations, resulting in a resolved index change of $\sim 1.5 \times 10^{-3}$ RIU for the initial prototype. This performance reasonably matches the theoretical estimation for this type of sensor, and thus the next step is to replace the bulky broadband light source and spectrum analyzers used here with our more compact and cost-effective VCSELs and detectors.

4.4 Summary

In this chapter we reviewed the fabrication, assembly, and characterization of the TECs, light sources, detectors, photonic crystals, and fluidic components that comprise our label-free sensor. Utilizing a combination of semiconductor processing, optical interference lithography, and soft-lithography techniques, we created low-loss, all-dielectric photonic crystals for the 650-900 nm operating range to be paired with our

desired sources, detectors, and fluidic components. We described the design and construction of an optical test setup and device packaging techniques to measure performance of the TEC/VCSEL/detector module in transmission and reflection, and found ample VCSEL power, but limited single-mode tuning range via current tuning, as expected. We demonstrated more controlled, precise tuning with a miniaturized TEC, with reasonable heating times on the order of ~1 minute for the range desired. Utilizing this information, we created a custom MATLAB interface for characterizing the sensor components in both reflection and transmission. The photonic crystals were initially characterized as part of a system with broadband sources, spectrometers, and a large fluidic reservoir, in preparation for integration with more compact VCSELs, detectors, and microfluidics. Even with highly non-uniform initial samples, experimental sensitivity of 130 nm/RIU was measured, with photonic crystals robust to sidewall roughness and fabrication variations. These components can open a new arena of continuous monitoring in compact, arrayed, and perhaps even implantable format.

Chapter 5

Refractive Index Sensing with Tunable VCSELs

“Great difficulties are felt at first and these cannot be overcome except by starting from experiments.”

- Christiaan Huygens

After testing the photonic crystals with broadband incident light and observing resonances at wavelengths that appear to coincide with our VCSEL target wavelengths, we set out to eliminate the need for bulky spectrometers. One of the primary challenges in repeating the refractive index measurements in Chapter 4 with a VCSEL source instead of a white light source and spectrometer is addressing the non-uniformity and angular dependence of the photonic crystal. Section 5.1 describes an *in situ* characterization setup that was created in order to focus both the white light source and the VCSEL beam onto the same location within the photonic crystal. This enabled verification of the transmission spectrum for a given sampling area of the photonic crystal before employing the tunable TEC/VCSEL/detector to measure a subset of the spectrum point-by-point without a spectrum analyzer.

As Section 5.2 will illustrate, experimental results for label-free sensing with a tuned VCSEL are similar to RCWA-simulated spectral shifts, enabling differentiation of water and IPA/water solutions. However, we will see that to more closely match the theoretical sensitivity, care must be taken to control photonic crystal fabrication to align the photonic crystal optical resonances with the VCSEL single-mode operating regime. Section 5.3 will discuss some of the non-idealities of the measurement system, specifically focusing on the angular-dependent transmission response that makes alignment of the VCSEL and photonic crystal resonance experimentally challenging in a research university setting without tight processing control. Particularly for non-uniform photonic crystal samples where the VCSEL operating range must be extensively tuned to try to overlap the photonic crystal resonance, drift over time is also a concern. In our proof-of-concept sensor system, the manual fluidic handling adds to both the testing time and the possibility of jostling the measurement setup (with forces arising when fluid samples are swapped). Thus, the macrofluidic systems are replaced with integrated microfluidics that are described in Section 5.5 for future sensor demonstrations.

5.1 Testing Setup

At the end of Section 4.3, we saw that the guided resonance peak locations and shape shifted depending on what photonic crystal locations were probed, even for samples made with interference lithography that appeared uniform to the eye (full coverage of the $\sim 1 \text{ cm} \times 1 \text{ cm}$ sample). This issue was revisited when designing the VCSEL test setup, since the most interesting wavelength for multi-modality sensing was 670 nm (as discussed in Chapter 2). The photonic crystal samples we had processed to be resonant at 670 nm were made with nanoimprint lithography; unfortunately, the template for 144

nm holes and 400 nm pitch square lattice photonic crystals, resonant at ~670 nm, was damaged. As shown in Figure 5-1, while the nanoimprint lithography technique is able to produce well-controlled, large area patterns, the resulting photonic crystal sample coverage can vary. Nevertheless, the incomplete coverage of a 12 mm x 12 mm sample still provided some areas of high quality photonic crystals that were larger than what could be easily realized with other methods like e-beam lithography at the time, and hence these samples, when carefully probed, could be used for a proof-of-concept testing with our TEC/VCSEL/detector modules.

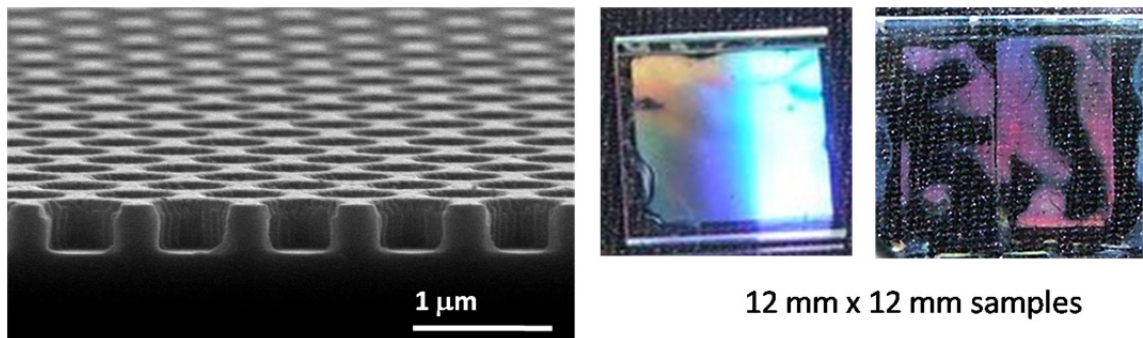


Figure 5-1: Scanning Electron Microscopy (SEM) image and photographs of photonic crystal samples made via nanoimprint lithography. For the photographs on the right, black fabric is placed behind the clear plastic sample container to provide contrast. While local patterning is transferred with high fidelity, the original master quality and adhesion issues can limit the patterned area of samples. Our sample with 144 nm holes on a 400 nm lattice (far right) was utilized for sensing even though it had large unpatterned voids, as it was resonant at wavelengths that corresponded to 670 nm VCSELs.

The photonic crystal sample non-uniformity problem is further illustrated in Figure 5-2. The reflectivity spectra highlight the fairly rapid change in the guided resonance peak quality, location, and shape that resulted from moving the beam ~500 μm at a time around the sample area experimentally mapped to be most likely to produce sharp resonances.

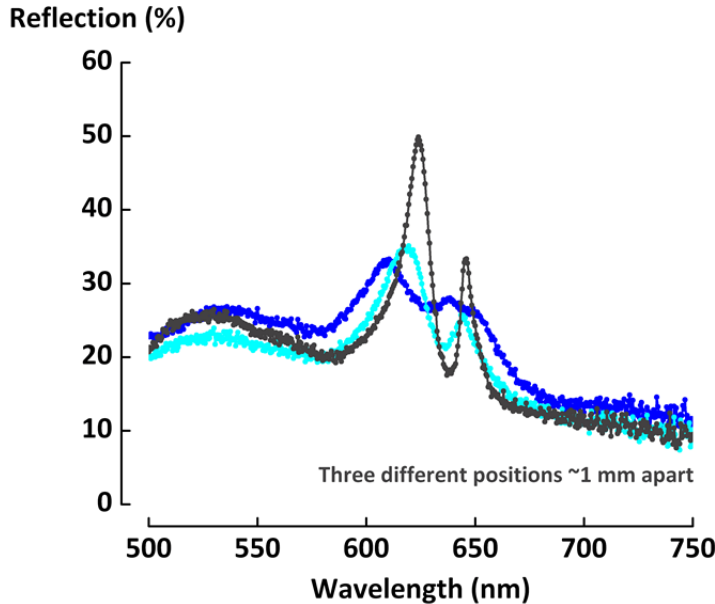


Figure 5-2: Non-uniformity of a photonic crystal made with nanoimprint lithography results in different reflection spectra. These curves were taken at locations ~1 mm apart.

This sample non-uniformity, combined with the angular dependence of the photonic crystal, necessitated a laboratory setup where we could examine the broadband characterization of the photonic crystal guided resonances *in situ* to verify that the VCSEL tuning wavelength coincided with the photonic crystal resonance peak (allowing us to replace the bulky broadband source and spectrometers used in Section 4.3 with an integrated TEC/VCSEL/detector). Such a setup was constructed and is depicted in Figure 5-3. A fiber-coupled QTH lamp was directed with a flip mirror through a pair of achromatic lenses, using 1:1 imaging to illuminate a spot on the photonic crystal sample. The transmitted light entered a fiber coupler to route the signal to our spectrum analyzer, allowing us to verify the photonic crystal broadband behavior prior to probing the crystal with a VCSEL.

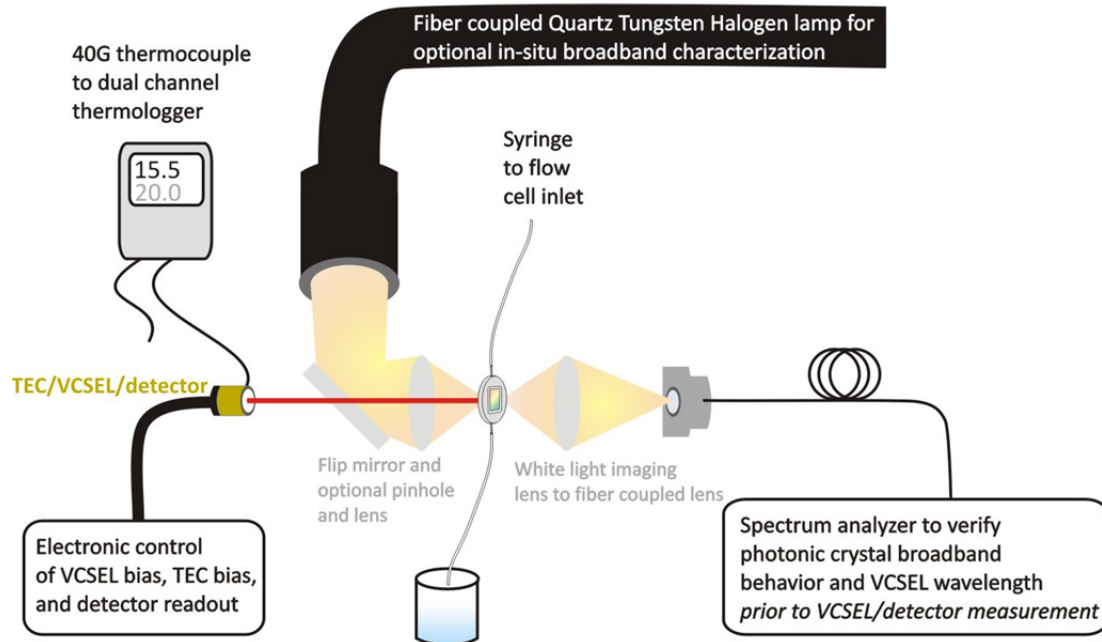


Figure 5-3: Schematic of the measurement system used to co-align the broadband light source with the VCSEL to probe the same location on the photonic crystal.

With the QTH lamp turned off and the flip mirror positioned out of the VCSEL beam path, the spectrum analyzer or a handheld spectrometer could be used to verify the VCSEL lasing wavelength for various temperature and current biasing conditions. With both of the photonic crystal resonance and the VCSEL lasing wavelength measurements falling in the same range, we could proceed to illuminate the photonic crystal with the TEC/VCSEL/detector module, provided the beams were aligned using the flip mirror, to measure a subset of the spectrum point-by-point without the spectrum analyzer. Pinholes, not pictured in the figure, were utilized for limiting the angle of incidence onto the photonic crystal slab, but the white light signal in particular was weak, limiting the size of pinhole that was practical to $\sim 800 \mu\text{m}$. This resulted in an approximately 1.5 mm

diameter spot on the photonic crystal, and hence the spectra shown average the non-uniformities of that size region. A 40 gauge precision thermocouple monitored the TEC/VCSEL/detector module, in addition to recording the ambient temperature, as in the characterization measurements described in Chapter 4. For these measurements, our macrofluidic cell was utilized along with manual syringe delivery. The electronic controls used were the same as described in Section 4.1.2 and Figure 4-7, with a custom MATLAB interface and GPIB protocols.

5.2 Bulk Sensing Results

The results from the *in situ* measurement are shown in Figure 5-4. The photonic crystal spectrum in air (black) and the spectrum in DI water (blue) collected by the spectrometer show peaks at 615 and 642 nm for air, and 657 and 680 nm for DI water. This corresponds to a 132 nm/RIU shift, which matches what was anticipated from simulations. The nominal VCSEL wavelength roughly aligns with the midpoint of the deepest resonance for the photonic crystal in DI water; however, since shifting the incident light beam to different locations on the photonic crystal changes the resonance spectrum due to the nanoimprint lithography non-uniformities (Figure 5-2), we anticipated difficulty in aligning the VCSEL resonance with the photonic crystal resonance in practice.

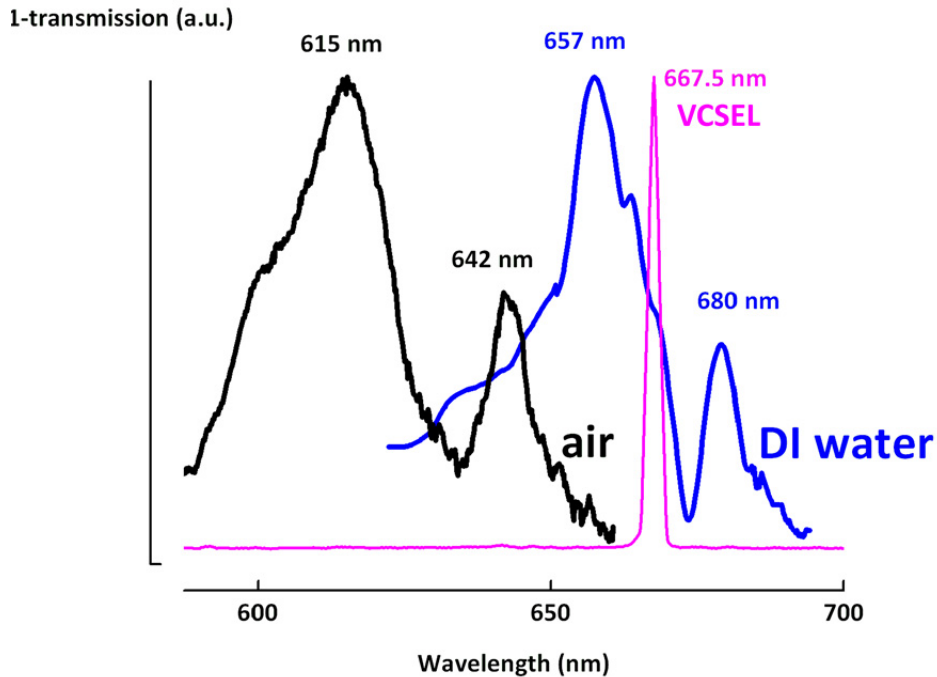


Figure 5-4: *In situ* characterization of the photonic crystal slab in air (black) and DI water (blue) shows a shift of 132 nm/RIU. The photonic crystal resonance in aqueous solutions appears to align with the VCSEL wavelength (pink).

For the refractive index sensing with this sample utilizing VCSELs, solutions of DI water and IPA were prepared in the same manner as described in Chapter 4. VCSEL and ambient temperatures were recorded 12 times per second, and the TEC current was swept to cool or heat the VCSEL at different current biases, pausing to allow for heating transients to pass. At each TEC and VCSEL bias combination, the transmitted photonic crystal intensity was recorded at least 15 times and averaged. Figure 5-5 shows the VCSEL's normalized transmitted intensity through the photonic crystal slab, plotted as reflection (where reflection and transmission are assumed to add to unity). This was measured by a calibrated Newport 1830-C optical power meter for pure DI water, 1%, 10% and 50% (v/v) IPA, for biasing combinations that aimed to maintain single-mode FWHM linewidths on the order of 0.08 nm.

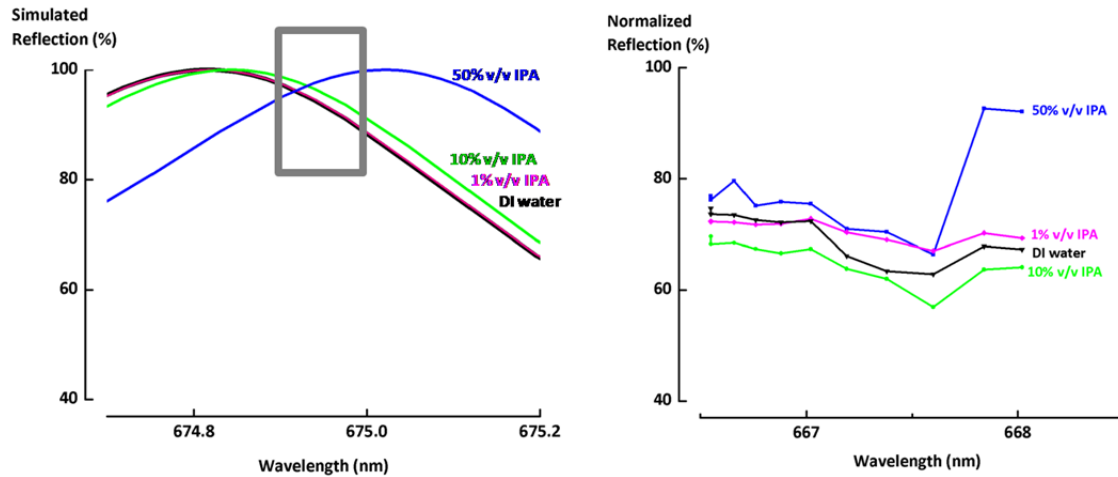


Figure 5-5: Simulated reflection for the photonic crystal with four solutions of DI water/IPA (left), compared with experimental results for normalized reflection utilizing a VCSEL source. We see 25% change in transmission between DI water and 50% IPA, corresponding to $\sim 10^{-4}$ RIU detection.

We hypothesize that we are measuring the region in the grey box highlighted in the simulation, with a $\sim 25\%$ change in intensity visible between 50% v/v IPA and DI water. Some drift is thought to occur around the 10% IPA (green) curve, as the entire test took over 30 minutes per solution; this can be remedied by integrating fluidic functionality (discussed in Section 5.5). To more completely trace the photonic crystal resonance curve, the VCSEL tuning would need to be extended further, well past the onset of multi-mode operation. The index sensing results thus highlight the importance of fabrication control in the photonic crystal, in order to more accurately align the VCSEL tuning range with the guided resonance. Still, the large observed 25% change in transmission corresponds to a $\sim 10^{-4}$ RIU detectable index change, assuming 1-2% change in VCSEL intensity can be resolved, and moderate single-mode linewidth. This has been shown to translate to biologically-relevant concentrations of 2.5 nM of streptavidin in

recent studies [69]. The photonic crystal 132 nm/RIU measured shift corresponds to a $\sim 7e^{-6}$ RIU limit for picometer linewidths and $\sim 1\text{-}2\%$ minimum detectable intensity based on the noise measured in Section 4.1.

Since the photonic crystal resonance and limited VCSEL tuning range did not seem to align optimally for the differentiation of the lower concentration IPA solutions, we examined the consequences of foregoing single-mode operation (which would provide the best wavelength resolution) to expand the tuning range. Tracing out more points of the reflection spectra could help to ensure that the sensing is performed at the peak and point of highest slope. Figure 5-6 illustrates the effect of extending the VCSEL tuning range. This behavior is expected, based on the VCSEL characterization measurements discussed in Chapter 4. If we only swept the current that biased the VCSEL, without activating the TEC, we spanned a limited 1.1 nm tuning range, denoted in grey. In this regime, we observed 0.35 nm/mA shifts in lasing wavelength. Temperature tuning provided an additional ~ 0.05 nm/ $^{\circ}\text{C}$.

Cooling the VCSEL, one obtains typical spectra like that shown in the blue box, taken for a 2 mA VCSEL current and 150 mA reverse TEC bias. The FWHM linewidth is less than 0.08 nm for this measurement, limited by the OSA resolution. The side mode suppression of 35 dB provides a high quality beam. In comparison, the spectrum highlighted in the orange box was taken for a maximum operating current (5 mA) and 150 mA TEC bias. Even for typical oxide apertures of less than 6 μm in diameter, the VCSEL FWHM increases with current bias due to the appearance of additional transverse modes at high bias current. The spectrum is clearly multi-mode, albeit with 10 dB side mode suppression, and shows a FWHM of 0.05 nm, providing resolution ~ 6 times worse than what one can achieve with single-mode operation.

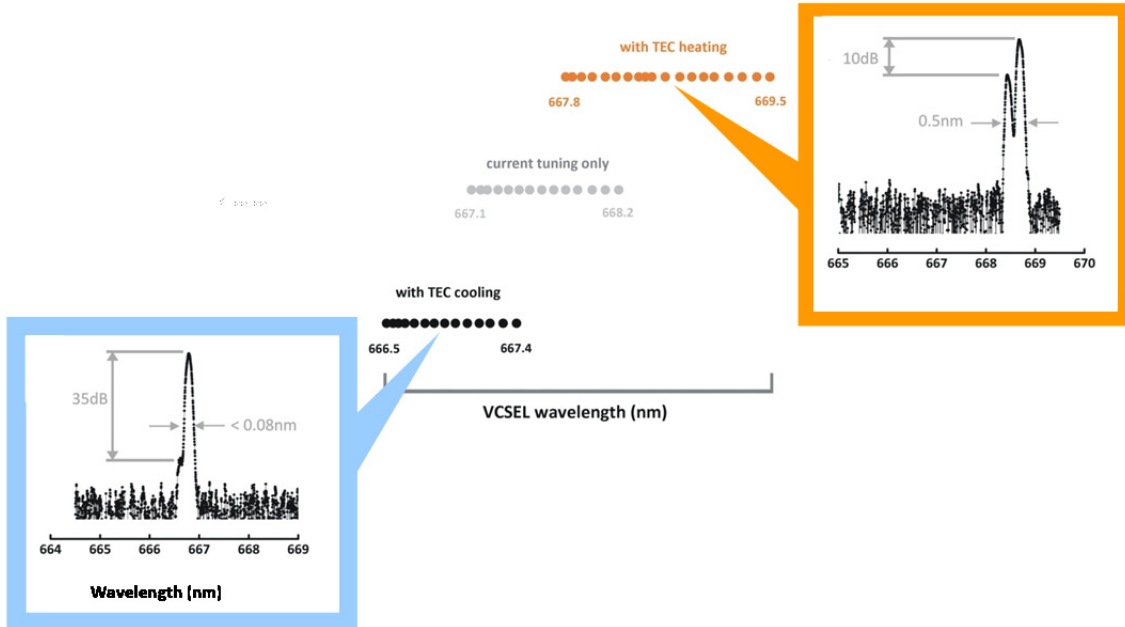


Figure 5-6: Extended tuning range of the 670 nm VCSEL, compiled from Lorentzian fits of OSA spectra for different temperature (TEC bias) and current biasing conditions. Single-mode operation provides less than 0.08nm FWHM linewidth for precise control of wavelength, and transverse multi-mode operation yields ~0.5 nm FWHM linewidth. The total tuning range with a combination of temperature and current tuning is 3 nm. To generate the graph in the center, temperatures ranged from ~8 °C to ~50 °C, corresponding to four TEC bias points of -350 mA (black), 0 mA (grey), 150 mA, and 275 mA (both orange).

The VCSELs were operated from approximately 10% above threshold (thresholds ranged from 1.5-3 mA, depending on operating temperature) to a maximum operating current of 5 mA. In order to maintain output powers of at least 10% of the maximum, the selected tuning range combining both VCSEL bias and TEC bias spans 3 nm (666.5-669.5 nm). The intensity as a function of wavelength for the bias conditions ranges from 0.2 mA to 2 mA for the data in Figure 5-6, and this offset from wavelength to wavelength is normalized when viewing the photonic crystal reflection spectra.

The resulting extended 3 nm tuning range still represents a small portion of the peak to valley resonance curve that we aim to interrogate, due to the broadening of the photonic crystal resonance. Nevertheless, the data shows that with some tradeoff of spectral sensitivity (~6x), even with misaligned resonances and a limited VCSEL tuning range, one can employ a combination of VCSEL current tuning and TEC temperature tuning to extend the overlap in hopes of better differentiating analyte solutions. Alternatively, and with less impact on the system performance, more precise fabrication of the photonic crystals to produce a linewidth matching the VCSEL range will enable more sensitive detection.

Before discussing some of the non-idealities, namely the angular dependence of the photonic crystal, that made the alignment experimentally challenging, it is useful to note results from testing the repeatability of VCSEL wavelength. For each of the data points in the center graph of Figure 5-6, the lasing output for a given VCSEL current bias and TEC bias were recorded during separate tests with various optical coupling schemes and acquisition parameters. Varying the VCSEL bias in steps of 0.25 mA (for VCSELs with a 5 mA maximum current) and varying the TEC current in bias steps of 25 mA (where the TEC was rated to withstand up to 1000 mA maximum current, but tests were limited to 300 mA to maintain adequate laser power), the wavelength was consistently repeatable to within the OSA measurement resolution of 0.08 nm. Coherence length measurements via interferometry are consistent with the linewidth of these lasers being on the order of picometers, which presents an opportunity for very precise tuning to trace portions of spectra without the need for a bulky OSA and broadband source.

5.3 Off-Normal Incidence and Drift in Realistic Systems

In addition to the wavelength and intensity precision challenges mentioned, in realistic systems, even a VCSEL that is considered highly directional has a finite divergence angle that should be taken into account when designing the packaged sensor. The simulations shown in previous sections generally assumed an ideal plane wave light source impinging the sample at normal incidence. In Section 3.3, we noted that off-normal incidence calculations with a transfer matrix technique showed that for +/- 2°, which is reasonably achieved in a laboratory setting with collimating optics, the slope of interest for the guided resonance is maintained. However, many biosensors today actually use white light sources or LEDs and optical spectrum analyzers, where the uncorrected beam divergence can easily be 30° half-angle.

VCSELs provide a more compact, efficient, and directional source, with a typical half-angle divergence angle of 7.5°. This angle is still significantly larger than the 2° assumed in initial studies in Section 3.3; thus, to determine the critical design parameters for collimating optics, we investigated the angular dependence more closely. While our 2D photonic crystal slab features a TE-like and a TM-like resonance mode, with both modes being excited by normal incidence light due to symmetry, at off-normal incidence, the loss of symmetry complicates the transmission spectrum. To examine this, a nominal design structure using SiNx and fused silica with a 500 nm pitch, 100 nm radius holes, and a slab thickness and hole etch depth of 250 nm, producing two guided resonances around 800 nm, was employed. As shown in Figure 5-7, numerous high-Q resonances appear as we increase the incident angle. The simulated reflection spectra for 0°, 1°, 2°, and 4°, 7.5°, and 9° are shown in Figures 5-7a and 5-7b. Half angles of 7.5-9° would correspond to the divergence of a typical VCSEL, if left uncorrected by collimating lenses.

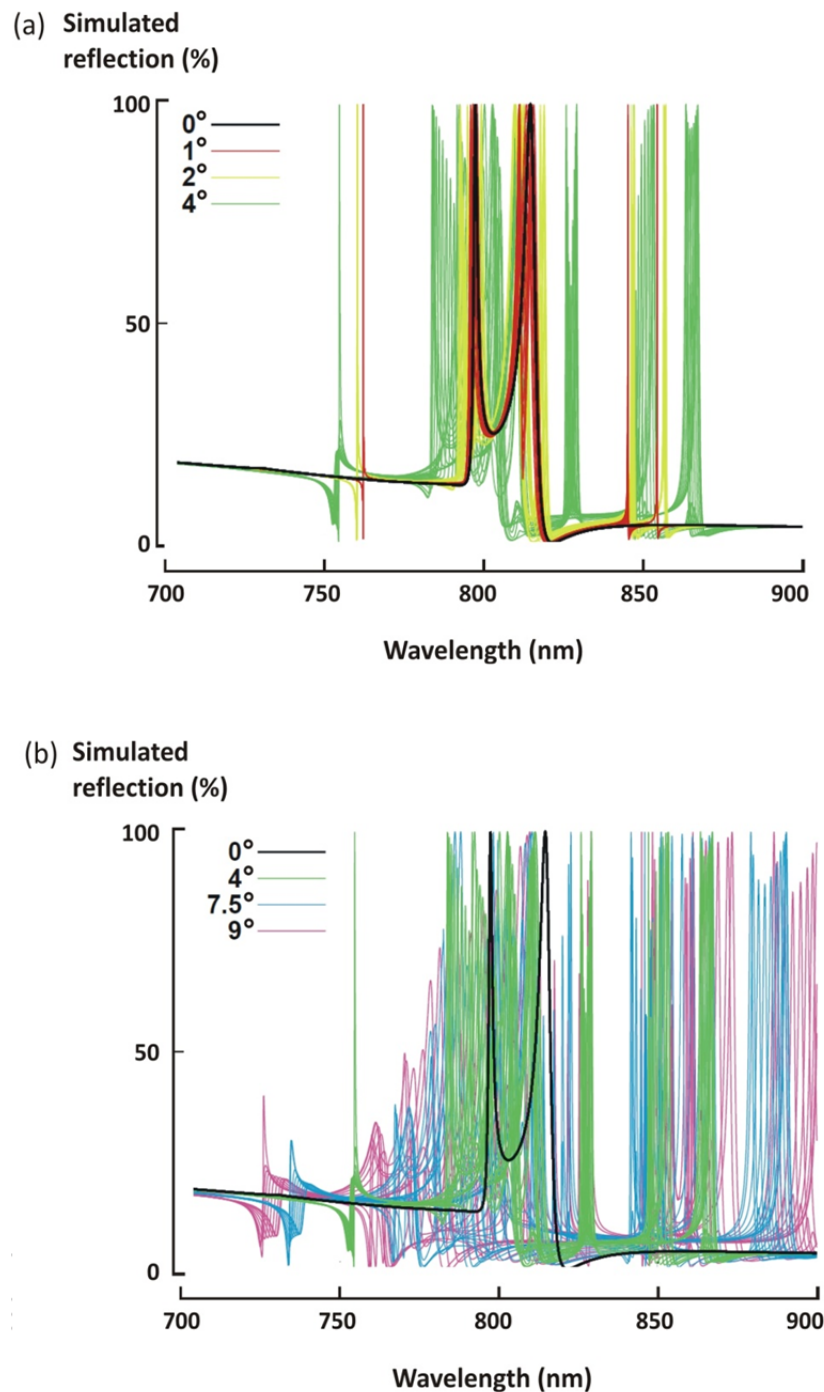


Figure 5-7: Reflection spectra for a photonic crystal design with two guided resonant modes at ~ 800 nm shown for (a) normal incidence, 1° , 2° , and 4° , and (b) normal incidence, 4° , 7.5° , and 9° .

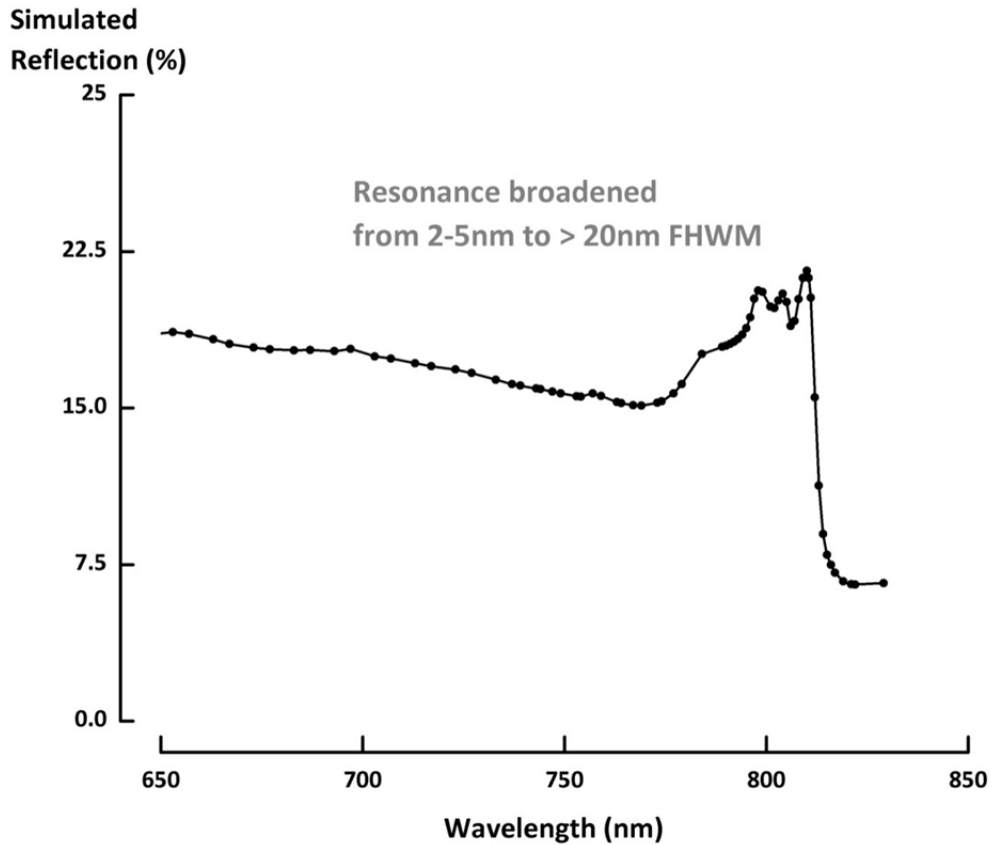


Figure 5-8: Simulated photonic crystal spectral response for an incoming source beam with a finite divergence angle of 7.5° $1/e^2$ half width. The VCSEL incident beam is approximated by a superposition of plane waves at different incidence angles, with a Gaussian amplitude distribution with respect to the angle from normal incidence. The reflection spectra were numerically integrated up to a maximum full angular width of 15° at each wavelength and summed over equal amplitudes of both polarizations.

In Figure 5-8, we utilize these plane wave results at different incoming angles and polarizations to further model the spectral response for a beam with a finite divergence angle. The VCSEL incident beam is approximated by a superposition of plane waves at different incident angles, with a Gaussian amplitude distribution with respect to the angle from normal incidence. The reflection spectra were numerically integrated up to a maximum full angular width of 15° at each wavelength and summed over equal

amplitudes for both polarizations. We note the resonance has broadened from a FWHM of 2-5 nm to a broad peak with FWHM greater than 20 nm. While this simplistic model is not a full representation of the actual beam, especially in the case of polarization-controlled VCSELs, it demonstrates the broadening of the spectral features for a “worst case” scenario where both polarizations are present in equal parts over the uncorrected divergence of a typical VCSEL. In this scenario, the angular dependence has destroyed many of the sharp reflection peaks and reduced the signal contrast from nearly 0-100% reflectivity to only 8-23%. These quantifications enable the practical design and packaging of sensors, with new insight into the specifications for any micro-array collimation optics that will alleviate this non-ideal behavior.

As noted in Chapter 2, VCSEL polarization can be controlled through the addition of slits or other structures [95, 96]. Moreover, for single-mode lasers such as those used in this dissertation, a VCSEL tends to lase in one mode when operated within a narrow tuning range. Thus, the scenario in Figure 5-8 provides an upper bound to the anticipated spreading of the guided resonance, and in experiment, it is reasonable that we would see sharper peaks even without additional collimating optics.

5.4 Label-free Optical Biosensor Comparison

While the initial measured sensitivity reported here in simulation (Section 3.3) as well as experiment (Section 5.2) is less than the best reported performance of other label-free sensors, the utilization of VCSELs, integrated detectors, and all-dielectric photonic crystal slabs for this platform still has several advantages due to its compact size, scalability, thermal behavior, and cost-effectiveness. To further illustrate these tradeoffs, we include a comparison of this work with other optical label-free sensor results published in literature in Table 5-1.

	SPR	Waveguides/ Resonators	VCSELs [27, 28]	VCSELs [29]	This Work
Operating Wavelength	Typically ~1550 nm /swept	Typically ~1550 nm or broadband	850 nm	790 nm	670 nm
Limit-of-Detection (RIU)	10^{-4} - 10^{-9} [64, 71]	10^{-4} - 10^{-8} bulk [118-120]; 7×10^{-9} [121]	$< 5 \times 10^{-3}$	—	10^{-4} bulk index; $7e^{-6}$ if picometer FWHM
Thermal Dependence (Resonator)	Angle sensitive to 0.027 K at 632 nm [122, 123]	Typical $\sim 10^{-5}$ - 10^{-4} RIU/K. 0.3 pm/K achieved on-chip (SiNx/silica) [124]	—	—	SiNx/silica, mini TEC, 3D chip well-suited for compensation
Signal-to-Noise	2000 S/N for protein binding [125]	Noise equivalent detection limit $3.8e^{-8}$ RIU[121]	—	Wavelength stability 0.02 nm (minutes), 0.06 nm accuracy Intensity, detector noise not reported	<1% intensity variation (hours), 0.03 nm wavelength control. Detector noise (I_{dark}) 5.0 pA/mm^2
Size	Sensor surface can be <1 mm x 1 mm Systems typically > 10 cm in each dimension	Resonators/waveguides typically a few μm , but lasers many cm	"Benchtop" system with 2 detectors, beam splitter, lenses	Wavelength meter: 15 cm x 12 cm x 4.6 cm "Benchtop" system	1 cm^3 system packaged. ¹⁵ Unpackaged components: 2.5 mm x 3.2 mm x ~ 3 mm ¹⁶
Weight	package dependent (external lasers /spectrometers can be 10s of kg)	—	—	—	< 3 grams ¹⁷
Estimated scaled costs¹⁸	Tunable lasers and/or mechanics for tunable angle: \$100; position sensor for [64]	Resonators : <\$1 External lasers, broadband sources: ~50-~\$50 000	VCSELs: <\$1 grating/fluidics: $\sim \$1$	TECs/VCSELs: $\sim \$1$ - $\$10$, wavelength meter/readout: $\sim \$50$, grating/fluidics: $\sim \$1$	TEC/VCSEL/detector (integrated)/control/readout: $\sim \$1$ - $\$10$ Photonic crystal, microfluidics: $\sim \$1$
+ bulk detectors, optics, hardware: $\sim \$100+$					
Coupling	Needs prism/grating coupler; off-normal incidence	Often delicate alignment, typically bulky external source	Expansion/collimation lenses, beam splitter	Pair of beam splitters, polarizer, prisms	Simple normal incidence free space or microlenses

Table 5-1: Comparison of optical label-free sensor performance.

¹⁵ This includes the temperature-tunable source (and hence TEC), detector, photonic crystal resonator, PDMS fluidics, TO-5 header, and cap packaging.

¹⁶ The smallest unpackaged prototype without microfluidics includes the TEC (2.5 mm x 3.2 mm x 1.4 mm), VCSEL/detector die (1 mm x 1 mm x 500 μm), photonic crystal (smallest sample cut to 2 mm x 3 mm x 500 μm , but the resonance can be excited by only $\sim 100 \mu\text{m} \times 100 \mu\text{m}$).

¹⁷ The effect of readout electronics/cables and power source is omitted, but the PCB that represents the next step towards wireless operation is included in this weight.

¹⁸ These cost estimates assume the purchase or fabrication of components in bulk for those elements that can be mass-manufactured today (e.g., VCSELs, silicon waveguides/ring resonators).

The choice of sensor wavelength is important, as it can impact the range of possible biomedical applications. The benefits of operating our devices in the 650-900 nm biological transparency window (particularly at 670 nm) have been discussed previously in Chapter 2. In addition, Table 5-1 draws attention to the size, weight, and cost advantages of VCSEL-based sensing compared to approaches that rely on external light sources, spectrometers, and the complex components often required for the alignment of benchtop-style systems. SPR-based sensors, since they take advantage of materials properties at the sensor/analyte interface, have a minimum sensor surface size that can be smaller than photonic crystal-based designs. SPR sensors were, as mentioned in Chapter 2, the first label-free optical sensors commercialized, and have been implemented with various flavors [11, 64, 71, 126]. However, the need for precise coupling and readout hardware makes the implementation of SPR for low-cost handheld applications quite challenging.

In contrast, the benefit of normal-incidence coupling has been described in Chapter 3, with a more critical analysis of just how close to normal-incidence our probing light source must be in Chapter 5. Fortunately, the allowable angle tolerance found in this work is achievable with modern manufacturing techniques, and simple, cost-effective micro-optics arrays can shape VCSEL beams to provide adequate near-normal-incidence performance. Interestingly, one could imagine designing a micro-optics array layer to collimate some of the VCSELs for normal incidence, but intentionally steer other VCSEL beams to hit the photonic crystal at off-normal incidence. This could serve as a means for calibrating the VCSEL-to-photonic-crystal alignment in packaged systems. In addition, using micro-optics to control the VCSEL's angle of incidence onto the photonic crystal enables the active “selection” of the photonic crystal optical resonance behavior that the user desires at a given time, providing yet another degree of tunability with a single device.

Our signal-to-noise and detection sensitivity have been examined throughout Chapters 3-5. With dark current measured to be 5.0 pA/mm², signals in the reflection configuration on the order of nA, and signals in the transmission configuration near 1000 nA, ample SNR is noted for photonic crystal samples in air. Characterization of SNR in fluids needs to be completed, but since we operate in the low absorption window, we anticipate adequate signal. Moreover, the incremental wavelength control for our measurement setup, or spectral resolution, was found to be ~0.03 nm, limited by the ability to control the temperature at the VCSEL die to ~0.5 °C. With the addition of a feedback loop, the temperature control could be improved. Still, 0.03 nm wavelength resolution is better than many spectrometers, and the VCSEL/detector offers a much more compact implementation. In addition to characterizing the sensor's spectral noise, we quantified the amplitude noise. The measurements presented show a < 1% peak-to-peak variation of VCSEL intensity over the course of hours, and repeatable intensity for a given biasing condition.

Thus, we anticipate with more stringent fabrication of photonic crystal resonators and more careful control of angle of incidence during sensor assembly, the VCSEL and photonic crystal slab platform can capture the information gleaned from traditionally bulky spectrometers in a much smaller footprint. The sensor limit-of-detection is estimated at 10⁻⁴ from simulations and experiment, based on designs that have moderate Qs and shifts of ~130 nm/RIU. Higher Q designs have been demonstrated, but since the experimental limitation is currently the alignment of the photonic crystal resonance with a limited VCSEL tuning range, the low-Q structures help us to experimentally align the wavelength ranges.

From engineering both Q and the mode profile, there have been considerable efforts in literature concentrated on pushing the limit-of-detection with the above systems, with selected approaches highlighted in Section 2.4 as well as Table 5-1. For example, recent work on capillary-based optofluidic ring resonators shows a bulk sensitivity of 570 nm/RIU and a measured changed of 2.8×10^{-7} RIU (noise equivalent detection limit of 3.8×10^{-8} RIU). This enables the detection of 10 nM biotin (1.6 pg/mm²). However, the demonstration relied on an external tunable laser coupled laterally to the resonator, adding to the cost and complexity of the system. Moreover, the ring resonator had to be placed in an isolated, thermally controlled copper chamber, highlighting the challenge of temperature sensitivity and drift. The following section discusses the challenges of resonator temperature dependence in further detail and outlines key thermal compensation approaches useful for optical label-free sensors.

5.4.1 Temperature Sensitivity and Drift

We note in Table 5-1 that many commonly used waveguide materials and liquid samples of interest for label-free optical sensing have thermo-optic coefficients with magnitudes $\sim 10^{-5}\text{-}10^{-4}$ RIU/K. Hence, for sensors where detection limits are often designed to be $\sim 10^{-4}$ RIU or less, temperature sensitivity and susceptibility for thermal drift are important aspects of device design and material choice. Active temperature control, athermal device design, and on-chip referencing for drift control have been employed by various groups to help address this issue.

Active control is generally achieved with Peltier coolers, and is necessary for applications that measure chemical reaction rates where the rate constants are temperature dependent. In this work, since we employ a miniature TEC for VCSEL

tuning, we can already monitor and engineer the sensor environment to some extent without adding further complexity. As reported in Chapter 4, we recorded the temperature at the VCSEL die and ambient air, with the thinnest (40 gauge) insulated precision thermocouple available and a meter with accuracy of +/- 0.1 °C. With this configuration, noise was observed to be < ~0.5 °C. Furthermore, the VCSEL light impinging on the sample did not generate a measurable increase in the photonic crystal slab surface temperature. This is as expected, since our photonic crystal slab design consists of all-dielectric SiNx on fused silica and the powers used are generally < 1 mW. While the experiments thus far simply controlled the TEC and monitored the temperature, a feedback loop in future designs would allow for automatic temperature compensation.

Athermal sensing approaches take advantage of the different polarity thermo-optic coefficients of liquid samples and solid sensing surfaces. For example, water has a coefficient of -10^{-4} RIU/K, whereas SiNx and oxides have a positive value of 10^{-5} RIU/K. By engineering the light intensity that is confined in each material, the temperature dependence of refractive index can be compensated. The primary drawbacks to this approach are the limitation of the analyte delivery fluids (to those with certain thermal properties), and the fact that athermal designs are usually very sensitive to fabrication variations. It is useful to note that the athermal sensing approach is not a valid technique for polymer resonators and waveguides because the thermo-optic coefficient of polymers and many delivery liquids are of the same polarity.

The third approach to thermal drift compensation is the use of on-chip references; this requires multiple sensors on the same substrate to make differential measurements. Fortunately for our label-free sensor design, the array-based 3D layered integration of

surfaces, sources, and electronics lends itself well to on-chip referencing and parallel measurements. The use of on-chip temperature compensation to improve refractive index sensing has been demonstrated recently by Gylfason *et al.* [124] in a slot-waveguide sensor using an external cavity diode laser at 1.3 μm .

For the sake of completeness, there are two additional comments we would like to note regarding the sensor types chosen for this comparison. First, optical fiber-based label-free sensors are not included in this comparison, as they lack the ability to take advantage of lithography to produce sensor arrays, but they represent an interesting and elegant approach for endoscopic applications. For an introduction to efforts in fiber-based label-free sensing, we refer the reader to literature [47, 48, 53].

Secondly, while it is not explicitly labeled as such, the efforts from UC Berkeley/University of Illinois Urbana-Champaign and the work presented in this thesis on VCSELs paired with photonic crystal guided resonances can be viewed as falling under the resonator category as well as being classified as interferometric-based sensors, such as those reviewed by Fan *et al.* [68]. Interferometric-based sensors are attractive for many applications, as phase-detection can provide high sensitivity, and reference arm configurations can help correct for thermal drift. Indeed, studies using interferometric backscatter (albeit with a sizeable Helium-Neon laser source and bulk optics) have reported a limit-of-detection as low as 2.8×10^{-9} RIU [121], as noted in Table 5-1.

Many of these label-free optical sensors are beginning to integrate microfluidics delivery into the system fabrication process. Since the manual fluidic handling in our proof-of-concept system extended both the testing time and the possibility of jostling the measurement setup due to forces when swapping the fluid samples, the development of microfluidics is expected to improve the mechanical stability during testing. Moreover,

with the optical components of our sensor now packaged in less than 1 cm³, the fluidic interface is one of the most bulky remaining elements. Scaling the size of the fluidics while providing a means for more efficient on-chip mixing and timed delivery can enable sensor systems with more automated and controlled testing.

5.5 Microfluidics Integration

To miniaturize and integrate the analyte delivery, we designed microfluidic circuits for existing photonic crystal samples and employed PDMS-based soft-lithography to fabricate the circuits at the Stanford Microfluidics Foundry. Soft lithography is a microfabrication process in which a soft polymer, such as PDMS, is cast onto a mold that is made from conventional photolithography. In contrast to our photonic crystal features that are on the order of 100-200 nm, the fluidic molds made from Si wafers are designed to have features ranging from 15 μm to hundreds or thousands of microns. Hence, the computer aided design (CAD) layouts can be printed onto inexpensive transparency films to serve as a cost-effective large-area lithography mask.

The basic microfluidic device with membrane microvalves to control liquids is composed of two PDMS layers, and thus requires two molds: one containing the flow channels, and the other containing control channels that can deflect the membrane microvalve into the flow channel to stop liquid flow when pressurized with air or liquid. For more information about microfluidic large-scale integration technologies, we direct the reader to a selection of review articles [127-130].

Using push-down valves where a top control channel presses the membrane into the adjacent flow channel to stop flow, two types of chips were designed: standard two-layer systems as well as new three-layer systems that enabled more testing flexibility.

Designs for the standard two-layer chips are shown in Figure 5-9. In the first design, a large area 3.2 mm x 3.2 mm corner reservoir allows one to reposition the fluidic chip to easily probe different areas of the photonic crystal. Six microfluidic channels (shown in cyan) allow the user to insert different solutions, including a flush line, to the chamber, while individual valves (shown in red) control the fluidic path to prevent unwanted backflow. The circular terminations indicate punch holes for 23 gauge stainless steel tubing that feeds into flexible Tygon tubing and syringes or a valved compressed air line.

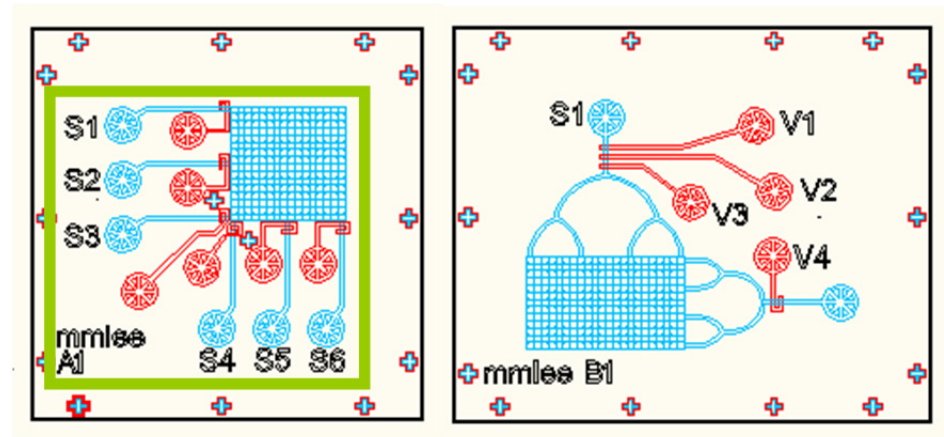


Figure 5-9: Schematic for two 2-layer microfluidic chips, featuring a valved control line and a flow line for the aqueous solution delivered to the photonic crystal.

Since the two-layer fluidic system relies on a substrate to seal the bottom of the microfluidic channel, all of the features on the PDMS chip needed to be within the photonic crystal sample area. With photonic crystal samples measuring less than 15 mm on a side, Figure 5-10 represents the smallest-to-date two-layer microfluidic chip that incorporates multiple controlled inlets fabricated in the Stanford Microfluidics Foundry. The second two-layer design (Figure 5-9b) has only one inlet port and one outlet port, with the 100 μm wide and 15 μm high channel splitting twice to increase the volume flow into the chamber. A trio of control valves (labeled V1, V2, V3 in red) is used for

peristaltic pumping of fluid. This design features a large ~3 mm x 5 mm chamber and enables manipulation of one aqueous solution at a time, similar to the original macrofluidic chamber, and allows for testing of the pumping functionality.

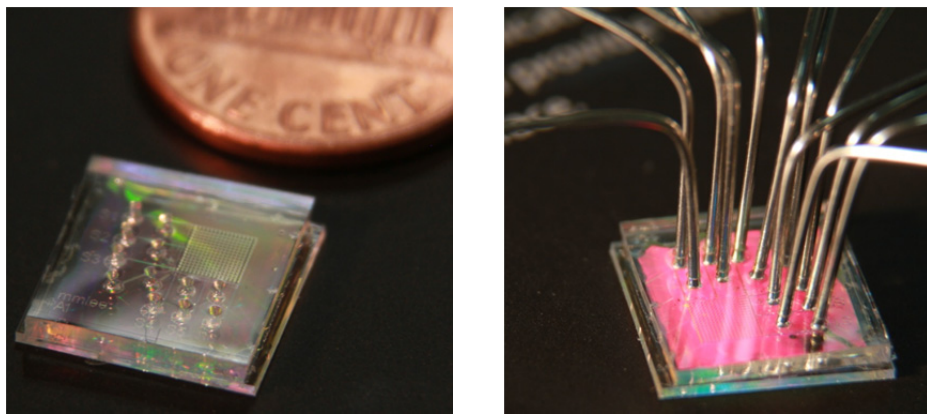


Figure 5-10: Photographs of two-layer microfluidic chip with a 3.2 mm x 3.2 mm reservoir mounted on photonic crystal slab. Stainless steel 23 gauge tubing is used for inlets and outlets.

While both of these two-layer designs reduce the amount of fluid needed for tests and represent a more integrated, low-cost approach for fluid handling than the macrofluidic channel, the need to seal the channels with a bottom substrate limits the chip area and the complexity of fluidic manipulations. Thus, we devised a new three-layer process compatible with the Microfluidics Foundry design rules to enable arbitrarily large and complex fluidic manipulations. As the CAD schematic in Figure 5-11 shows, the three-layer design features a top control layer, middle fluidic layer, and bottom fluidic reservoir layer. The control layer operates in the same fashion as in the two-layer designs. The middle fluidic layer is connected to the syringes and Tygon tubing through stainless steel tubing in the punch holes, as before, but instead of containing any reservoirs or testing chambers, the features are all “dead end” channels (shown in red in Figure 5-12). The addition of a third layer, with a fluidic chamber that overlaps the middle layer’s dead

end channels, provides a route for the fluid to complete the microfluidic circuit. Only the area of the reservoir in the bottom layer ($3.4\text{ mm} \times 9.6\text{ mm}$) is exposed and hence needs to be sealed by the photonic crystal substrate. To prevent unintentional collapse of the reservoirs, a 2D array with standard supporting pillars $50\text{ }\mu\text{m}$ in diameter spaced with a pitch of $200\text{ }\mu\text{m}$ is added.

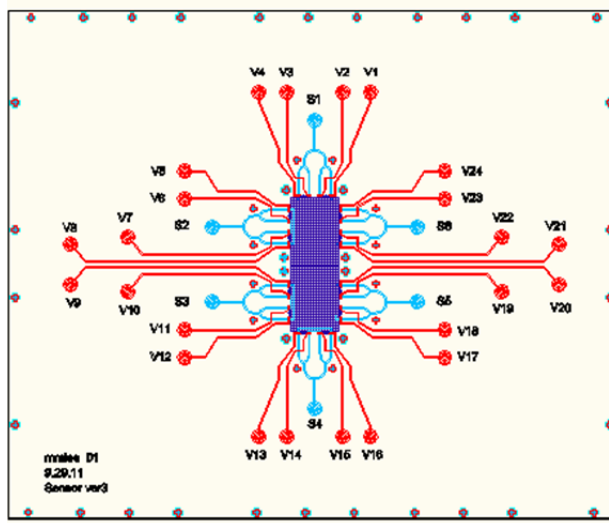


Figure 5-11: CAD schematic of three-layer microfluidic chip to enable more complexity without requiring a larger photonic crystal substrate to seal the entire area. The control layer (red) regulates flow of the middle fluidic layer (blue) with pneumatic valves. Dead end channels (blue) overlap a reservoir (purple) in the third layer.

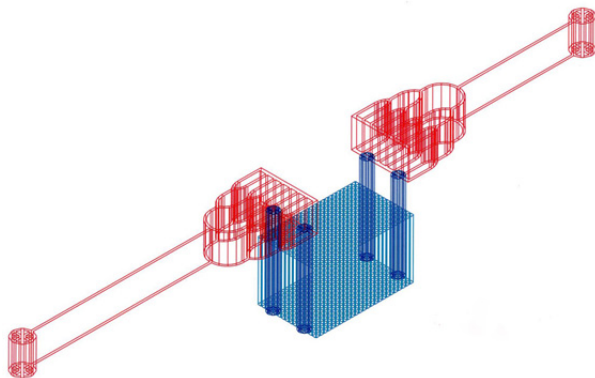


Figure 5-12: 3D CAD schematic of fluid layers, showing dead end channels (red), punch through connections (navy) and the reservoir (cyan). The z axis is scaled 100x to show the connections.

Figure 5-13 shows a photograph of a three-layer microfluidic chip, with the reservoir sealed by the photonic crystal. In this design, 24 valves and 6 source lines are demonstrated. These 24 valves can be controlled with portable compressed air canisters, with a prototype pneumatic manifold and bank of valves (Pneumadyne, Inc.) shown in Figure 5-14.

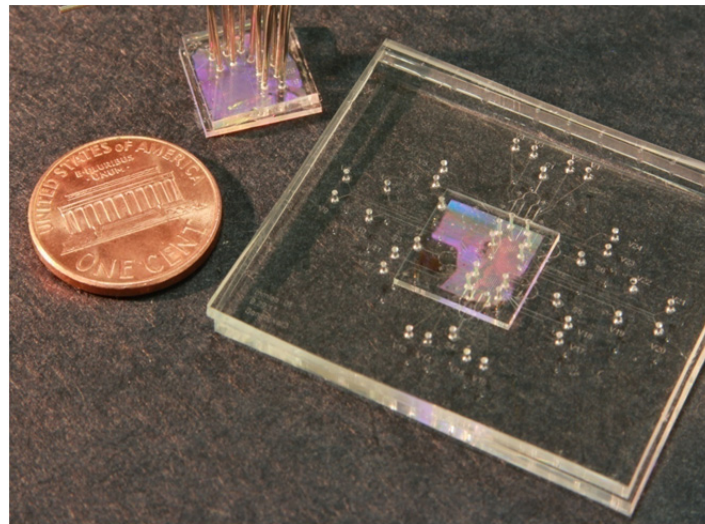


Figure 5-13: Photograph of a three-layer microfluidic chip with a photonic crystal sealing the chamber. For size reference, the smaller microfluidic chip and a United States penny are shown to the left.

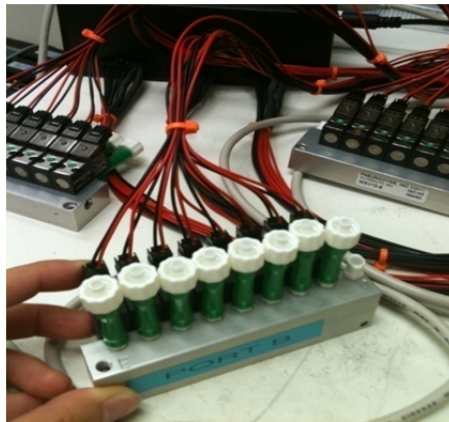


Figure 5-14: A pneumatic manifold and the corresponding valves designed for use with the control layer of the microfluidic chips shown in Figures 5-10 and 5-13. The valves can be operated with a MATLAB user interface for rapid pumping, mixing, and flushing.

Initial studies with the microfluidic system are promising, with real-time control of pumps and valves enabling rapid sample characterization. Issues such as the adhesion of the PDMS onto the photonic crystal surface to ensure sealed channels, quantification of flushing speed, and quality of flow in the reservoirs are under investigation.

5.6 Summary

This chapter extends the characterization of our photonic crystal resonators by demonstrating sensor sensitivity with temperature and current tuned VCSELs. This represents a significant reduction in the system footprint; the fiber-coupled broadband source and optical spectrum analyzers or spectrometers used in Chapter 4 can be replaced by integrated lasers and detectors packaged to be less than 1 cm³. In order to enable multi-modality sensing - in particular, parallel fluorescence and label-free sensing - for increased diagnostic confidence, we demonstrate a sensor system of TECs, VCSELs, detectors, and photonic crystals operating at 670 nm, where there are FDA-approved early cancer marker molecular probes for pre-clinical use.

Refractive index sensing shows differentiation of bulk solutions with a 25% change in transmission for 50% IPA and DI water, using a temperature and current tuned 670 nm VCSEL, corresponding to an extrapolated detection limit of 2.5 nM streptavidin. The sensor limit-of-detection is estimated at 10⁻⁴, as our designs have moderate only Qs and shifts of ~130 nm/RIU. Higher Q designs have been demonstrated, but since the experimental limitation is currently the alignment of the photonic crystal resonance with a limited VCSEL tuning range, the low-Q structures enable modest refractive index differentiation, which is better than not having any alignment between a possibly higher-Q photonic crystal and the ~3 nm VCSEL single mode tuning range.

Challenges in aligning the photonic crystal resonance to the VCSEL tuning range, adjusting for off-normal incidence light, and counteracting system drift over time are discussed in detail. We model the “worst case” (50% TE-polarized and 50% TM-polarized incoming light) spectral response for a beam with a finite divergence angle. In this scenario, the resonance broadens from ~2-5 nm to 20 nm FWHM. The angular dependence is seen to have destroyed many of the sharp reflection peaks and reduced the signal contrast from nearly 0-100% reflectivity to only 8-23% if a VCSEL’s natural divergence goes uncorrected. These quantifications enable the practical design and packaging of sensors, with new insight into the specifications for any micro-array collimation optics that will alleviate this non-ideal behavior.

While our initial measured sensitivity is less than the best reported performance of other label-free sensors, the utilization of VCSELs and integrated detectors for this platform has several advantages due to its compact size, scalability, and cost-effectiveness. To elaborate upon these tradeoffs, we include a critical comparison of this work with other optical label-free sensor results published in literature. Furthermore, we discuss key insights about photonic crystal angular dependence that can aid the development of future tunable designs. Finally, to shrink the last component of the sensor system, improve the speed of the assays, and enable stable delivery of fluids, we describe microfluidic delivery systems. Cost-effective PDMS microfluidic chips were designed and fabricated, and can enable rapid fluidic delivery, mixing, and flushing for the next generation of label-free sensors.

Chapter 6

Coupled Photonic Crystal Slabs for Sensing

“Two paradoxes are better than one; they may even suggest a solution.”

- Edward Teller

The devices discussed thus far have employed single photonic crystal slabs, where the electric field evanescently decays as one moves away from the slab surface. As Suh et al. theoretically proposed in [131], if two photonic crystal slabs (Figure 6-1) are brought together such that the distance between them is less than a wavelength, one can expect to observe rich optical phenomena arising from the evanescent coupling of each slab’s guided resonances. This chapter discusses how we can utilize coupled guided resonances in double photonic crystal slabs to design tunable label-free biosensors. We will see that the coupled structure offers a number of advantages over single-slab configurations, for applications in diagnostics as well as studies in the developing field of

mechanobiology¹⁹. Section 6.1 describes the motivations for investigating tunable-gap structures for biosensing. In Section 6.2, we discuss the design and simulation results for a coupled slab system with resonances in the VIS-NIR wavelength range. To rapidly characterize the double-slab behavior, we devised and constructed an experimental setup employing a wedge approximation to measure coupled resonances (Section 6.3). Finally, in Sections 6.4 and 6.5, we outline a polymer and piezoelectric-based device design and fabrication process to enable the creation of large-area coupled-slabs with tunable gaps.

6.1 Background

As we saw in Chapter 5, the ability to actively tune our biosensor provides measurement flexibility that can be invaluable, especially for point-of-care applications. With a pair of photonic crystal slabs, and, more importantly, with the volume in between them, we have an opportunity to increase light intensity in an easily accessible space and enhance the interaction between incident light and our biochemical molecules of interest. The double-slab structure provides more surfaces for analyte binding, and, as we shall describe in Section 6.2, electric field enhancement of more than a factor of 20 compared to a sensor with just a single photonic crystal slab. Moreover, the gap between the slabs can be optimized for different-sized analytes, and one can imagine tuning the gap distance, as illustrated in Figure 6-1, to measure a 2D “fingerprint” of intensity vs. wavelength for numerous gap distances to more thoroughly identify biomolecules of interest.

¹⁹ Mechanobiology is an emerging discipline that seeks to study the roles of mechanical forces, the extracellular matrix, and cellular structure on biological function. Insights about these roles could propel new developments in tissue engineering, therapeutic disease intervention, and translational medicine.

The structure shown in Figure 6-1 can be thought of as a Fabry-Perot resonator. Such resonators represent one of the simplest incarnations of coupled systems, and they have been considered for applications ranging from gravitational-wave detection [20, 74, 87-90] to optical cooling [42, 92-95] and sensing [131, 132]. In these examples, the separation between the two elements is designed to be large compared to the evanescent tail of the respective optical modes.

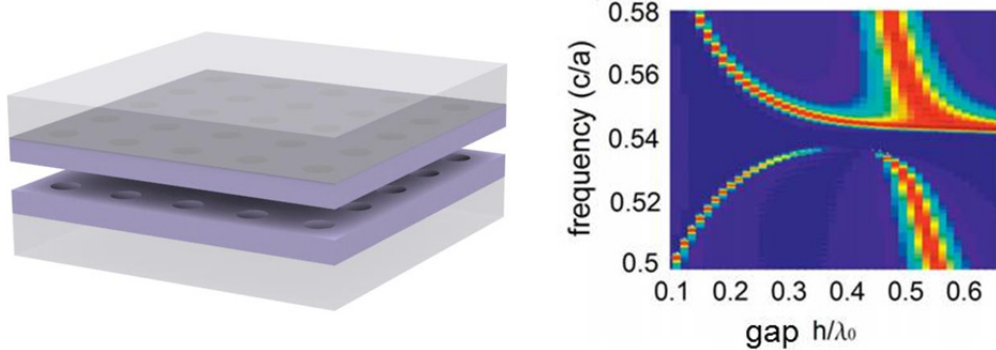


Figure 6-1: (a) Illustration of a double photonic crystal slab system. (b) Example of a 2D spectrum from [131], simulated for a pair of photonic crystal slabs, with intensity spectra for various gap distances.

In a different operating regime, if one designs the gap spacing to be less than 10% of the operating wavelength, one can devise a sensor for which the optical behavior is exponentially dependent on the optical path length, $n \cdot l$, in the gap between the slabs. Photons are not only able to propagate in free space between the slabs, but can also evanescently tunnel. Changing either the length of the cavity (such as in the case of a displacement sensor) or the refractive index inside the cavity (such as in the case of a label-free biosensor) by small amounts will influence both the near-field and far-field coupling between guided resonances. Specifically, in utilizing the evanescent tunneling pathway, we couple near-field information into far field transmission to generate a non-Lorentzian transmission response with respect to the optical path length. This in turn

translates to an enhancement in sensitivity, that, notably, can be obtained without the use of the high reflectivity mirrors required in conventional Fabry-Perot sensor designs. As we shall see in Section 6.2, this increased enhancement, combined with the flexibility that a tunable-gap double photonic crystal slab sensor design can provide, enables a number of possible applications.

Indeed, the range of optical phenomena offered by studying coupled systems has garnered great interest in recent research. Symmetric and asymmetric structures have been examined, in order to learn more about fundamental optomechanical forces and explore many emerging applications [133, 134]. Approaches range from simple planar interfaces separated from gratings and distributed Bragg reflectors by a gap to elaborate nanofabricated suspended membranes [135-137]. For tunable actuation, the incorporation of MEMS structures is promising; however, for many applications that require a large, flat surface, the undesirable membrane bowing in many actuation designs limits the useful membrane size. With research in mechanobiology increasingly looking towards systems that can realistically mimic the 3D environment for cells, there are many applications where it is crucial to create a mm-by-mm scale volume that can reproducibly stimulate samples with mechanical force.

For example, studies have indicated that the degree to which the extracellular matrix (ECM) is cross-linked (i.e., how much fibronectin is present) is an indicator of the presence and progression of cancer in tissue [138]. The amount of cross-linking in cancerous tissue is expected to generate an altered material response (for example, viscoelasticity) to mechanical stimuli when compared to the response from a normal tissue sample. Existing medical diagnostic procedures rely on fine needle aspiration biopsies that yield a syringe filled with a viscous material (~1 mm x 100s of microns).

This material is difficult to characterize, with staining procedures that are complex and time-consuming, cumbersome durometers, or AFM studies that are slow and offer a limited field-of-view. In contrast, an arrayable, compact, cost-effective device such as a tunable double-slab system promises the ability to correlate real-time tissue optical and mechanical responses with applied mechanical forces. As illustrated in Figure 6-2, by placing the sample in between two slabs, and applying compressive force of various frequency and duration, one could simultaneously monitor optical and mechanical responses. This could provide a wealth of data to help differentiate healthy and diseased tissue in many clinical applications.

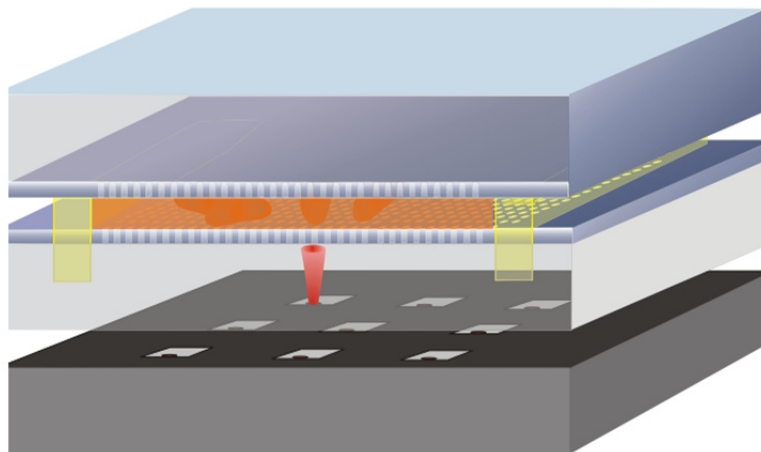


Figure 6-2: Schematic of a double-slab system to simultaneously monitor a tissue sample's optical and mechanical response to compression and extension forces. In a cost-effective cartridge-style system, piezoelectric transducers can bring the two slabs together, compressing elastic spacers.

6.2 Double-Slab Design

With these motivations in mind, several possible double-slab designs were evaluated. Considering the target applications in tissue diagnostics described in Section 6.1, the possible actuation mechanisms (Section 6.4), and the range of fabrication possibilities (Section 6.5), the design space explored included maximum gaps of up to hundreds or thousands of microns and the entire near-field coupled region, including the limit of a gap size of zero.

6.2.1 Simulations

The reflection spectra and field profiles for double-slab structures with various gaps were computed using the Fourier Modal Method [93]. The results shown are for a hexagonal lattice with a periodicity of 600 nm and hole diameter of 250 nm, with 250 nm thick SiNx. These parameters were shown in simulation to yield resonance in the VIS-NIR regime of interest, and the slabs were the best matched pair available from samples made originally for single-slab sensors. The slabs were assumed to extend infinitely in the xy plane, sitting on fused silica substrates. Figure 6-3 depicts a side profile view, with the position of the two slabs highlighted in purple. Any rotation or tilt between the two slabs was neglected; since the fields are continuous through each dielectric interface, the effect of slab-to-slab misalignment is expected to be minimal. Moreover, with the large area (~ 10 mm on a side) photonic crystals utilized, alignment of the edges of the two photonic crystal slabs within 2° is expected, and interferometric techniques can be utilized with the naked eye for adjusting parallelism (removing tilt) between the slabs.

As one can see in Figure 6-3, for a gap of 0.625 μm , simulation results indicate a 20x enhancement in the electric field intensity at the surface of the double-slab structure (red) compared to that of a single slab (blue). The volume in between the slabs allows for efficient overlap of the analytes with the field.

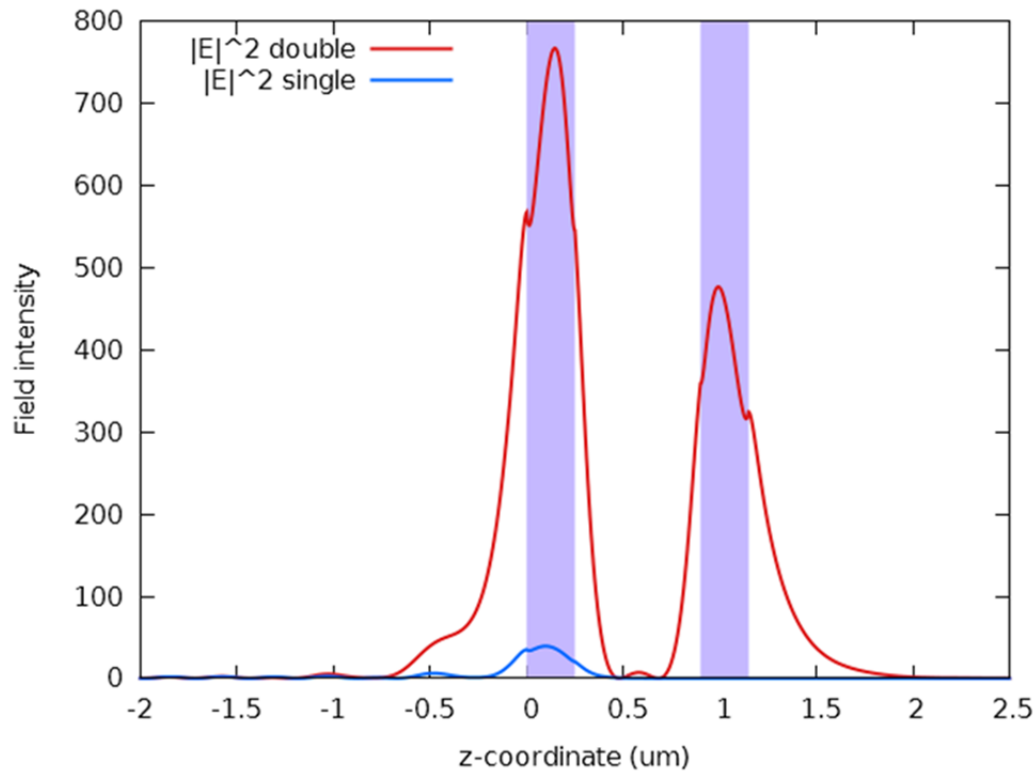


Figure 6-3: Simulated field profile for a double-slab structure (each slab is shown in purple). The square of the electric field for a double-slab configuration is shown in red; the value is ~ 20 x greater than the case for a single slab (shown in blue). The field values were In addition to the 20x peak field enhancement, the coupled slab system enables more efficient overlap of the field profile with the analytes, in an accessible volume between the slabs.

6.3 Wedge Approximation Experiment and Results

Although a double-slab structure that defines a tunable sample cavity is needed to enable many of the interesting mechanobiology studies described in Section 6.1, there are many challenges involved in fabricating a tunable gap (discussed further in Section 6.5). A simple characterization setup that allows one to optically characterize different gaps between the photonic crystal slabs is thus useful for approximating the behavior of the tunable coupled system. Figure 6-4 illustrates the use of a wedge configuration to enable transmission measurements of the double-slab structure with many gaps in a static device. By sweeping the light source relative to the sample with a pair of DC motors, one can effectively probe different gaps.

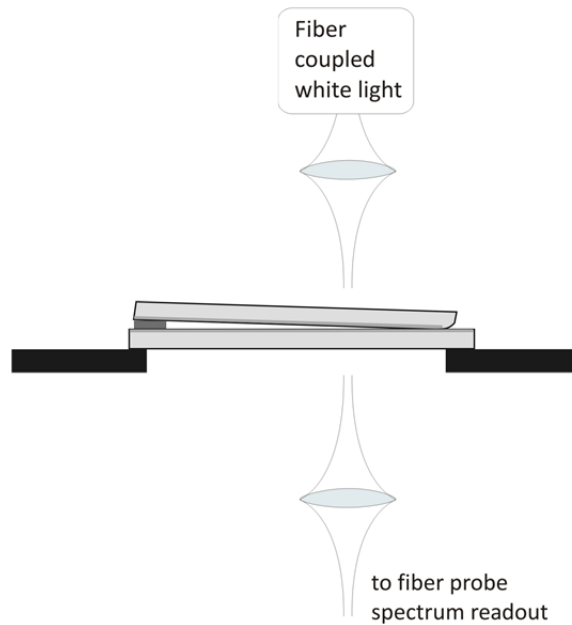


Figure 6-4: Schematic of the wedge approximation characterization setup. A fiber-coupled white light source can probe different effective gaps between the two photonic crystals in a static structure. For the 5 μm shim, an angle of 0.03° is formed between the slabs. The beam spot size (~500 μm) covers ~1000 periods and a difference in gaps of ~260 nm.

This is an approximation of the double-slab structure shown in Figures 6-1 and 6-2, as there is an angle between the two slabs. Hence, for a given transmission measurement, the incident beam illuminates a finite set of different gap sizes. For the large area (~10 mm x 10 mm) samples that were used, and a 5 μm shim, the angle between the slabs is 0.03°. With beam sizes on the order of 500 μm (~1000 periods of the photonic crystal pattern), this translates to one edge of the beam probing a gap that is 260 nm greater than the gap at the opposite edge of the beam. While such a variance is acceptable for large operating gaps on the order of tens of microns (e.g., for compressed tissue or small cellular studies), for smaller gaps, a smaller diameter beam or a thinner shim should be used to achieve a more accurate transmission response²⁰. For the initial characterization setup, the x - and y -axis motion-controlled minimum incremental step was ~2500x finer than the beam diameter, allowing position readout with an accuracy of 0.2 μm . The beam's Gaussian nature results in a weighted averaging of the different gaps probed in a single transmission measurement, improving the effective resolution of the data acquisition to better than the incident beam spot size.

To avoid damage during the assembly of the wedge, especially at the line of contact between the two photonic crystals, the upper photonic crystal was precision polished with a rounded edge. Since the photonic crystal samples were previously diced with an unpatterned border, this also allowed for the two slabs to be assembled with near-zero gap at the line of contact. The 5 μm shim was inserted at one edge in between the slabs, and custom-machined adjustable clamps with tips that were covered with Kapton tape were used to create a stable wedge shape, as illustrated in the photo in Figure 6-5.

²⁰ A supercontinuum source or tunable laser would have more power than the QTH lamp, and enable a smaller probing spot size. In addition, a straightforward shadow mask evaporation of 100's of nm of metal could replace the 5 μm shim for future characterization tests.

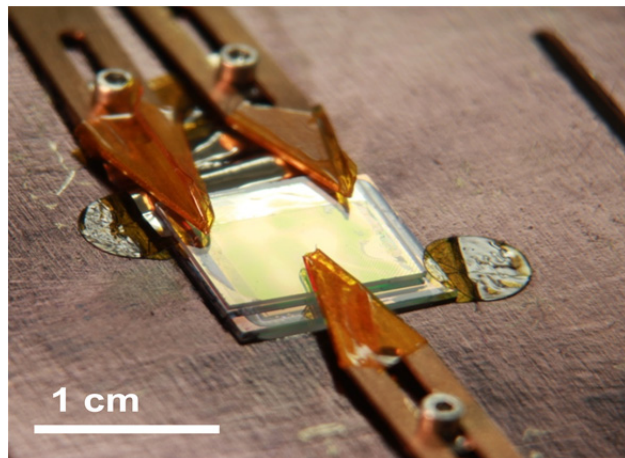


Figure 6-5: Photograph of the two photonic crystal slabs, with a $5 \mu\text{m}$ shim inserted between them on one side, and the rounded edge on the opposite side. Three clamps are shown; the sample holder allowed for additional clamps if needed to adjust the flatness of the samples.

The interference fringes arising from the two slabs were employed to iteratively adjust the position and pressure of each of the clamps. Care was taken to achieve even linear fringes repeating in the direction of the changing gap, utilizing the motion of fringes to identify the configuration that provided a monotonically decreasing gap from left to right as shown in Figure 6-3. In addition, an inverted microscope that had a manual z-adjustment option with $1 \mu\text{m}$ tick marks was used to focus through the wedge structure to confirm spacing.

As depicted in Figure 6-6, the custom sample holder was then secured with screws to a pair of stacked crossed-roller bearing linear stages that enabled sample movement in the xy plane with the integrated actuators and custom Java applets. The apertures of the linear stages allowed for transmission measurements and accommodated the placement of the lower achromatic lens.

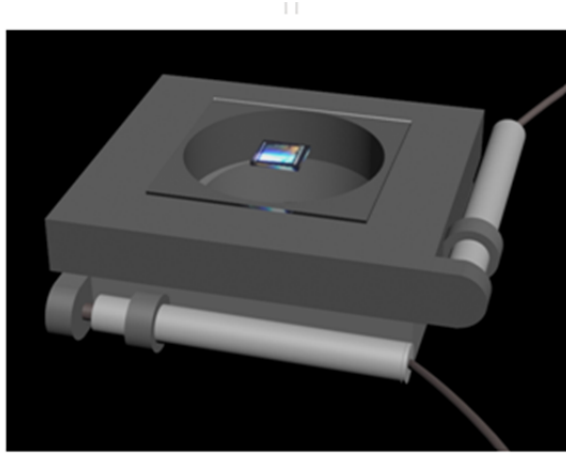


Figure 6-6: The sample mount (depicted as a transparent square in the illustration to allow visualization of the layers below) is attached to a pair of stacked crossed-roller bearing linear stages with apertures. Clamps (not shown) secure the photonic crystal slabs and the shim in between the slabs.

The pair of stages was then mounted on a mechanical bridge with sturdy posts, as shown in Figure 6-7. Decoupled from the sample and lower level bridge setup, a secondary bridge with an optical breadboard and four large posts was constructed. Attached to this bridge, a Quartz Tungsten Halogen (QTH) white light source with an aspheric F/0.85 focusing assembly and 0.125 inch glass fiber bundle, a pinhole, the first of an achromatic lens pair, and an iris were aligned. The second achromatic lens and pinhole were placed underneath the sample bridge, directing the transmitted light to a flip mirror that directed the signal to a fiber spectrometer sitting on a *xyz* stage. To align the probe spot to the desired area on the photonic crystal slab, a CMOS camera was placed on a sliding rail beneath the second achromatic lens.

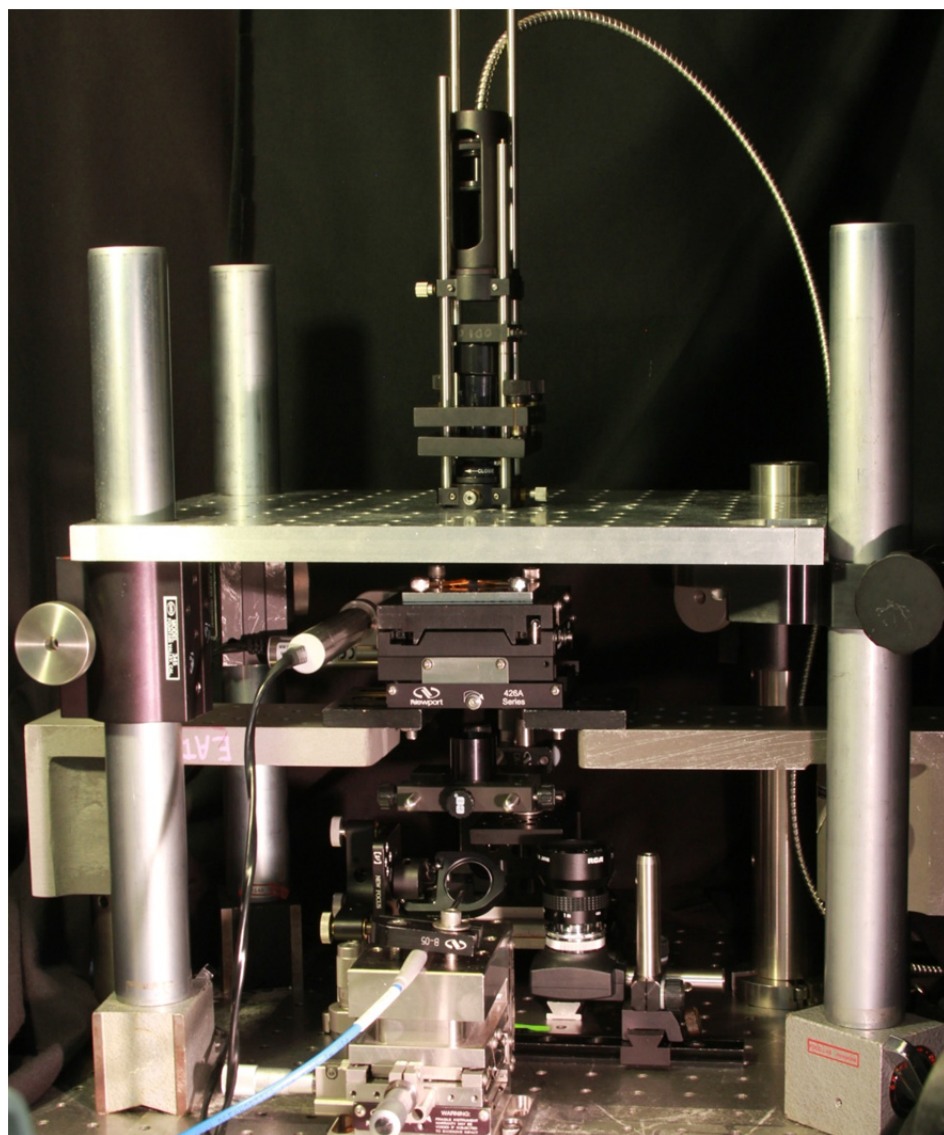


Figure 6-7: Photograph of the double-slab wedge experimental setup, with a Quartz Tungsten Halogen (QTH) fiber-coupled light source, motion controlled sample stage, fiber spectrometer, and a camera used for alignment.

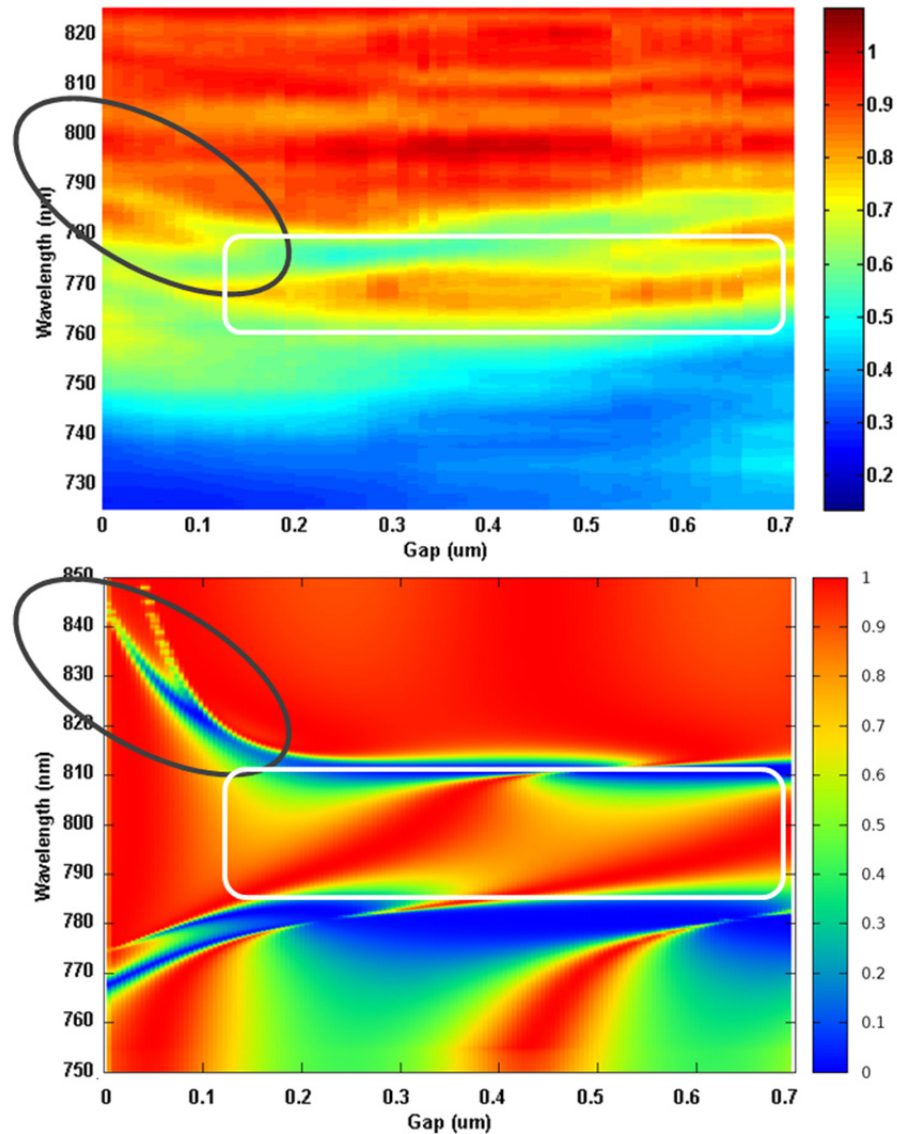


Figure 6-8: Experimental spectra as a function of gap for coupled photonic crystal slabs in a wedge configuration (top) correlate with simulation data (bottom). The color bar indicates normalized transmission intensity.

After alignment, the actuators were used to sweep the sample relative to the incident beam to probe the continuously increasing gaps. An incremental step of 10 μm was used for the majority of the scan, increasing to 20 μm after traveling a few

millimeters. The 10 μm or 20 μm steps in the direction of changing gap correspond to increasing the center gap distance by 5 nm or 10 nm, respectively, for each transmission spectrum collected. The x and y coordinates of the line representing a gap of zero (the edge of the top photonic crystal sample) were identified by use of the CMOS camera as well as the spectrometer. Due to the relatively coarse DC motor on-axis accuracy ($\pm 5 \mu\text{m}$) and uni-directional repeatability (2 μm), numerous spectra were collected near the contact line to ensure the data included the zero gap region. The experimental results shown at the top of Figure 6-8 are hence cropped to eliminate the signal collected through the bullnose radius and top edge (substrate and air interface) of the top photonic crystal, where there is no double-slab structure formed.

Even with the wedge approximation, one can see in Figure 6-8 that the experimental transmission scans for various gaps correlates with the expected simulation results. Since the as-designed and simulated geometry are expected to vary from the fabricated devices and the wedge approximation is employed, we note qualitative behavior that suggests further refinement of the characterization setup would be promising. One can see high transmission above 800 nm in the experiment, which corresponds to the high transmission expected in the simulations for wavelengths longer than ~ 820 nm. Two streaks of low transmission coupled resonances at 760 nm and 780 nm in the experimental results mimic the anticipated low-transmission resonances calculated to be present at 780 nm and 810 nm in simulations (circled in white). While the percentage error in transmitted signal is higher towards the zero-gap limit, even with the weighted averaging inherent to a finite beam, we may begin to resolve some of the resonances present at gaps less than 100 nm (circled in black). Improvements to the characterization setup now under way include the use of an ultra-broadband high power source and

precision linear stages with finer control of the minimum incremental step size, position accuracy, and repeatability.

6.4 Actuation Design

With promising agreement between simulation and the wedge-approximation double-slab transmission results, future studies of the system can incorporate gap tunability. This section provides an overview of the suggested cartridge style design pictured in Figure 6-9 that employs piezoelectric actuators and polymer spacers (indicated by the blue squares and yellow structures, respectively). To measure the gap at multiple locations, capacitive pads (shown in red) can be used [139, 140]. While other mechanisms, including electrostatics and thermal expansion,²¹ were investigated, the piezoelectric approach provides precise motion control of high loads and is compatible with double-slab designs that incorporate different spacer materials and dimensions, providing the most flexibility for tunable cost-effective implementation.

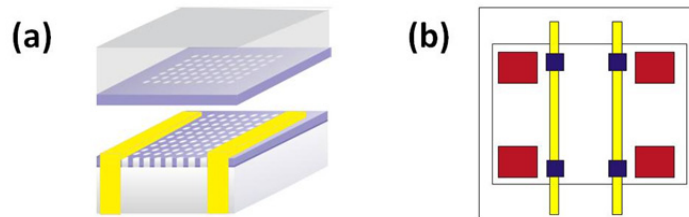


Figure 6-9: (a) A double photonic crystal slab on thick fused silica with trenched polymer spacers (in yellow) enables a large percentage of compression relative to the exposed spacer volume. (b) A top view showing actuation contact points (blue) and capacitance pads (red) for measuring the gap.

²¹ The expansion of a metal spacer via Joule heating, or of a piezoelectric spacer via the piezoelectric effect, can be used to increase the gap. A trenched design similar to that shown in Figure 6-9a, but with electroplated metal or piezoelectric spacers, enables a larger perceived percentage change in the gap. These mechanisms would eliminate the need for external piezoelectric actuators, but the machinability constraints (and hence lack of control of the flatness) of such spacers limit the usefulness of this approach.

The two primary options for fabrication strongly influence the actuation details: one can either fabricate the two slabs in-place on one substrate [141, 142], or opt for the assembly of two pieces through bonding. While the former option is attractive for alignment, the bonding method is well-suited to accommodate adjustable spacers between the slabs without sacrificial layer processing. In addition to permitting a larger range of gap sizes, the bonding method allows for the use of thicker substrates for improved flatness.

Figure 6-10 illustrates the results of a COMSOL multi-physics simulation showing the flatness²² during actuation with respect to the substrate thickness. For this simulation, the spacing between the two PDMS spacers was set to a “best case” 5 mm, which provides adequate area to optically probe the photonic crystals, but reduces the bowing compared to PDMS spacing of ~10 mm for the ~10 mm x 10 mm top photonic crystal. For substrate thicknesses greater than a couple of millimeters, the flatness is significantly reduced compared to the case of standard 500 μm thick wafers.

In order to collect intensity spectra for different gap distances such as the data shown in Figure 6-8, one must be able to reliably sweep the gap distances. Ideally, one would control data acquisition with a feedback system that allows one to measure and adjust the gap before each spectrum collection. While measuring and controlling such gaps can be achieved with positioning tools that provide a full six degrees of freedom in contemporary lithography applications [143], such systems are prohibitively expensive for the cost-effective diagnostic realm.

²² This is defined as the z coordinate of the center of the photonic crystal sample relative to the z coordinate of the sample edges where the capacitance-based gap measurement would be taken.

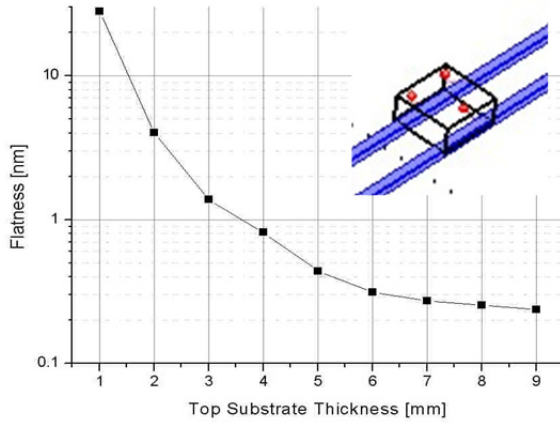


Figure 6-10: COMSOL simulations show that increasing the top substrate thickness by a couple of millimeters improves the flatness (and hence gap uniformity) during actuation.

A more reasonable solution for our target application space is the use of capacitance measurements [139, 140] and the aforementioned piezoelectric actuators. A trenched polymer spacer such as that depicted in Figure 6-9 can be compressed and adjusted, relaxing constraints on the as-fabricated spacer flatness and uniformity. The limitation to the design is that the optically probed area is not precisely where the gap is measured via capacitance; with high-uniformity photonic crystals that can be fabricated with today's standard lithography, however, this issue is mitigated.

For applications requiring thick substrates to ensure minimal warping of the photonic crystal and even compressive forces, the fabrication processes described in Chapter 4 (originally designed for 500 μm thick wafers) need to be modified. The following section describes a process development flow designed for double slabs with thick substrates.

6.5 Process Development

The thicker substrates began with fused silica (synthetic, ground, and unpolished, Hayward Quartz) that was polished at the Stanford crystal shop. As shown in Figure 6-11, the custom substrates were made to have a thinner rim to fit into existing fabrication clamps for cleaning and metallization. The substrates were cleaned and SiNx was deposited via PECVD, with similar processing steps to those described in Chapter 4. For the thicker substrates, however, care was taken with an ultrasonic clean and the PECVD steps were modified to reach thermal equilibrium across the substrate before deposition.

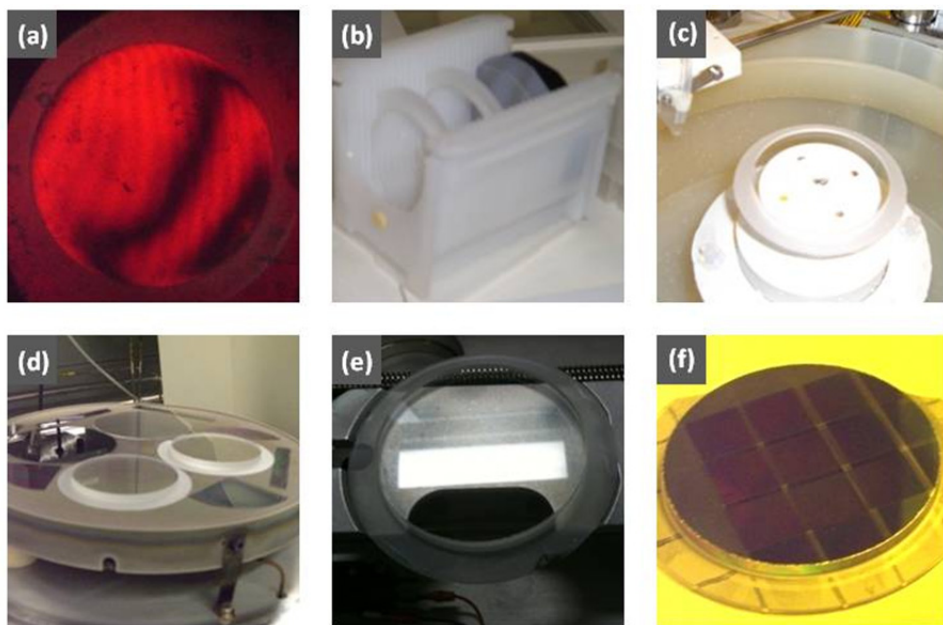


Figure 6-11: Photographs taken during the thick-substrate photonic crystal fabrication process. (a) Interferometry was used to estimate flatness and parallelism. (b) Thinned rims were compatible with existing wafer holders and equipment. (c) Increased vacuum suction was needed during wafer spinning. (d) SiNx was deposited via PECVD, using a process similar to that described in Chapter 4 for standard thickness wafers. (e) 4-inch wafers fit into existing etchers. (f) Interference lithography was used to pattern the thick wafer with nine large area photonic crystals.

Following nitride deposition with PECVD, the samples were patterned with interference lithography. Again, it was necessary to adjust the resist spinning parameters and chuck vacuum to account for the larger mass of the thicker wafers to obtain a uniform resist layer. As shown in Figure 6-11e, an entire 4-inch wafer was patterned with nine large photonic crystal areas on the thick substrate.

After the photonic crystal holes are etched and the resist and ARC layers are removed (similar to the processes described in Chapter 4), the wafer can be diced if needed. Diamond saws were able to create trenches like those illustrated in Figure 6-9, with ~1-3 mm widths to allow for side-injection of PDMS for spacers with the use of Teflon guides for casting. To enable gap measurement and feedback, fabrication techniques used in MEMS processing to create wrap-around capacitance pads for both slabs could be integrated; another option is to make the bottom photonic crystal slightly larger and have at least the electrical readout contacts from one slab directly accessible from standard CMOS processing techniques. While the process described here and in Appendix A.3 was used for wafers up to 6 mm thick, initial testing indicates that the ~3mm thick wafers provide flatness benefits while being much easier to handle in the clean room. Hence, for future studies needing large area samples and tunable gaps, less aggressive scaling of the thickness is recommended to allow for the use of more standard processing techniques.

6.6 Summary

The interaction between two photonic crystal slabs can provide a set of rich optical phenomena arising from the evanescent coupling of each slab's guided resonances. With the pair of photonic crystal slabs and the volume in between them, we have an

opportunity to enhance the interaction of light intensity and our biochemical molecules of interest in an easily accessible space. Such a structure provides field enhancement of more than a factor of 20 compared to a single-slab sensor, an opportunity to optimize the volume for different-sized analytes, and the ability to measure a 2D “fingerprint” of intensity vs. wavelength for numerous gap distances to more thoroughly identify biomolecules of interest.

To rapidly characterize the double-slab behavior, we designed and constructed an experimental setup to measure coupled resonances, employing a wedge approximation. The experimental spectra for a range of gaps, in steps as small as 5 nm and including the limit of a zero-gap, correlate with simulated results. With this promising experimental agreement, we design a polymer and piezoelectric-based device fabrication process to enable the creation of large-area coupled-slabs with a tunable gap. Such a system can provide cost-effective, cartridge-style real-time analysis for applications in diagnostics as well as studies in the developing field of mechanobiology.

Chapter 7

Conclusions

“We shall not cease from exploration, and the end of all our exploring will be to arrive where we started and know the place for the first time.”

- T.S. Eliot

The development of new detection and monitoring technologies promises to revolutionize our response to not only rapid-onset epidemics, but also longer-term and more common diseases. By drastically reducing sensor size, cost, and wait times, we can envision combining multiple sensing mechanisms onto a handheld lab-on-a-chip for more accurate and reliable correlated diagnostics. Many of these miniaturized sensor technologies are particularly well-suited to real-time, continuous monitoring and implantation, providing a foundation for cost-effective theranostics²³ and future advances in personalized and predictive medicine[144, 145].

Redesigning biochemical analysis systems to enhance detection performance and to capitalize on integrated manufacturing techniques is crucial to the practical realization

²³ I.e., a *portmanteau* of the words therapeutics and diagnostics. Theranostics is a proposed process that first diagnoses a patient and then tailors a therapeutic treatment for them based on the test results.

of handheld biosensing. In addition to being sensitive, specific, cost-effective, and well-suited for multi-modality detection, biosensors for a lab-on-a-chip must tolerate a wide range of operating conditions to be field-deployable. Especially for point-of-care diagnostics, where the testing environment can be highly variable, it is advantageous to have a sensor with a tunable operating range. Creating an entire suite of tailored sensors would allow the user to collect a broad dataset despite any non-ideal environmental conditions, for novel analysis and more thorough diagnostics.

To address these opportunities, in this thesis, we have presented the design, fabrication, and characterization of tunable biosensors with compact and low-cost Peltier coolers, lasers, integrated detectors, photonic crystal slab resonators, and polymer microfluidics. All of the components utilize scalable semiconductor and soft-lithography techniques to significantly reduce the required device footprint, simplify system assembly, and enable large-scale, economical manufacturing.

The following Section 7.1 provides a summary of key contributions and insights from this work that can aid the design and implementation of future label-free biosensors; these are described throughout the thesis, but collected here for convenience. In Section 7.2, we describe future research directions that can build upon the topics discussed in this work, and provide a broader outlook on potential applications in biomedical diagnostics.

7.1 Summary

7.1.1 Label-Free Sensor Design/Fabrication/Characterization

Guided resonance modes in 2D photonic crystal slabs were examined for use with Vertical Cavity Surface Emitting Lasers (VCSELs), with a focus on 650-900 nm operation

in the biological transparency window. Although the VIS-NIR photonic crystal slab fabrication (particularly for the 670 nm designs where 400 nm pitch and ~70nm radius holes were needed) required the use of less-readily-available interference and nanoimprint lithography techniques and a notable amount of processing development, the obstacles were surmountable. Several samples, with sizes ranging from ~5 mm x 5 mm up to 12 mm x 12 mm, were fabricated, as described in Section 4.2.

One of the more challenging aspects to the prototype development was the design of appropriate characterization techniques and detection methods. As we saw in Chapters 3 and 4, polarization/angular dependencies as well as sample non-uniformities in the photonic crystal slabs were observed with spectrometers and Scanning Electron Microscopy (SEM)/Focused Ion Beam (FIB) imaging. Hence, in order to recreate the guided resonances measured in broadband systems with our VCSEL-based sensing scheme, we had to first devise a system where both white light as well as the VCSEL beam could strike the photonic crystal at the same location with similar angles. Since we relied upon a fairly weak QTH lamp, we had to balance the requirements of a broadband 1:1 imaging system and the VCSEL which was originally designed to be placed directly beneath the photonic crystal. This required careful selection of achromatic lenses and alignment procedures to ensure that the beams were co-located on the photonic crystal. Our approach was successful in identifying the resonance spectra *in situ* before taking data with the VCSEL, and had the added benefit of enabling studies on the effect of incident beam quality on the transmission and reflection spectra.

While this non-uniformity complication could have been avoided (if the fabrication of all the sensor elements were more tightly controlled), the practical challenge drew attention to the importance of the sensor operating range and tunability. This

influenced the design and fabrication processing flow development of later sensors, especially the double-slab configurations discussed in Chapter 6.

7.1.2 Demonstration of Index Sensing with 670 nm VCSELs

We provided a proof-of-principle demonstration of refractive index sensing in bulk aqueous solutions utilizing temperature and current-tuned 670 nm VCSELs. In contrast to existing results published in literature on VCSELs for label-free sensing, this work features monolithically integrated VCSELs and detectors and operates at the challenging deep-red 670 nm regime for compatibility with fluorescence sensors that take advantage of FDA-approved molecular probes such as Cy5.5. Low-loss, all-dielectric resonant photonic crystal slabs, microfluidic delivery chips, prototype packaging, and the integration of a miniature TEC for fine temperature control and single-mode preservation are realized in this work to enable point-of-care handheld sensing.

The index sensing experiments performed for different bulk solutions at 670 nm with tuned VSCELs yielded a measured \sim 130 nm/RIU shift and 25% change in intensity visible between DI water and 50% (v/v) IPA. This is comparable to simulations, but further engineering of the measurement setup is needed to be able to detect smaller refractive index changes. A few of the key issues that emerged in this endeavor included the alignment of the photonic crystal resonance with the limited single-mode tuning range of the VCSEL, the thermal transients when sweeping the laser temperature, and the angular dependence of the spectra. These are quantified in Chapters 4 and 5. Notably, the incremental wavelength control when one can control the temperature to within 0.5 $^{\circ}$ C is \sim 0.03 nm for VCSELs at 670 nm. This is smaller than the minimum linewidth that

can be measured by many optical spectrometers, providing excellent wavelength resolution without the need for cumbersome equipment.

In this work, we have replaced bulky and expensive broadband sources and spectrometers (often 10s of centimeters to a meter long, and thousands of dollars) with cost-effective, integrated, and scalable sources and detectors that can be produced at the wafer-scale for cents to dollars per unit. This substantial reduction in size and cost means, however, that one must carefully engineer the performance of the miniature components. Specifically, since we can no longer rely on broadband spectra to view the photonic crystal resonance, and are instead aiming to trace just a fraction of the relevant reflection spectra, the narrow (few nm to 10s of nm FWHM) resonances must coincide with the wavelength range of the incident light. We found that, particularly for 670 nm where the materials and thermal constraints make wide temperature tuning more challenging than in designs for higher operating wavelengths, the few nanometers of single mode temperature tuning range can be a practical limiting factor. Hence, until the photonic crystal slabs can be reliably fabricated²⁴ or tuned to match the range of as-fabricated VCSELs, options such as MEMS tunable VCSELs can provide an attractive, albeit slightly more complex, solution.

7.1.3 Examination of Photonic Crystal Angular Dependence

The sensing experiments not only shed light on the fabrication tolerances for the system components, but also highlighted the importance of understanding a few key non-idealities that had previously not been investigated. For example, it is well-known that a coherent light source such as a VCSEL offers a more narrow divergence angle than other

²⁴ I.e., in a research university setting or fabrication facility that can accommodate the requisite materials such as fused silica substrates. The dimensions of ~100 nm holes and ~400-500 nm periodicity can already be achieved at the wafer scale in industrial facilities at this time.

alternatives. However, even the $\sim 8^\circ$ half angle divergence quickly translates into issues when used with a photonic crystal slab due to the slab's angular dependence. In this work, we clarify the angular dependence of photonic crystal guided mode resonance sensors. The natural uncorrected divergence of a typical oxide-aperture VCSEL is shown in a “worst case” (50% TE-polarized and 50% TM polarized) scenario to broaden resonances from 2-5 nm FWHM to over 20 nm FWHM, destroying many of the sharp reflection peaks and reducing the signal contrast from nearly 0-100% reflectivity to only 8-23%. These quantifications enable the practical design and packaging of sensors, with new insight into the specifications for any micro-array collimation optics.

7.1.4 Design of Coupled Slabs for Tunable-Gap Devices

We designed a new double-slab device and fabrication process flow, featuring a piezoelectric and polymer-based actuation mechanism. The device design enables simultaneous study of optical and mechanical properties of large $\sim \mu\text{m}$ to mm size samples such as cells and tissues. An experimental setup was created to characterize the effect of photonic crystal slab coupled guided mode resonances, employing a simple wedge configuration and position scanning to enable the measurement of various gaps (from microns down to a zero-gap) with nm resolution. Compared with single-slab devices, these double-slab designs offer increased intensity enhancement (a 20x increase is presented for a gap of $0.625 \mu\text{m}$ in this work) and an opportunity to differentiate captured molecules with an additional dimension of data from an intensity spectrum vs. gap 2D “fingerprint.” This 2D fingerprint was simulated for double slabs with coupled resonances in the 760-810 nm range, and experimentally measured, showing good agreement with resonances in the 760-790 nm region for the first time to our knowledge.

This effort highlighted the importance of simulating non-idealities, as the effect of the wedge approximation is yet to be quantified with available tools. In addition, the development of the characterization setup as well as the fabrication process emphasized the need to constantly balance tradeoffs between measurement or fabrication complexity and practical applications, as discussed in Chapter 6 and Appendix A.

7.2 Future Work

Based on these results and insights, there are several directions for future exploration and development. The first suggested projects described below describe possible improvements to the underlying technology, with an emphasis on device design, simulation approaches, and fabrication methods. We then describe extensions of this work that would address various biomedical applications, focusing on a few key areas where the cost-effectiveness and multi-modality capabilities of such a platform have the potential to disrupt existing markets and enable new functionality.

7.2.1 Increased Simulation and Design Capabilities

To improve the limit-of-detection, we would like to maximize the field intensity in areas of the sensor that are accessible to analytes. Modern simulation tools are just now becoming fast enough to enable the optimization of geometric and materials parameters for structures like photonic crystal slabs. This will allow for more efficient design of future structures; however, additional simulation tools are needed to ensure designs that are robust to testing conditions. Based on our experiments, we describe here some key simulation tool functions that would enable more effective optical biosensor design.

As we saw in Chapter 5, the effects of off-normal incidence and more realistic (non-plane-wave) light are of interest. A quantitative evaluation of the tolerance to beam divergence and component misalignment would guide the choice of beam shaping elements and set packaging constraints, greatly affecting the complexity and costs of the system. We presented a “worst case” polarization scenario for VCSELs in this work, but obtaining a more thorough understanding of the expected optical behavior as a function of beam quality will be crucial to the practical implementation of these photonic devices. In addition, as we imagine scaling the sensor components to their size limits, the effects of finite structures (both the sensor and the analyte to be detected) become relevant. At this time, the computing power needed to study a finite (non-periodic) sample size of ~100s of microns to millimeters precludes rapid or thorough studies. Future work on simulating finite photonic crystal sample sizes would allow the designer to effectively space sensor elements in arrays to minimize crosstalk and degradation of the signal-to-noise, while balancing the need for integration density.

Finally, we saw in Chapter 6 that in practice the interaction between two or more photonic structures can yield interesting phenomena. Although the coupling behavior for two slabs placed various distances apart can be simulated, and is shown in Section 6.2, we assumed perfect alignment of the periodic structures. Since the fields are continuous through the structure’s interfaces, we believe this is a valid approximation; however, quantifying the effect of rotation or tilt between the structures would be insightful and help guide the assembly or design of future coupled structures. Especially since breaking symmetry has been shown to introduce sharp features in transmission, further study of these tolerances could enable more effective characterization and perhaps even generate new applications.

7.2.2 Sensor Component and Array Optimization

For the individual components of the sensor, as mentioned in earlier chapters, the addition of polarization control, improved filtering, and increased wavelength tuning range would help performance and relax fabrication tolerances. Another useful improvement, mentioned in Section 4.1.4, would be to develop reference detector schemes to be able to normalize any drift of the laser excitation power. Because of the inherent scalability of the sensor arrays, it would be straightforward to monitor laser intensity on a second channel. Correction for drift could also be achieved by monitoring the spontaneous emission that couples between the VCSEL and detector through the transparent DBR layer. A second or third channel could also be used to monitor absorption and scattering, adding another sensing modality that could, for example, quantify blood oxygenation level [37].

Further investigation into array crosstalk and ensemble performance would be beneficial for cost-effective scaling of parallelized, multiplexed sensors. Operating arrays of devices simultaneously in close proximity (without dicing and repackaging or the use of multiple TO-header type components) would enable compact imaging. Future implementation work in effective readout and wireless transmission of the data into a cloud-based architecture would allow untethered, implantable monitoring for a host of new applications.

7.2.3 Interface with Biology and Users

To further the practical deployment of the sensor, a large number of studies on the biocompatibility and specificity could be completed. While future research could characterize the quality of cleaning procedures for re-use of *in vitro* devices, contamination concerns and the as-designed cost-effective nature of these chips points to

a disposable model, where the materials could be sent back periodically for recycling, but the patient's biological sample would remain isolated from future samples. Nevertheless, questions on the durability of the biorecognition layer and ability to ensure a long shelf-life for the devices in harsh environments offer many opportunities for relevant studies. For *in vivo* applications, there is a host of research on bio-fouling and implantation longevity that are of interest.

Moreover, the user interface of such systems, whether they operate *in vitro* or *in vivo*, is an important factor in successful implementation, especially in developing countries or isolated communities where user support may be quite limited. Hence, the human interaction with the sensor system, including sample preparation, data communication, interpretation of results, and any required maintenance (such as replacing batteries or running calibrations), should be revisited for ease of operation and robustness for specific applications.

7.2.4 Multi-Modality Sensing

Perhaps the most significant technology directions emerging from the development of this platform are those that propel more multi-modality sensing. The components used in both the single- and double-slab sensor demonstrations, including the TEC/VCSEL/detector, photonic crystals, and piezoelectric actuator designs, are well-suited for simultaneous and parallel measurement of numerous optical and mechanical parameters. Raman scattering²⁵ with the sensor components developed here would be a

²⁵ When a photon encounters and scatters from a molecule, the vast majority of photons scatter elastically, at the same wavelength. A few photons scatter inelastically via Raman scattering, by either gaining or losing energy to the molecules' vibrational states.

natural extension. Because the vibrational energy characteristic of a molecule is unique, depending upon specific chemical bonds and conformation, Raman scattered photons form a spectra that is unique to the molecule. Raman measurements generally require a high power external pump laser, and a high resolution scanning spectrometer with a sensitive detector. However, one could envision the use of tunable lasers (from TECs or current tuning, as demonstrated in this thesis, and the use of gratings for wavelength extension as described in Section 4.1.4), and large detectors with separate bandpass filters that probe individual portions of the Raman spectra.

The development of different detection modalities that could be integrated for simultaneous, correlated sensing and imaging offers a multitude of clinical applications. Recent work on triple modality sensing [146] with magnetic resonance imaging (MRI), photoacoustic, and Raman scattering modalities was shown to help delineate the margins of brain tumors in living mice, both preoperatively and intraoperatively. Such approaches where medical professionals can collect and correlate information from multiple approaches promises to provide unprecedented accuracy and diagnostic value. Immediate uses that take advantage of the real-time, continuous, cost-effective benefits of our platform include pharmacokinetic studies (where there are separate periods of time when high temporal resolution is important), previously unobtainable continuous studies of long-term dynamics, and the deployment of sensors to resource-limited areas where size and cost have thus far prevented access. Designing cost-effective, integrated, and scalable incarnations of such multi-modality systems would provide a tremendous extension of our diagnostic capabilities and enable a wide range of applications.

Appendix A: Fabrication Techniques

A.1 Photonic Crystal Slab Process Flow

This is the basic process flow used to create the all-dielectric photonic crystal slabs for VIS-NIR. The nanoimprint lithography process described in Section 4.2.4, or conventional optical lithography, can be used in place of the interference lithography described here.

Wafers used: 4 inch fused silica (Hoya 4W55), and standard Si wafers from Stanford Nanofabrication Facility (SNF) stockroom

1. **Wafer cleaning:** Piranha cleaning, on wbnonmetal Wash-Rinse-Dry

2. **PECVD Nitride deposition**

STS PECVD to deposit SiNx layer 200-250 nm with standard recipe

Parameters: 2% SiH₄ (Silane) - 2000 sccm, 100% NH₃ (Ammonia) - 35 sccm

Uniformity ~ 1%, deposition rate ~was 73 Å/minute (~30 min deposition)

Steps:

Cleaning cycle, with no wafer inside machine – coat walls with 250 nm nitride

Coat calibration sample 4 inch Silicon wafer, and measure SiNx layer thickness using Rudolph ellipsometer, Woollam ellipsometer and/or nanometrics thickness monitor

Coat actual sample and a witness Si wafer

3. **Interference lithography:** Nd:YAG laser, tripled in frequency from 1.06 µm to 355 nm, pulsed energy 50 mJ; 60 Hz. 2D arrays of holes were patterned on samples as large as 4 inch wafers.

Recipe:

Spin. Coat with bi-layer resist (adjust according to sample size): Brewer Science, ARC i- CON-16 conformal BARC to control substrate reflectivity and enhance the critical dimension control first, then on top of the ARC spin Shipley SPR505 or NR700photoresist coated at 4000 rpm. (SPR has shown better uniformity thus far). Bake resist on a hotplate at 90 °C

Expose. Double exposure with 90° rotation, using black paper mounted above the wafer when needed to define different size photonic crystal areas

Develop. Develop samples with tetramethylammonium hydroxide developer (MEGAPOSIT, MF 702) - could be developed at Univ. of New Mexico and also again at Stanford if needed, followed by a DI water rinse

4. **Coat:** Deposit 50 nm of Cr or Ti at Stanford (Innotec, ES26C evaporator at ~0.3 Å/sec deposition rate). The chrome serves as a mask for subsequent pattern transfer of the photonic crystal holes.

5. **Liftoff:** Acetone liftoff process, as described in Chapter 4
6. **Etch:** NF₃ dry etch on tool similar to AMT etcher (semiclean) / PQuest/ p5000/drytek to etch resist and SiNx, stop on quartz (timed).
Sample mounting: use 4 inch Si carrier wafer, mount samples onto carrier wafer using Kapton tape. (Can spin coat 1 μm 3612 resist, remove edge bead from carrier wafer, mount small sample onto the resist layer).

Steps:

Seasoning chamber using etch recipe for 15 minutes. See plasma color stabilize, and bias voltage stabilize after ~ 10 minutes.

Test sample etching: mount a dummy sample and inspect etch rates
SiNx etch rate ~ 540 Å/minute for 4 minute NF₃ etch.

Etch real sample: AMT etcher, NF₃ etch. Load program from program 55 to process 5, program 5. Parameters: Verify change to voltage control at Bias voltage = -390 V, 15 sccm flow rate of NF₃, 40 mTorr pressure, 8 minutes etch time (hold step is added before etch to verify Hexode temp. cooled to 20 °C). Continue from hold step, record etch parameters along the run. (pressure, temp, incident and reflected power, Bias voltage. Typical values: 41.3 mTorr, 20 °C Hexode temp. -387 V bias voltage, 780 ±10 W power, 20 W reflected power)

7. **Descum:** O₂ plasma with Drytek4 etcher
8. **Sample Dicing:** Dice wafer in Ginzton crystal shop to square samples
9. **Sample cleaning:** Organic solvent cleaning: Acetone, Methanol, Isopropanol. 10 minutes in ultrasonic bath for each solvent. Dry sample.

A.1.1 Nanoimprint Lithography

This can be substituted for the interference lithography step to pattern SiNx photonic crystals directly. In addition, "father" stamps can be made out of pure silicon in order to imprint SiNx as a subsequent step.

1. prepare appropriate wafer (can be silicon on fused silica depending on which NIL tool used). If patterning directly (vs. creating father stamp), deposit photonic crystal SiNx layer on fused silica substrate
2. coat with a Cr mask, photoresist, and an imprinting resin
(80% benzylmethacrylate, 10% methacryloxypropyl-terminated polydimethylsiloxane, 5% polybenzylmethacrylate, and 5% trigonox 21ls curing agent)
3. thermal (or UV) nanoimprint pattern transfer: Low pressure (25 atm) and low temperature heat (120-130 °C) for 5 minutes
4. Remove imprint mold (razorblade technique)
5. Use Cr mask and etch (O₂ RIE)
6. Remove mask

A.2 Fluidic Delivery Systems

This section specifies the equipment and materials used for building macrofluidic and microfluidic delivery systems.

A.2.1 Macrofluidics

Interferometric windows: Melles Griot IF-1025-UV

Teflon spacer: made in Physics Machine Shop, Stanford

O-rings, syringes, tubing: standard, Stanford biostores and physics store

Paraffin wrap: Parafilm M sealing film

Index matching fluid: standard, Cargile or Newport

Kapton tape: standard, recommend cutting strips to completely seal edge of sample

Optical cage setup: standard 1"-optics-compatible components

Magnetic pipette recommended (Stanford biostores)

Spanner wrench recommended to provide even pressure when sealing chamber

A.2.2 Microfluidics

Chip design following rules of Stanford Microfluidics Foundry

Recommend 100 μm x 100 μm valve area, Stainless Steel 316 Hypodermic Tubing, 23 Gauge for inlets/outlets, and "wiring" in Physics Machine Shop, Stanford for clean finishes of tubes

Scotch tape for cleaning

A.3 Double Photonic Crystal Slab Process Flow

This is a process flow mentioned in Chapter 6 and designed for thick substrates. Both 3 mm and 6 mm substrates were investigated for these steps. Separately, the definition of spacers, backfilling, and assembly were completed on dummy 3 mm - 6 mm thick wafers.

1. **Obtain wafer and polish.** (recommend polishing at Ginzton Crystal Shop). Hayward Quartz fused silica (higher quality "synthetic" type), cut to size if needed, recommended. Initial processing studies used Standard Fused Quartz FSG-N (better quality than GE124, but more bubbles present than synthetic quartz).
2. **Thin edges.** If needed for compatibility with mounts, thin 4" wafer on edges: remove ~10 mm border, leave ~1.5 mm thickness on edge. Alternatively, use 3" diameter "piece" mounted on 4" carrier
3. **Decontaminate.** Follow standard steps per SNF (wbsilicide). If later processing steps will be with clean LPCVD, use N₂ gun or special dryer, then store, before doing wbdiff clean. For semi-clean or contaminated PECVD, use N₂ gun and/or ultrasonic clean (Megasonic) with increased vacuum.
4. **Clean.** wbnonmetal 5:1 Sulfuric Acid: Hydrogen peroxide at $\sim 110 \pm 10^\circ\text{C}$, for 20 minutes. Again, use Megasonic to rinse/dry (with vacuum adjustment), spin-rinse dryer with special holder, or manually dry.
5. **Deposit.** Options for photonic crystal layer are: Clean LPCVD (low stress standard recipe), semi-clean PECVD (requires 7h40min clean + predeposition + calibration before running sample), or contaminated PECVD (predeposition + calibration + sample). PECVD is recommended for ease of handling. Deposit 200nm SiNx (clean chamber first). Alternatively, if both sides of the sample can be

coated or a carrier is used, LPCVD is an option. For LPCVD, pre-diff clean at wbdiff < 1 hour before loading, and use dryer only (no spin) or N₂ gun. Use caution when handling the thicker wafers. A special spatula in addition to large tweezers is recommended for PECVD.

STS PECVD recipe: standard nitride

Parameters:

2% SiH₄ (Silane) - 2000 sccm, 100% NH₃ (Ammonia) - 35 sccm

Uniformity ~ 1%, deposition rates ~70 Å/minute (~30 min deposition)

Steps:

Cleaning cycle, with no wafer inside machine – coat walls with ~250 nm SiNx.

Coat calibration sample - 4 inch Silicon wafer, and measure SiNx layer thickness using Rudolph ellipsometer, Woollam ellipsometer, or nanometrics tool.

Coat actual sample(s) and a witness Si wafer.

LPCVD recipe: nitride2 – stoichiometric nitride

Steps:

Full boat with 20 dummy Si wafers; recommend 5 wafers for samples in the middle. Samples face furnace back side, and center wafer is 61 cm from front flange. User may need pre-etch stress-relieving "streets" to help subsequent sample dicing.

6. **Pattern.** For Optical Samples (for purely mechanical testing skip to Step 11): Interference lithography: Nd:YAG laser, tripled in frequency from 1.06 µm to 355 nm, pulsed energy 50 mJ; 60 Hz. 2D arrays of holes were patterned on samples as large as 4 inch wafers.

Recipe:

Spin. Coat with bi-layer resist (adjust according to sample size): Brewer Science, ARC i-CON-16 conformal BARC to control substrate reflectivity and enhance the critical dimension control first, then on top of the ARC spin Shipley SPR505 or NR700photoresist coated at 4000 rpm. (SPR has shown better uniformity thus far). Bake resist on a hotplate at 90 °C

Expose. Double exposure with 90° rotation, using black paper mounted above the wafer when needed to define different size photonic crystal areas

Develop. Develop samples with tetramethylammonium hydroxide developer (MEGAPOSIT, MF 702) - could be developed at Univ. of New Mexico and also again at Stanford if needed, followed by a DI water rinse

7. **Coat.** Deposit 50 nm of Cr or Ti at Stanford (Innotec, ES26C evaporator at ~0.3 Å/sec deposition rate). The chrome serves as a mask for subsequent pattern transfer of the photonic crystal holes.
8. **Liftoff.** Acetone liftoff process, as described in Chapter 4
9. **Etch.** NF₃ dry etch on tool similar to AMT etcher (semiclean) / PQuest/ p5000/drytek to etch resist and SiNx, stop on quartz (timed). PQuest was tested; 3" wafers on carriers would work well there.
May need to etch in steps to avoid burning resist since quartz wafer is cooled with water vs. Helium (p5000). May need to use a container to fool the system to thinking the wafer is thin (per techniques with Prof. Blas Cabrera Group).
10. **Descum.** O₂ plasma with Drytek4 etcher
11. **Define.** Set up trenches for PDMS spacers

Steps:

Evaporate. Create sacrificial metal layer (W) ~100nm Innotec (shadow mask ~0.5mm features) for PDMS trench definition. Alternatively, use contaminated polysilicon deposition (UC Berkeley)

Spin. Spin on 1 micron resist (3612, or thicker) to protect from 'spray' of wafer saw

Spray. Spray coat from crystal shop directly on metal and hard coverslip

Slice. Leaving the resist (spray coat) on, slice ~1.5 mm deep, 1-2 mm wide trenches with wafersaw (stripes along wafer)

12. **Remove.** Use acetone to remove resist/spray coat (leave metal). Metal should be clean and thin still

13. **Backfill** channels with PDMS

Steps:

Seal ends of trenches with Kapton tape or epoxy

Gasket: Put on a resist-covered quartz wafer as gasket

Inject PDMS into trenches w/ syringe

Cure, then use acetone to remove gasket

14. **Etch** In SNF: Remove metal (W) or polysi selectively from SiNx/quartz with XeF₂ Xactix or wet etchant that will not attack PDMS, SiNx, or quartz

15. **Assemble.** Clean PDMS and clean SiNx surface top wafer/ pieces (with O₂ plasma), then bring two slabs into contact in clean environment

Appendix B: Characterization Setups

B.1 Photonic Crystal Characterization Equipment

These pieces of equipment or parts were mentioned throughout the text for both single and double photonic crystal slab characterization.

Spectrum analyzer: Hewlett Packard, HP70951B

QTH white light source: Model 66181, Oriel

Fiber spectrometer: USB4000, Ocean Optics

Shim: FGSM0.005, Misumi

DC motors: CONEX-TRA25CC, Newport Corporation

Linear stages with aperture: (2 stacked) 426As, Newport Corporation

Motion control interface: NSTRUCT platform, Newport Corporation

Inverted microscope: ECLIPSE TE2000-U, Nikon

Aspheric F/0.85 focusing assembly: Model 77799, Newport Corporation

0.125 inch glass fiber bundle: Model 77527, Newport Corporation

CMOS camera for alignment: DCC1645-C, Thorlabs

B.2 TEC/VCSEL/Detector/Other Characterization Equipment

These pieces of equipment or parts were mentioned throughout the text for characterization of the TEC/VCSEL/detector and other components.

TEC: Custom Thermoelectric, Part 00411-9G30-20CN

Spectrum analyzer: Hewlett Packard, HP70951B

Fiber spectrometer: USB4000, Ocean Optics

Keithley Instruments 6221 AC/DC Laser Driver

ILX Lightwave LDC-3744B Laser Diode Controller

Lock-in Amplifier: Stanford Research Systems SRS830

Keithley 7001 Switch Mainframe with two Keithley 7158 mechanical relay switch cards

Insulated precision thermocouple: 40 gauge (0.076 mm diameter) Omega Engineering,
5SRTC-TT-T-40-36

Digital recording thermometer: Omega Engineering, HH-506-RA

Multimeter: 34401A, Hewlett-Packard

Bibliography

1. Benedictow, O.J., *The Black Death, 1346-1353 : the complete history*2004, Woodbridge, Suffolk, UK; Rochester, N.Y., USA: Boydell Press.
2. Jenner, E., *Inquiry into the Causes and Effects of the Variolae Vaccine*1798, London: Sampson Low
3. CDC, *A CDC Framework for Preventing Infectious Diseases*, U.S.D.o.H.a.H. Services, Editor 2011.
4. Organization, W.H., *The world health report 2007 - A safer future: global public health security in the 21st century*, 2007: Geneva.
5. Shu X., R.A., Lin M. Z., Aguilera T. A., Lev-Ram V., Steinbach P. A., and Tsien R. Y., *Mammalian expression of infrared fluorescent proteins engineered from a bacterial phytochrome*. Science, 2009. **324**(5928): p. 804.
6. Filonov, G.S., Piatkevich, K.D., Ting, L.M., Zhang, J., Kim, K. and V.V. Verkhusha, *Bright and stable near-infrared fluorescent protein for in vivo imaging*. Nat Biotechnol, 2011. **29**(8): p. 757-61.
7. Berger, C., Gremlich, H. U., Schmidt, P., Cannet, C., Kneuer, R., Hiestand, P., Rausch, M., and M. Rudin, *In vivo monitoring the fate of Cy5.5-Tat labeled T lymphocytes by quantitative near-infrared fluorescence imaging during acute brain inflammation in a rat model of experimental autoimmune encephalomyelitis*. J Immunol Methods, 2007. **323**(1): p. 65-77.
8. Veiseh, M., et al., *Tumor Paint: A Chlorotoxin:Cy5.5 Bioconjugate for Intraoperative Visualization of Cancer Foci*. Cancer Res., 2007. **67**(14): p. 6882-6888.
9. Gee M. S., U.R., Bergquist H., Alencar H., Reynolds F., Maricevich M., Weissleder R., Josephson L., and Mahmood U., *Human breast cancer tumor models: molecular imaging of drug susceptibility and dosing during HER2/neu-targeted therapy*. Radiology, 2008. **248**(3): p. 925.
10. Page, W.H., *Man And His Machines: Resuscitation Cage For Mine Canaries*, in *The World's Work: A History of Our Time*1914.
11. Hunt, H.K. and A.M. Armani, *Label-free biological and chemical sensors*. Nanoscale, 2010. **2**(9): p. 1544-59.
12. Lupta, P.B., L.J. Sokoll, and D.W. Chan, *Immunosensors—principles and applications to clinical chemistry*. Clinica Chimica Acta, 2001. **314**(1-2): p. 1-26.
13. Alexander, C., et al., *Molecular imprinting science and technology: a survey of the literature for the years up to and including 2003*. Journal of Molecular Recognition, 2006. **19**(2): p. 106-180.

14. Ye, L. and K. Mosbach, *Molecular Imprinting: Synthetic Materials As Substitutes for Biological Antibodies and Receptors†*. Chemistry of Materials, 2008. **20**(3): p. 859-868.
15. Grünberg, P., et al., *Layered Magnetic Structures: Evidence for Antiferromagnetic Coupling of Fe Layers across Cr Interlayers*. Physical Review Letters, 1986. **57**(19): p. 2442-2445.
16. Baibich, M.N., et al., *Giant Magnetoresistance of (001)Fe/(001)Cr Magnetic Superlattices*. Physical Review Letters, 1988. **61**(21): p. 2472-2475.
17. Osterfeld, S.J., et al., *Multiplex protein assays based on real-time magnetic nanotag sensing*. Proc Natl Acad Sci U S A, 2008. **105**(52): p. 20637-40.
18. Summerlot, D., et al., *Nanoporous Gold Electrode for Electrochemical Sensors in Biological Environment*. Procedia Engineering, 2011. **25**(0): p. 1457-1460.
19. O'Sullivan, C.K. and G.G. Guilbault, *Commercial quartz crystal microbalances – theory and applications*. Biosensors and Bioelectronics, 1999. **14**(8-9): p. 663-670.
20. Lakowicz, J.R. and B.R. Masters, *Principles of Fluorescence Spectroscopy, Third Edition*. Journal of Biomedical Optics, 2008. **13**(2): p. 029901-2.
21. Thrush, E., et al., *Monolithically integrated semiconductor fluorescence sensor for microfluidic applications*. Sensors and Actuators, B: Chemical, 2005. **105**(2): p. 393.
22. Dandin, M., P. Abshire, and E. Smela, *Optical filtering technologies for integrated fluorescence sensors*. Lab. Chip, 2007. **7**(8): p. 955-977.
23. Helmchen, F., et al., *A Miniature Head-Mounted Two-Photon Microscope: High-Resolution Brain Imaging in Freely Moving Animals*. Neuron, 2001. **31**(6): p. 903-912.
24. Thomas, J., et al., *Long wavelength fluorescence based biosensors for in vivo continuous monitoring of metabolites*, 2006, Proc. SPIE: San Jose, CA, USA. p. 60781Y-9.
25. Flusberg, B.A., et al., *High-speed, miniaturized fluorescence microscopy in freely moving mice*. Nat. Meth., 2008. **5**(11): p. 935-938.
26. Mateus, C.F.R., et al., *Ultra-sensitive immunoassay using VCSEL detection system*. Electronics Letters, 2004. **40**(11): p. 649-651.
27. Mateus, C.F.R., et al., *Compact label-free biosensor using VCSEL-based measurement system*. Photonics Technology Letters, IEEE, 2004. **16**(7): p. 1712-1714.
28. Huang, M.C.Y., et al., *VCSEL Optoelectronic Biosensor for Detection of Infectious Diseases*. Photonics Technology Letters, IEEE, 2008. **20**(6): p. 443-445.
29. Ko, H.-S., et al., *A Compact Tunable VCSEL and a Built-in Wavelength Meter for a Portable Optical Resonant Reflection Biosensor Reader*. J. Opt. Soc. Korea. **14**(4): p. 395-402.

30. Hasnain, G., Tai, K., Wang, Y. H., Wynn, J. D., Choquette, K. D., Weir, B. E., Dutta, N. K. and A.Y. Cho, *Monolithic integration of photodetector with vertical cavity surface emitting laser*. Electronics Letters, 1991. **27**(18): p. 1630-1632.
31. Thrush, E., et al., *Integrated semiconductor fluorescent detection system for biochip and biomedical applications*, in *Proc. SPIE2002*, Proc. SPIE. p. 289-297.
32. Thrush, E., et al., *Integrated bio-fluorescence sensor*. Journal of Chromatography A, 2003. **1013**(1-2): p. 103.
33. Thrush, E., *Integrated Fluorescence Sensor*, 2004, Ph.D. Thesis, Stanford University: Stanford, CA.
34. Thrush, E., et al., *Integrated semiconductor vertical-cavity surface-emitting lasers and PIN photodetectors for biomedical fluorescence sensing*. IEEE Journal of Quantum Electronics, 2004. **40**(5): p. 491.
35. Thrush E., L.O., Cook L. J., Deich J., Kurtz A., Smith S. J, Moerner W. E., and Harris J. S., *Monolithically integrated semiconductor fluorescence sensor for microfluidic applications*. Sensors Actuators, 2005. **105**(2): p. 393.
36. O'Sullivan T.D., M., E.A., Parashurama N., Conca C., Gambhir S.S., Harris J.S., and Levi O., *Implantable semiconductor biosensor for continuous in vivo sensing of far-red fluorescent molecules*. Opt. Express. **18**(12): p. 12513.
37. O'Sullivan, T.D., *Implantable Fluorescence Sensor for Continuous Molecular Monitoring in Live Animals*, 2010, Ph.D. Thesis, Stanford University: Stanford, CA.
38. J. S. Harris, T.D.O.S., T. Sarmiento, M. M. Lee and S. Vo, *Emerging applications for vertical cavity surface emitting lasers*. Semiconductor Science and Technology, 2011. **26**(1): p. 014010.
39. Calvert T., C.B., and Lambkin J. D., *80C continuous wave operation of AlGaInP based visible VCSEL*. Electron. Lett., 2002. **38**(5): p. 222.
40. Johnson, K. and M. Hibbs-Brenner. *High output power 670nm VCSELs*. in *Proc. SPIE*. 2007. San Jose, CA, USA: SPIE.
41. A. Knigge, M.Z., H. Wenzel, M. Weyers, and G. Trankle, *High efficiency AlGaInP-based 650 nm vertical-cavity surface-emitting lasers*. Electronics Letters, 2001. **37**(20): p. 1222.
42. O'Sullivan, T., et al., *Implantable semiconductor biosensor for continuous in vivo sensing of far-red fluorescent molecules*. Optics Express, 2010. **18**(12).
43. Zhu, H., et al., *Analysis of biomolecule detection with optofluidic ring resonator sensors*. Opt. Express, 2007. **15**(15): p. 9139-9146.
44. Nitkowski, A., A. Baeumner, and M. Lipson, *On-chip spectrophotometry for bioanalysis using microring resonators*. Biomed. Opt. Express. **2**(2): p. 271-277.

45. Levene, M.J., et al., *Zero-Mode Waveguides for Single-Molecule Analysis at High Concentrations*. Science, 2003. **299**(5607): p. 682.
46. Almeida, V.R., et al., *Guiding and confining light in void nanostructure*. Opt. Lett., 2004. **29**(11): p. 1209-1211.
47. Kim, D.W., et al., *Simultaneous measurement of refractive index and temperature based on a reflection-mode long-period grating and an intrinsic Fabry-Perot interferometer sensor*. Opt. Lett., 2005. **30**(22): p. 3000-3002.
48. Wei, T., et al., *Temperature-insensitive miniaturized fiber inline Fabry-Perot interferometer for highly sensitive refractive index measurement*. Opt. Express, 2008. **16**(8): p. 5764-5769.
49. Ouyang, H., C.C. Striemer, and P.M. Fauchet, *Quantitative analysis of the sensitivity of porous silicon optical biosensors*. Applied Physics Letters, 2006. **88**(16): p. 163108.
50. Rong, G., et al., *Nanoscale porous silicon waveguide for label-free DNA sensing*. Biosensors and Bioelectronics, 2008. **23**(10): p. 1572-1576.
51. Armani, A.M. and K.J. Vahala, *Heavy water detection using ultra-high-Q microcavities*. Optics Letters, 2006. **31**(12): p. 1896-1898.
52. Armani, A.M., et al., *Label-Free, Single-Molecule Detection with Optical Microcavities*. Science, 2007. **317**(5839): p. 783-787.
53. Liang, W., et al., *Highly sensitive fiber Bragg grating refractive index sensors*. APPLIED PHYSICS LETTERS, 2005. **86**(15): p. 151122-3.
54. Lee, M.R. and P.M. Fauchet, *Two-dimensional silicon photonic crystal based biosensing platform for protein detection*. Opt. Express, 2007. **15**(8): p. 4530-4535.
55. Lee, M.R. and P.M. Fauchet, *Nanoscale microcavity sensor for single particle detection*. Optics Letters, 2007. **32**(22): p. 3284-3286.
56. Kang, C. and S.M. Weiss, *Photonic crystal with multiple-hole defect for sensor applications*. Opt. Express, 2008. **16**(22): p. 18188-18193.
57. Jung, I., et al., *Highly Sensitive Monolithic Silicon Photonic Crystal Fiber Tip Sensor for Simultaneous Measurement of Refractive Index and Temperature*. J. Lightwave Technol., 2011. **29**(9): p. 1367-1374.
58. Fan, X. and I.M. White, *Optofluidic microsystems for chemical and biological analysis*. Nat Photon, 2011. **5**(10): p. 591-597.
59. Fahrenfort, J., *Attenuated total reflection: A new principle for the production of useful infra-red reflection spectra of organic compounds*. Spectrochimica Acta, 1961. **17**(7): p. 698-709.
60. Harrick, N.J., *Internal Reflection Spectroscopy* 1967, New York: John Wiley and Sons.

61. Vo Dinh, T., Cullum, B., *Biosensors and biochips: advances in biological and medical diagnostics*. Journal of Analytical Chemistry, 2000. **366**(6): p. 540-551.
62. Altug, H. and J. Vuckovic, *Polarization control and sensing with two-dimensional coupled photonic crystal microcavity arrays*. Optics Letters, 2005. **30**(9): p. 982-4.
63. White, I.M., H. Oveys, and X.D. Fan, *Liquid-core optical ring-resonator sensors*. Optics Letters, 2006. **31**(9): p. 1319-21.
64. Yin, X. and L. Hesselink, *Goos-Hanchen shift surface plasmon resonance sensor*. APPLIED PHYSICS LETTERS, 2006. **89**(26): p. 261108-261108-3.
65. Lee, M. and P.M. Fauchet, *Two-dimensional silicon photonic crystal based biosensing platform for protein detection*. Optics Express, 2007. **15**(8): p. 4530-4535.
66. Levi, O., Lee, M.M., Zhang, J., Lousse, V., Brueck, S.R.J., Fan, S. and J.S. Harris. *Optical Characterization and Sensitivity Evaluation of Guided-Resonances in Photonic Crystal Slabs for Biosensing Applications*. in *Conference on Lasers and Electro-Optics/Quantum Electronics and Laser Science Conference and Photonic Applications Systems Technologies*. 2007. Optical Society of America.
67. Vollmer, F. and S. Arnold, *Whispering-gallery-mode biosensing: label-free detection down to single molecules*. Nature Methods, 2008. **5**(7): p. 591-596.
68. Fan, X., White, I.M., Shopova, S. I., Zhu, H., Suter, J.D., Sun Y., *Sensitive optical biosensors for unlabeled targets: A review*. Analytica Chimica Acta, 2008. **620**(1-2): p. 8.
69. Nazirizadeh, Y., et al., *Low-cost label-free biosensors using photonic crystals embedded between crossed polarizers*. Opt. Express. **18**(18): p. 19120-19128.
70. White, I.M. and X.D. Fan, *On the performance quantification of resonant refractive index sensors*. Optics Express, 2008. **16**(2): p. 1020-1028.
71. Homola, J., *Present and future of surface plasmon resonance biosensors*. Analytical and Bioanalytical Chemistry, 2003. **377**(3): p. 528-539.
72. Tuchin, V.V., *Handbook of Optical Biomedical Diagnostics* 2002: SPIE Press.
73. Tetz, K.A., L. Pang, and Y. Fainman, *High-resolution surface plasmon resonance sensor based on linewidth-optimized nanohole array transmittance*. Optics Letters, 2006. **31**(10): p. 1528-30.
74. Pang, L., et al., *Spectral sensitivity of two-dimensional nanohole array surface plasmon polariton resonance sensor*. Applied Physics Letters, 2007. **91**(12): p. 123112.
75. Yu, Z. and S. Fan, *Extraordinarily high spectral sensitivity in refractive index sensors using multiple optical modes*. Opt. Express, 2011. **19**(11): p. 10029-10040.
76. Chang-Hasnain, C.J., *Progress and prospects of long-wavelength VCSELs*. Communications Magazine, IEEE, 2003. **41**(2): p. S30-S34.

77. Ortsiefer, M., et al., *2.5-mW single-mode operation of 1.55-μm buried tunnel junction VCSELs*. Photonics Technology Letters, IEEE, 2005. **17**(8): p. 1596-1598.
78. Hofmann, W. and M.C. Amann, *Long-wavelength vertical-cavity surface-emitting lasers for high-speed applications and gas sensing*. Optoelectronics, IET, 2008. **2**(3): p. 134-142.
79. Wilmsen, C.W., H. Temkin, and L.A. Coldren, *Vertical-cavity surface-emitting lasers: design, fabrication, characterization, and applications*2001, Cambridge: Cambridge Univ Press.
80. Lee, T.T., et al., *Low-frequency noise characterization of near-IR VCSELs for functional brain imaging*, in *Photonic Therapeutics and Diagnostics IV*2008: San Jose, CA, USA. p. 68422T-8.
81. Cocorullo, G. and I. Rendina, *Thermo-optical modulation at 1.5 mu m in silicon etalon*. Electronics Letters, 1992. **28**(1): p. 83-85.
82. Han, M. and A. Wang, *Temperature compensation of optical microresonators using a surface layer with negative thermo-optic coefficient*. Opt. Lett., 2007. **32**(13): p. 1800-1802.
83. Teng, J., et al., *Athermal Silicon-on-insulator ring resonators by overlaying a polymer cladding on narrowed waveguides*. Opt. Express, 2009. **17**(17): p. 14627-14633.
84. Guha, B., B.B.C. Kyotoku, and M. Lipson, *CMOS-compatible athermal silicon microring resonators*. Opt. Express. **18**(4): p. 3487-3493.
85. Yablonovitch, E., *Inhibited Spontaneous Emission in Solid-State Physics and Electronics*. Physical Review Letters, 1987. **58**(20): p. 2059-2062.
86. John, S., *Strong localization of photons in certain disordered dielectric superlattices*. Physical Review Letters, 1987. **58**(23): p. 2486-2489.
87. Joannopoulos, J.D., P.R. Villeneuve, and S. Fan, *Photonic crystals*. Solid State Communications, 1997. **102**(2-3): p. 165-173.
88. Suh, W., *Photonic Crystal Slabs: Theory and Applications*, in *Electrical Engineering*2005, Stanford University: Stanford, CA.
89. Joannopoulos, J.D., Robert D Meade, and Joshua N Winn *Photonic Crystals : Molding the Flow of Light*1995, Princeton, N.J.: Princeton University Press.
90. Suh, W., *Photonic crystal slabs: Theory and applications*, 2006, Ph.D. Thesis, Stanford University: Stanford, CA.
91. Pendry, J.B. and A. MacKinnon, *Calculation of photon dispersion relations*. Physical Review Letters, 1992. **69**(19): p. 2772-2775.
92. Pendry, J.B., *Photonic Band Structures*. Journal of Modern Optics, 1994. **41**(2): p. 209-229.
93. Liu, V. and S. Fan *S4 : A free electromagnetic solver for layered periodic structures*. Computer Physics Communications. DOI: 10.1016/j.cpc.2012.04.026.

94. El Beheiry, M., et al., *Sensitivity enhancement in photonic crystal slab biosensors*. Opt. Express, 2010. **18**(22): p. 22702-22714.
95. Choquette, K.D. and R.E. Leibenguth, *Control of vertical-cavity laser polarization with anisotropic transverse cavity geometries*. Photonics Technology Letters, IEEE, 1994. **6**(1): p. 40-42.
96. Debernardi, P., et al., *Reliable polarization control of VCSELs through monolithically integrated surface gratings: a comparative theoretical and experimental study*. Selected Topics in Quantum Electronics, IEEE Journal of, 2005. **11**(1): p. 107-116.
97. Burger, M., Osher, S.J., Yablonovitch, E., *Inverse Problem Techniques for the Design of Photonic Crystals*. Industrial Mathematics, 2004. **E87-C**(3): p. 258-265.
98. Lu, J. and J. Vuckovic, *Inverse design of nanophotonic structures using complementary convex optimization*. Opt Express, 2010. **18**(4): p. 3793-804.
99. Thrush, E., et al., *Integrated bio-fluorescence sensor*. Journal of Chromatography A, 2003. **1013**(1-2): p. 103-110.
100. Larson, M.C., B. Pezeshki, and J.S. Harris, Jr., *Vertical coupled-cavity microinterferometer on GaAs with deformable-membrane top mirror*. Photonics Technology Letters, IEEE, 1995. **7**(4): p. 382-384.
101. Larson, M.C., A.R. Massengale, and J.S. Harris, *Continuously tunable micromachined vertical cavity surface emitting laser with 18 nm wavelength range*. Electronics Letters, 1996. **32**(4): p. 330-332.
102. Sugihwo, F., M.C. Larson, and J.S. Harris, Jr., *Micromachined widely tunable vertical cavity laser diodes*. Microelectromechanical Systems, Journal of, 1998. **7**(1): p. 48-55.
103. Chang-Hasnain, C.J., *Tunable VCSEL*. Selected Topics in Quantum Electronics, IEEE Journal of, 2000. **6**(6): p. 978-987.
104. Riemschneider, F., et al., *Continuously tunable long-wavelength MEMS-VCSEL with over 40-nm tuning range*. Photonics Technology Letters, IEEE, 2004. **16**(10): p. 2212-2214.
105. Cole, G.D., et al., *Short-wavelength MEMS-tunable VCSELs*. Opt. Express, 2008. **16**(20): p. 16093-16103.
106. O'Sullivan, T.D., et al., *Compact Semiconductor Bioluminescence Bio-sensors*, in *Frontiers in Optics / Laser Science 2007*, Optical Society of America. p. JMD5.
107. Heitz, R.T., et al. *A low noise current readout architecture for fluorescence detection in living subjects*. in *Solid-State Circuits Conference Digest of Technical Papers (ISSCC), 2011 IEEE International*.

108. Wu, J., Xiao, W. and Y.M. Lu, *Temperature and wavelength dependence of gain and threshold current detuning with cavity resonance in vertical-cavity surface-emitting lasers*. Optoelectronics, IET, 2007. **1**(5): p. 206-210.
109. Wipiejewski, T., et al. *Performance and reliability of oxide confined VCSELs*. in *Electronic Components and Technology Conference*. 1999.
110. Ian Aeby, D.C., Brian Gibson, Christopher J. Helms, Hong Q. Hou, and D.J.B. Wenlin Luo, Charlie X. Wang. *Highly reliable oxide VCSELs for datacom applications*. in *Proceedings of SPIE*. 2003

111. Klein Johnson, M.H.-B., William Hogan, and Matthew Dummer, *Advances in Red VCSEL Technology*. Advances in Optical Technologies, 2012. **2012**.
112. Brueck, S.R.J., *Optical and Interferometric Lithography - Nanotechnology Enablers*. Proceedings of the IEEE, 2005. **93**(10): p. 1704-1721.
113. Raub, A.K. and S.R.J. Brueck, *Large area 3D helical photonic crystals*. Journal of Vacuum Science & Technology B: Microelectronics and Nanometer Structures, 2011. **29**(6): p. 06FF02-6.
114. Chou, S.Y., P.R. Krauss, and P.J. Renstrom, *Nanoimprint lithography*. Journal of Vacuum Science & Technology B: Microelectronics and Nanometer Structures, 1996. **14**(6): p. 4129-4133.
115. Jiang, X., et al., *Immunosensors for detection of pesticide residues*. Biosensors and Bioelectronics, 2008. **23**(11): p. 1577-1587.
116. Knopp, D., D. Tang, and R. Niessner, *Review: bioanalytical applications of biomolecule-functionalized nanometer-sized doped silica particles*. Anal Chim Acta, 2009. **647**(1): p. 14-30.
117. Kalia, J. and R.T. Raines, *Advances in Bioconjugation*. Curr Org Chem, 2010. **14**(2): p. 138-147.
118. Chung-Yen, C., W. Fung, and L.J. Guo, *Polymer microring resonators for biochemical sensing applications*. Selected Topics in Quantum Electronics, IEEE Journal of, 2006. **12**(1): p. 134-142.
119. Yalcin, A., et al., *Optical sensing of biomolecules using microring resonators*. Selected Topics in Quantum Electronics, IEEE Journal of, 2006. **12**(1): p. 148-155.
120. Li, H. and X. Fan, *Characterization of sensing capability of optofluidic ring resonator biosensors*. APPLIED PHYSICS LETTERS, 2010. **97**(1): p. 011105-3.
121. Wang, Z. and D.J. Bornhop, *Dual-Capillary Backscatter Interferometry for High-Sensitivity Nanoliter-Volume Refractive Index Detection with Density Gradient Compensation*. Analytical Chemistry, 2005. **77**(24): p. 7872-7877.
122. Chiang, H.P., et al., *Surface plasmon resonance monitoring of temperature via phase measurement*. Optics Communications, 2004. **241**(4-6): p. 409-418.

123. Grassi, J.H. and R.M. Georgiadis, *Temperature-Dependent Refractive Index Determination from Critical Angle Measurements: Implications for Quantitative SPR Sensing*. Analytical Chemistry, 1999. **71**(19): p. 4392-4396.
124. Gylfason, K.B., et al., *On-chip temperature compensation in an integrated slot-waveguide ringresonator refractive index sensor array*. Opt. Express, 2010. **18**(4): p. 3226-3237.
125. Dahlin, A.B., J.O. Tegenfeldt, and F. Höök, *Improving the Instrumental Resolution of Sensors Based on Localized Surface Plasmon Resonance*. Analytical Chemistry, 2006. **78**(13): p. 4416-4423.
126. Shankaran, D.R., K.V. Gobi, and N. Miura, *Recent advancements in surface plasmon resonance immunosensors for detection of small molecules of biomedical, food and environmental interest*. Sensors and Actuators, B: Chemical, 2007. **121**: p. 158-177.
127. Duffy, D.C., et al., *Rapid Prototyping of Microfluidic Systems in Poly(dimethylsiloxane)*. Analytical Chemistry, 1998. **70**(23): p. 4974-4984.
128. Thorsen, T., S.J. Maerkl, and S.R. Quake, *Microfluidic Large-Scale Integration*. Science, 2002. **298**(5593): p. 580-584.
129. Psaltis, D., S.R. Quake, and C. Yang, *Developing optofluidic technology through the fusion of microfluidics and optics*. Nature, 2006. **442**(7101): p. 381-386.
130. Whitesides, G.M., *The origins and the future of microfluidics*. Nature, 2006. **442**(7101): p. 368-373.
131. Suh, W., O. Solgaard, and S. Fan, *Displacement sensing using evanescent tunneling between guided resonances in photonic crystal slabs*. Journal of Applied Physics, 2005. **98**(3): p. 1-4.
132. Shi, L., et al., *Tunable structures comprising two photonic crystal slabs: optical study in view of multi-analyte enhanced detection*. Opt. Express, 2009. **17**(13): p. 10623-10632.
133. Rodriguez, A.W., et al., *Bonding, antibonding and tunable optical forces in asymmetric membranes*. Opt. Express, 2011. **19**(3): p. 2225-2241.
134. Povinelli, M.L., et al., *Evanescence-wave bonding between optical waveguides*. Opt. Lett., 2005. **30**(22): p. 3042-3044.
135. Kanamori, Y., T. Kitani, and K. Hane, *Control of guided resonance in a photonic crystal slab using microelectromechanical actuators*. APPLIED PHYSICS LETTERS, 2007. **90**(3): p. 031911-3.
136. Boutami, S., et al., *Ultimate vertical Fabry-Perot cavity based on single-layer photonic crystal mirrors*. Opt. Express, 2007. **15**(19): p. 12443-12449.

137. Guo, Y., et al., *Label-free biosensing using a photonic crystal structure in a total-internal-reflection geometry*. Proc SPIE, 2009. **7188**: p. 71880B-71880B12.
138. Levental, K.R., et al., *Matrix Crosslinking Forces Tumor Progression by Enhancing Integrin Signaling*. Cell, 2009. **139**(5): p. 891-906.
139. Drost, R., et al. *Electronic alignment for proximity communication*. in *Solid-State Circuits Conference, 2004. Digest of Technical Papers. ISSCC. 2004 IEEE International*. 2004.
140. Chow, A., et al. *Measuring 6D Chip Alignment in Multi-Chip Packages*. in *Sensors, 2007 IEEE*. 2007.
141. Basu Mallick, S., et al. *Double-Layered Monolithic Silicon Photonic Crystals*. in *Conference on Lasers and Electro-Optics (CLEO) 2008*. San Jose, CA: Optical Society of America.
142. T. Stomeo, M.G., G. Rainò, A. Passaseo, A. D'Orazio, R. Cingolani, A. Locatelli, D. Modotto, C. De Angelis, and M. De Vittorio, *Optical filter based on two coupled PhC GaAs-membranes*. Optics Letters, 2010. **35**(3).
143. Moon, E.E., et al., *Interferometric-spatial-phase imaging for six-axis mask control*. Journal of Vacuum Science & Technology B: Microelectronics and Nanometer Structures, 2003. **21**(6): p. 3112-3115.
144. Vogenberg, F.R., C. Isaacson Barash, and M. Pursel, *Personalized medicine: part 1: evolution and development into theranostics*. P T, 2010. **35**(10): p. 560-76.
145. Kelkar, S.S. and T.M. Reineke, *Theranostics: Combining Imaging and Therapy*. Bioconjugate Chemistry, 2011. **22**(10): p. 1879-1903.
146. Kircher, M.F., et al., *A brain tumor molecular imaging strategy using a new triple-modality MRI-photoacoustic-Raman nanoparticle*. Nat Med, 2012. **18**(5): p. 829-834.